High-power infrared plasmonic nano-devices

Evgeny G. Mironov

A thesis in fulfillment of the requirements for the degree of

Doctor of Philosophy

School of Engineering and Information Technology

University of New South Wales – Canberra

April 2015

PLEASE TYPE

THE UNIVERSITY OF NEW SOUTH WALES
Thesis/Dissertation Sheet

Surname or Family name: Mironov

First name: Evgeny

Other name/s:

Abbreviation for degree as given in the University calendar: PhD

School: School of Engineering and Information Technology

Faculty:

Title: High-power infrared plasmonic nano-devices

ABSTRACT

Many modern optical nano-devices rely on the excitation of surface plasmon polaritons or localized surface plasmons at the metal-dielectric interfaces. The arising plasmonic effects can then be used for sub-wavelength confinement of optical radiation, production of negative refractive index material, and strong field enhancement of particular components of the incident electric field. Due to the lossy nature of metal, some portion of the electromagnetic energy inevitably converts into heat, which, in case of plasmonic resonances, can thermally damage fragile nano-structures. This thesis experimentally and theoretically investigates the optical properties and heat resistance of infrared nano-antennas, metamaterial slot waveguides and fishnet metamaterials by numerically analyzing or exposing them to incident laser light. More precisely, these studies include:

1) Comparing the performance of titanium and gold dipole nano-antennas. It is shown that titanium-based structures can handle more than 18 dB greater power densities, thereby, being able to withstand 7 times higher electric fields than gold counterparts of similar size.

2) Numerically investigating metamaterial-based silica-filled slot waveguides, whose geometry and judicious choice of constituent materials enable both improvement of their optical properties and operation in high-power regimes. It is found that the proposed design also provides a balanced solution between strong electric field confinement and reasonably low propagation losses.

3) Analysing light-medium interactions in fishnet metamaterial, which has an additional absorbing titanium layer. The experiments demonstrate that the amount of incident optical radiation required to damage these metamaterials reduces by nearly 50% and the exposure leads to various thermal deformations of illuminated surfaces even at moderate laser powers.

Thereby, it is shown that all considered devices are suitable for high-power operation by either having high melting thresholds (nano-antenna and slot waveguide) to withstand strong incident electromagnetic fields or, on contrary, being very temperature dependent and, thus, having a potential to be used as thermal sensors (fishnet metamaterial).

Миронов — Signature

Liming Liu — Witness

27/04/2015 — Date

COPYRIGHT STATEMENT

AUTHENTICITY STATEMENT

ORIGINALITY STATEMENT

'I hereby declare that this submission is my own work and to the best of my knowledge it contains no materials previously published or written by another person, or substantial proportions of material which have been accepted for the award of any other degree or diploma at UNSW or any other educational institution, except where due acknowledgement is made in the thesis. Any contribution made to the research by others, with whom I have worked at UNSW or elsewhere, is explicitly acknowledged in the thesis. I also declare that the intellectual content of this thesis is the product of my own work, except to the extent that assistance from others in the project's design and conception or in style, presentation and linguistic expression is acknowledged.'

Signed Миронов

Date 27/04/2015

# Abstract

Many modern optical nano-devices rely on the excitation of surface plasmon polaritons or localized surface plasmons at the metal-dielectric interfaces. The arising plasmonic effects can then be used for sub-wavelength confinement of optical radiation, production of negative refractive index material, and strong field enhancement of particular components of the incident electric field. Due to the lossy nature of metal, some portion of the electromagnetic energy inevitably converts into heat, which, in case of plasmonic resonances, can thermally damage fragile nano-structures. This thesis experimentally and theoretically investigates the optical properties and heat resistance of infrared nano-antennas, metamaterial slot waveguides and fishnet metamaterials by numerically analyzing or exposing them to incident laser light. More precisely, these studies include:

1) Comparing the performance of titanium and gold dipole nano-antennas. It is shown that titanium-based structures can handle more than 18 dB greater power densities, thereby, being able to withstand 7 times higher electric fields than gold counterparts of similar size.

2) Numerically investigating metamaterial-based silica-filled slot waveguides, whose geometry and judicious choice of constituent materials enable both improvement of their optical properties and operation in high-power regimes. It is found that the proposed design also provides a balanced solution between strong electric field confinement and reasonably low propagation losses.

3) Analysing light-medium interactions in fishnet metamaterial, which has an additional absorbing titanium layer. The experiments demonstrate that the amount of incident optical radiation required to damage these metamaterials reduces by nearly 50% and the exposure leads to various thermal deformations of illuminated surfaces even at moderate laser powers.

Thereby, it is shown that all considered devices are suitable for high-power operation by either having high melting thresholds (nano-antenna and slot waveguide) to withstand strong incident electromagnetic fields or, on contrary, being very temperature dependent and, thus, having a potential to be used as thermal sensors (fishnet metamaterial).

Keywords

Plasmonics, surface plasmon polaritons, localized surface plasmons, infrared, fishnet metamaterials, dipole nano-antennas, slot waveguides.

Acknowledgements

My PhD thesis was not a standalone project, but, in reality, involved tight collaborations, sharing experience in nano-fabrication and having fruitful research discussions on the topics of plasmonic devices and beyond. Thereby, I want to use this opportunity to acknowledge my fellow colleagues and friends for their contributions and continuous support to my work.

First of all, I would like to thank my colleagues from the University of New South Wales – Canberra Liming Liu, Abdul Khaleque, Dr. Ziyuan Li and my supervisor Dr. Haroldo Hattori thanks to whose guidance and help this thesis has been successfully produced. I also acknowledge the general support from the administrative staff of the School of Engineering and Information Technology, especially, Craig Edwards and Michelle McAuliffe, as well as the support provided by Luke Garner and Elvira Berra from the Research Student Unit. Additionally, I want to say a special thanks to Retd. Maj. Heath Pratt for a valuable work experience and Ms. Denise Russel for proofreading my thesis.

During the last 3.5 years I was also a visiting student at the Australian National University (Department of Electronic Materials Engineering, Research School of Physics and Engineering) and I would like to thank its staff Julie Arnold, Timothy Burgess and Prof. Chennupati Jagadish. I also pay my respect to the collaborators Dr. Ilya Shadrivov, A/Prof. Dragomir Neshev and Dr. David Powell (Nonlinear Physics Centre, ANU), Dr. Peter Reece and Wen Jun Toe (School of Physics, UNSW – Sydney) and Prof. Richard De La Rue (School of Engineering, The University of Glasgow) for the fruitful mutual work and valuable research discussions.

The fabrication of nano-devices described in this thesis won't be possible without the support of the staff from Australian National Fabrication Facility (Australian Capital Territory node) and, thus, I am gratitude to Dr. Fouad Karouta, Dr. Kaushal Vora and Dr. Li Li for their help in operating Focused Ion Beam system, Sputter system and Electron Beam Evaporator.

I also thank to my friends Nizami Jafarov, Andrey Kirsanov, Nataliya Derevyanko, Dariya Goranskaya, George Ovchinnikov, Artem Korkh, Andrey Chugunov, Ivan

Rukhlenko, Zhi Zhang and Manuel Cegarra Polo for their continuous support through my research journey.

At last, I thank my parents Yulia Mironova and Gennadiy Mironov, my brother Alexey Mironov, my grandfathers Boris Mozjerin and Alexander Mironov, as well as other relatives for their always being there for me.

Finally, I want to express my sincere gratitude to Ms. Calla Bradford for her selfless support, patience, kindness and understanding, for remaining with me in all circumstances.

List of publications

The present thesis is directly based on the following journal publications and conference proceedings (each chapter has a reference in its introduction section to the corresponding publication):

1) **Evgeny G. Mironov**, Ziyuan Li, Haroldo T. Hattori, Kaushal Vora, Hark Hoe Tan and Chennupati Jagadish, "Titanium nano-antenna for high-power pulsed operation", *IEEE Journal of Lightwave Technology*, vol. 31, issue 15, pp. 2459–2466 (2013)
2) **E G Mironov**, W J Toe, P J Reece and H T Hattori, "Fishnet metamaterials with incorporated titanium absorption layer", *Journal of Physics D: Applied Physics*, vol. 46, no. 49, 495107 (2013)
3) **Evgeny G. Mironov**, Liming Liu, Haroldo Hattori and Richard De La Rue, "Analysis of silica filled-slot waveguides based on hyperbolic metamaterials", *Journal of the Optical Society of America B*, vol. 31, no. 8, pp. 1822–1828 (2014); Erratum – vol. 31, issue 10, pp. 2285 (2014)
4) **Evgeny G. Mironov**, Ziyuan Li and Haroldo T. Hattori, "High power titanium Q-switched nano-antennas", *OSA Advanced Photonics 2013* (Rio Grande, Puerto Rico, United States), ISBN: 978-1-55752-981-7, DOI 10.1364/IPRSN.2013.IM1B.2 (2013)
5) **E G Mironov**, W J Toe, P J Reece and H T Hattori, "Titanium absorption layer in fishnet metamaterials", *Australian and New Zealand Conference on Optics and Photonics 2013 - ANZCOP 2013* (Perth, Western Australia, Australia) (2013)
6) **Evgeny G. Mironov**, Liming Liu, Haroldo Hattori and Richard De La Rue, "Sub-wavelength confinement in metamaterial filled-slot waveguide", *Conference on Lasers and Electro-Optics 2014 / CLEO 2014* (San Jose, California, USA), ISBN: 978-1-55752-999-2 (2014)

The following journal publications and conference proceedings were also published during the candidature:

1) Ziyuan Li, Haroldo T. Hattori and **Evgeny G. Mironov**, “Charnia-like broadband plasmonic nano-antenna”, *Journal of Modern Optics*, vol. 60, issue 10, pp. 790–796 (2013)
2) Liming Liu, Ilya V. Shadrivov, David A. Powell, Md. Rezaur Raihan, Haroldo T. Hattori, Manuel Decker, **Evgeny Mironov** and Dragomir Neshev, “Temperature control of terahertz metamaterials with liquid crystals” (invited paper), *IEEE Transactions on Terahertz Science and Technology*, vol. 3 no. 6, pp. 827–831 (2013), DOI 10.1109/TTHZ.2013.2285570
3) Liming Liu, Ilya V. Shadrivov, David A. Powell, Rezaur Raihan, Haroldo T. Hattori, Manuel Decker, **Evgeny Mironov**, Dragomir N. Neshev, “Liquid crystal tunable terahertz metamaterials”, *Australian and New Zealand Conference on Optics and Photonics 2013 - ANZCOP 2013* (Perth, Western Australia, Australia)
4) Liming Liu, Haroldo T. Hattori, **Evgeny G. Mironov** and Abdul Khaleque, “Composite chromium and graphene oxide as saturable absorber in ytterbium doped Q-switched fiber lasers”, *Applied Optics*, vol. 53, issue 6, pp. 1173–1180 (2014)
5) **Evgeny G. Mironov**, Liming Liu, Abdul Khaleque, Wen Jun Toe, Peter J Reece and Haroldo T. Hattori, “Enhancing the performance of graphene oxide saturable absorbers by adding chromium and titanium to ytterbium doped *Q*-switched laser”. *OptoElectronics and Communication Conference and Australian Conference on Optical Fibre Technology 2014 - OECC / ACOFT 2014*, (Melbourne, Victoria, Australia), 978-1-922107-21-3, Engineers Australia, pp. 498–500 (2014)
6) **Evgeny G. Mironov**, Abdul Khaleque, Liming Liu, Ivan S. Maksymov and Haroldo T. Hattori, “Enhancing Weak Optical Signals by Using a Plasmonic Yagi-Uda Nanoantenna Array”, *IEEE Photonics Technology Letters*, vol. 26, no. 22, pp. 2236–2239 (2014)

Awards and Prizes

1) UNSW Tuition Fee Remission Scholarship (TFR) with a living allowance provided by the University College, UNSW–Canberra (2011-2014)
2) High Impact Journal Publication Prize – $3000, School of Engineering and Information Technology, UNSW–Canberra (2014)
3) Postgraduate Research Support Scheme (PRSS) funding – $2630, Graduate Research School, UNSW–Australia (2014)
4) Completion Scholarship of UNSW, UNSW–Canberra (2014)

Table of contents

List of Abbreviations

CW	Continuous wave
SPP	Surface plasmon polariton
LSP	Localized surface plasmon
TE	Transverse Electric [field]
TM	Transverse Magnetic [field]
CGS	Centimetre-gram-second [units]
MKS	Meter-kilogram-second [units]
SI	International system of units
MDM	Metal-dielectric-metal [structure]
DMD	Dielectric-metal-dielectric [structure]
NIM	Negative index material
SRR	Split ring resonator
ESSR	Electric split ring resonator
FDTD	Finite-difference time-domain [method]
FEM	Finite element method
CFL	Courant–Friedrichs–Lewy [condition]
PML	Perfectly matched layer
CAD	Computer-aided design
GUI	Graphical user interface
FIB	Focused ion beam [system]
EBE	Electron beam evaporator
SEM	Scanning electron microscope [image]
TEM	Transmission electron microscopy
NSOM	Near-field scanning optical microscope
SLM	Spatial light modulator
CCD	Charge-coupled device
Nd:YAG	Neodymium-doped yttrium aluminium garnet ($Nd:Y_3Al_5O_{12}$) [laser]
SERS	Surface enhanced Raman scattering
RLC	R – resistor, L – inductor, C – capacitor
SOI	Silicon on insulator
IPA	Isopropanol (C_3H_8O or C_3H_7OH)
TTM	Two temperature model

List of Figures

List of Tables

Chapter 1 – Introduction

1.1 Preface

Recently, a great deal of attention has been drawn to high-power optical applications, including giant pulse generation using Q-switched and mode-locked lasers **[1-3]**, ablation in metals **[4-7]** and nonlinear effects in light-matter interactions **[8-10]**. Generally, high-power optics involves research on formation of an intense laser beam, the plasmonics that addresses the excitation of electromagnetic resonances in exposed structures, and thermodynamics, which focuses on the heat transfer and temperature distribution in an illuminated material. While being a multidisciplinary topic, the further discussion should start from description of high-power laser sources followed by the outline of interactions between an incident light and medium. This will help to understand the thermal effects arising in plasmonic devices and how the high-power studies discussed in the present work could improve the performances of these structures.

1.2 High-power lasers and thermal-based effects

The construction of high-power laser setups has remained a continuing interest in laser research since their first demonstration in 1960 **[11]**. While the early prototypes were relatively weak and had average powers below milliwatts, following developments allowed increasing the laser output level on several orders **[12]**. Based on their operational regimes, lasers can be classified into two categories: continuous wave (CW) and pulsed lasers (that, in turn, can be either Q-switched or mode-locked). Besides the operating frequency (which is a key parameter for any kind of a laser), the first type is usually characterized by an average output power P_{av} that ranges from several microwatts **[13]** to thousands of watts **[12, 14]**. As for pulsed lasers, the concept of average power doesn't have much practical meaning and their performance is usually assessed by the maximum peak power P_{peak}, duration of a single pulse $\tau_{single\ pulse}$, repetition rate, number of peaks per single pulse, number of excited modes and other important parameters. These characteristics may vary significantly depending on the design of a given Q-switched laser. For example, P_{peak} could be as high as 10 kW **[15]** and $\tau_{single\ pulse}$ could be as short as 56 ps **[16]**. In turn, mode-locked lasers are capable of producing even shorter pulses of 10^{-12}–10^{-14} seconds, with their maximum peak powers exceeding tens of kilowatts **[17]**. In this situation, the term "high power" may seem to be a relative concept, which depends on a particular laser design and intended application. Therefore, for the sake of simplicity, the term "high power" further implies Class 3B and Class 4 lasers according to Australian and New Zealand Laser Safety Standard as outlined in **[18]**.

The interaction between a medium and high-power laser beam often leads to thermal-based effects including extensive heating, melting and ablation of an exposed material. From the laser point of view, the potential damage is generally assessed in terms of fluence, which represents the amount of incident power distributed over a certain area **[19]**. This treatment allows correct descriptions of situations, in which a weak, but narrow beam, deals more damage, than a powerful laser with a large spot diameter. From the material point of view, heating arises from the direct absorption of incoming radiation by electrons with subsequent electron-phonon coupling **[20]**. Further material deformation and heat transfer may be addressed by using a thermodynamics approach that explicitly and rigidly deals with the phase transitions occurring in an exposed medium **[21-23]**. However this is mostly left out of the scope of the present discussion, which, instead, focuses on the impact of plasmonic-based thermal effects.

In plasmonic nano-devices, heating is not limited to that of material absorption, but also involves heating resulting from the excitation of surface plasmon resonances **[24]**. These resonances, which occur at metal-dielectric interfaces under particular conditions **[25]**, are not explicitly taken into account in a thermodynamic treatment, but may play a dominant role because of their localized highly intense fields, which lead to the formation of so-called hot spots **[26]**.

Generally, the interest in plasmonic heating is limited to the case of individual nano-particles that are used for in vivo bio-imaging **[27, 28]** or utilized as therapeutic agents for the thermal treatment of cancer cells **[29, 30]**. Since the near-infrared radiation can be partially transmitted through the human tissues, an incident laser beam is capable of reaching the nano-particles delivered by drugs. Depending on the particle scattering parameters (calculated according to the Mie theory **[31]**), this light is partially scattered, transmitted or absorbed (i.e., the optical energy is converted into heat). High scattering and low absorption is preferable for imaging applications, while strong plasmonic absorption is required for thermal therapy. The exact scattering coefficients are determined by the particle's geometry (single or multilayer) **[32]**, morphology (for example, spheres or cylinders) **[33]**, and the materials used (typically, gold for monolithic particles or combination of gold and quartz for nano-shells).

In most cases, nano-particles are homogeneous (except nano-shells) and have a very simple geometry whereas plasmonic devices, on the contrary, are typically non-uniform and are formed by several individual components of different sizes and shapes. Therefore, nano-particles should be distinguished from plasmonic devices, and only the latter are considered in the following discussion.

1.3 Plasmonic nano-devices

As most optical plasmonic nano-devices are intrinsically passive, to start operating, they require a light source, which can be a local emission generated by a quantum dot **[34, 35]** or quantum well **[36, 37]** micro-laser. However, a large portion of plasmonic structures are simply driven by an external laser setup. As in all cases of medium-laser interaction, the durability of nano-devices become influenced by several parameters, such as the characteristics of the exposed material, increased absorption (which is associated with the excitation of plasmonic resonances) and fluence. The combination of these factors leads to the establishing a melting threshold, above which the performances of structures quickly degrade and they eventually become thermally damaged. Given the small sizes of plasmonic devices, they are quite fragile even for moderate laser radiation levels. Such sensitivity to high temperatures may become disadvantageous and limit the practical application of nano-structures to low-power problems.

An example of a device that could benefit from an increase in its melting threshold and, thereby, substantially expand its operational area, is a nano-antenna. This tiny structure resembles a miniaturized version of a conventional microwave or radio antenna and is usually utilized in photonics to locally enhance electromagnetic radiation. The obtained strong electric fields then can be used for different applications, including sensing **[40]**, imaging **[41]** and nano-particle manipulation **[26, 42]**. Although, to date, the work on thermal effects in optical antennas is very limited, the strong field enhancements in sensors, based on surface enhanced Raman scattering (SERS), may lead to the creation of hot spots, which, in turn, may negatively affect a device's performance and distort its recorded signal.

Nano-antennas can be directly excited by incident radiation or driven by a light coupled from a waveguide **[43]**. While implementing tapers **[44, 45]** or directing light through a focusing array **[46]** dramatically improves coupling efficiency, some portion of electromagnetic energy is always lost due to scattering **[47]**. Also, the waveguide itself can be lossy **[48]** and further limit the amount of radiation that eventually reaches a nano-antenna. Although these losses can be compensated, for example, by adding sections with a gain medium **[49]**, the increased complexity of the final structure limits such an approach in practice. The other solution implies pumping initially more power into the waveguide, but at the potential risk of exceeding the melting threshold and damaging the whole nano-device. High-power (i.e., heat-resistant) waveguides can overcome this limitation and allow more flexibility in choosing the operating regimes of light sources.

Nano-antennas are not the only plasmonic devices driven by external laser sources. Metamaterials, artificial structures with unique optical properties, also rely on the excitation of plasmonic resonances, which originate from coupling between the incident radiation and metal-electron plasma **[25, 50]**. In such situation, the total absorption is not limited only by the material absorption of the metamaterials' media, but is also supplemented with losses associated with the structures' resonant behaviour. This results in a reduction in durability and increased sensitivity to thermal effects, which should be taken into account in any realistic design **[51]**. One of the important practical applications of metamaterials is a metamaterial absorber, which utilizes the plasmonic resonance to attenuate the incident electromagnetic waves **[52, 53]**. Another common example is a thermal emitter in thermophotovoltaic systems **[54, 55]**. In these situations, the importance of plasmonic heating cannot be underestimated.

The above mentioned shortcomings of existing devices have motivated the present work to design plasmonic structures capable of withstanding high powers or, in contrast, effectively exploiting their thermal vulnerabilities, either of which implies addressing the role of plasmonics in producing heat effects on a nano-scale. This is achieved by designing and numerically analyzing a fully operational dipole nano-antenna, fishnet metamaterial and multilayered slot waveguide. The first two nano-devices are fabricated and then experimentally tested by exposing them to varying incident laser radiation. The last structure is studied only theoretically due to fabrication difficulties, however its geometry is also made intrinsically heat resistant. Despite being developed for high-power applications, the designed structures fully retain their plasmonic capabilities and can still be used in low-power regimes.

The study of each plasmonic structure, presented in this thesis begins with a general introduction followed by a literature review of the most recent advances in the corresponding research sub-field. Then, the electromagnetic properties of the relevant nano-device are modelled using a finite-difference time-domain (FDTD) method or similar approach. The theoretical section ends with a brief heat analysis, which includes a qualitative temperature distribution pattern. The next section, at first, describes the measurement setup and experiment methodology, and then provides the information on the exposure conditions. Each chapter ends with a conclusion based on the experimental (or theoretical) results, which outlines the benefits of the proposed design and its potential applications.

1.4 Brief outline of thesis content

While this introduction is limited to a general overview of the material presented in thesis, further information on physics background, fabrication issues, nano-device performances and obtained results are provided only in subsequent chapters. The first four chapters present the theoretical and experimental frameworks that are useful for the following discussion of nano-structures in Chapters 5 to 7. Chapter 8 summarizes the performed studies, while Appendices A and B add some supplementary information regarding sample fabrications. Details of the contents of these chapters are given below.

Chapter 2 provides information of the underlying physical mechanisms responsible for interactions between incident electromagnetic waves and the considered nano-devices. This is achieved by studying the properties and deriving the dispersion relations of surface plasmon polaritons and localized surface plasmons. This chapter also concisely addresses the issues of converting optical energy into thermal energy via the Poynting's theorem.

Chapter 3 introduces the numerical methods implemented in the current work. Firstly, the FDTD method is discussed and the differential equations used in the Yee's algorithm are outlined. Then, the commercial software RSoft FullWAVE is in detail described and some additional information regarding numerical simulations is provided.

Chapter 4 discusses the fabrication equipment utilized to create plasmonic devices, including an Electron Beam Evaporator (EBE), Sputter system and Focused Ion Beam (FIB) system, which are used for either the deposition or processing of nanometre thick films. The chapter concludes with a description of the adopted fabrication methodologies and addresses some patterning issues.

Chapter 5 focuses on titanium and dipole nano-antennas and compares them in terms of field enhancement and high-power handling. The field enhancement factor is evaluated based on numerical simulations with calculations performed for several gap widths. In the experimental section, nano-antennas made of either metal are exposed to nanosecond Q-switched pulses, and the power of incident laser radiation is gradually increased in order to determine the damage threshold, at which the structures start melting. It is shown that, while gold-based nano-antennas have a higher field enhancement factor than their titanium counterparts, their melting threshold is much lower. Therefore, it is possible to obtain higher electric fields in titanium devices by simply increasing the input power of the incident pulses.

Chapter 6 theoretically investigates a silica-filled slot waveguide formed by two metal-dielectric multilayer structures. The behaviour of the fundamental slot mode at infrared frequencies is studied for different gap widths and various ratios of conductor-insulator layer thicknesses. The coupling problem of a slot waveguide is also considered and its transmission as a function of metal-dielectric layer thickness ratios is evaluated. It is found that, at an optimum ratio, the transmission reaches a local maximum, which is surpassed only by a lossless dielectric case. Calculations of the electric field distributions inside a slot waveguide show an improvement in field confinement compared with that of a pure insulator-based slot waveguide. This means that the metamaterial slot waveguide has the potential to achieve a reasonable trade-off between a high field confinement and long propagation distance. The thermal simulations show that the greatest amount of power is localized inside the slot, but, due to the design of the waveguide, even melting of its lateral regions does not considerably affect the device's performance.

Chapter 7 addresses the issues of electromagnetic radiation absorption in fishnet metamaterials by depositing a thin titanium film on top of a multilayer sample, and then studying the absorption of such a structure by varying the thickness of that film. The experiments, in which the samples are exposed to an infrared CW laser, confirm the numerical estimations of significant changes in absorption behaviour. In addition, the formation of a microbump and nanojet are experimentally observed. These results clearly demonstrate the strong impact of an external material placed close to a metamaterial's surface, which leads to a substantial increase in structure's total absorption.

Chapter 8 summarizes the current thesis by presenting the conclusions drawn from this study and providing comments on the potential for future work in the specified research area.

Appendix A provides supplementary information about the computer scripts used to operate the FIB during the patterning of nano-devices by analysing a simple structure's code.

Appendix B presents some examples of advanced patterns made by utilizing the FIB and, thereby, demonstrates the broad capabilities of the fabrication equipment.

Chapter 2 – Theoretical background

2.1 Introduction

Since the research presented in this thesis is focused on infrared plasmonic nano-devices, it is crucial to have a fundamental understanding of the interactions between electromagnetic waves and matter. Therefore, before moving to complex plasmonic designs, a simple case of wave propagation inside a uniform and homogeneous medium is considered.

This chapter begins with a review of the Maxwell's and Helmholtz equations, which form the basis of classical electrodynamics and optics. Then, the fundamental concepts of plasmonics (surface plasmon polaritons (SPPs) and localized surface plasmons (LSPs)) are explained and, finally, the dispersion relations are derived (in a similar manner to the approach presented in **[56]**). The chapter ends with a brief discussion on a conversion of optical radiation into thermal energy by using the Poynting's theorem and estimating the heat distribution in nano-structures.

It should be noted that all physical phenomena described in this and following chapters are always established using classical approximations (i.e., without involving quantum mechanics). Such treatment is valid since, even if the studied structures are as small as tens of nanometres in size, they are still considered too large for quantum effects to dominate.

2.2 Maxwell's equations

2.2.1 Different notations

In the second part of the 19th century, rapid advances in experimental physics allowed qualitative observations of the dependencies between electric and magnetic forces, such as the generation of a magnetic field produced by an electric current (Biot–Savart law) and the generation of an electric current in a conductor exposed to a varying external magnetic field (Faraday's law). The obtained data required researchers to establish a new electromagnetic model capable of explaining all experimental material in a rigid mathematical form. Such model was first demonstrated between 1861 and 1862 by the Scottish physicist James Clerk Maxwell in the form of 4 macroscopic equations, which later became widely known as the *Maxwell's equations*.

In his work, Maxwell summarized everything known in the 19th century about the nature of electromagnetic interactions and proposed a novel way of linking electric and magnetic fields by introducing the displacement current. While some researchers (including Weber and Helmholtz) at first doubted this approach, Maxwell's theory was experimentally proven by Hertz and then expanded by Heaviside and Gibbs, who rewrote the equations in their present form **[57]**. These equations played a crucial role in the later development of the special theory of relativity (which was introduced by Einstein) and, for the last 150 years, have remained the basis of modern electromagnetics.

The Maxwell's equations can be written using various notations depending on the: a) system of units (i.e., Gaussian or International System of Units); b) scale of description (i.e., microscopic or macroscopic); and c) type of equation (i.e., integral or differential). Nevertheless, it should be noted that, despite different notations, all sets of the equations remain equivalent.

In the literature, the Maxwell's equations are typically written in either Gaussian units, also known as symmetric CGS (centimeter-gram-second) or the International System of Units (SI), also known as MKS (meter-kilogram-second). The system of units is usually chosen to simplify the involved measurements and, therefore, depends on a particular problem. In electromagnetics, preference is often given to CGS because the magnetic permeability μ_0 and dielectric permittivity ε_0 of vacuum are dimensionless and both are identical to unity. On the other hand, in MKS, $\mu_0 = 1.25663706 \times 10^{-6}$ N/A^2, $\varepsilon_0 = 8.854187817 \times 10^{-12}$ F/m and the speed of light in vacuum c is connected to μ_0 and ε_0 as:

$$c = \frac{1}{\sqrt{\varepsilon_0 \mu_0}}. \qquad (2.1)$$

Since the research presented in this thesis involves not only electromagnetics but also other fields of physics, SI units are preferred to Gaussian units in all further discussions, unless specified otherwise.

The Maxwell's equations can be also written in either microscopic or macroscopic form. The first approach represents the fields in terms of total charge and current densities (ρ and J), which include the charges and currents on an atomic scale, while, in the second case, bound charges and currents are separated from free counterparts. However, in this work, notations are always based on **[56]** and the total charge and current densities are divided into an external set (which drives the system) and an internal set (which responds to the excitation).

At last, the Maxwell's equations in differential and integral forms can be found in most physics textbooks. The latter form is obtained after applying the Gauss's or Stokes' theorem to the set of original differential equations. While both describe the same physical phenomena, the preference in the current chapter is given to the differential form, because it simplifies the derivation of the SPP waves given in Section 2.3.2.

2.2.2 Maxwell's equations

After taking into account the notations discussed above, the Maxwell's equations can be finally written in a vector form as **[56]**:

$$\nabla \cdot \vec{D} = \rho_{ext} \tag{2.2a}$$

$$\nabla \cdot \vec{B} = 0 \tag{2.2b}$$

$$\nabla \times \vec{E} = -\frac{\partial \vec{B}}{\partial t} \tag{2.2c}$$

$$\nabla \times \vec{H} = \vec{J}_{ext} + \frac{\partial \vec{D}}{\partial t}. \tag{2.2d}$$

Here D is the displacement field; B is the magnetic induction (magnetic flux density); E is the electric field, and H is the magnetic field. ρ_{ext} and J_{ext} represent the total external charge and current densities. Each of these equations rephrases one of the four experimentally observed laws:

1) Eq. 2a states that electric induction originates from electric charges (Gauss's law);
2) Eq. 2b states that no magnetic charges are experimentally observed (Gauss's law of magnetism);
3) Eq. 2c states that, for a closed loop, changes in the magnetic flux result in induction of the electric field (Faraday's law of induction);

4) Eq. 2d states that the displacement current and changes in electromagnetic induction lead to the formation of a magnetic field (Ampère's circuital law modified by Maxwell's addition).

It should be noted that Maxwell assumed that free magnetic charges don't exist (Eq. 2.2b) and, even today, at the beginning of the 21st century, magnetic monopoles still have not been experimentally observed. If, in future, such elementary charges would be finally found, the Maxwell's equations will be modified by adding free magnetic charge and current densities.

The macroscopic fields in Eq. 2.2a-d can be also linked using magnetization M and polarization P as:

$$\vec{D} = \varepsilon_0 \vec{E} + \vec{P} \qquad (2.3a) \qquad \vec{H} = \frac{1}{\mu_0}\vec{B} - \vec{M} , \qquad (2.3b)$$

which, for linear, isotropic and nonmagnetic media, are simplified to:

$$\vec{D} = \varepsilon_0 \varepsilon \vec{E} \qquad (2.4a) \qquad \vec{B} = \mu_0 \mu \vec{H} . \qquad (2.4b)$$

Here ε and μ denote the relative permittivity and permeability with respect to a vacuum.

2.2.3 Boundary conditions and continuity of components

While the Maxwell's equations govern the propagation of electromagnetic waves, it is important to understand what will happen with the field components on the boundary of two adjacent media (for simplicity, media are denoted as *1* and *2*). Changes in the electric field components can be obtained by considering the electric flux across the media interface and applying the Gauss's law (in the integral form), which results in the condition **[57]**:

$$D_{2n} - D_{1n} = \sigma_{ext} \qquad (2.5a) \qquad E_{2t} - E_{1t} = 0 . \qquad (2.5b)$$

This means that the difference between the normal components of the displacement field D_n is proportional to the surface charge density σ_{ext}, and the tangential components of the electric field E_t are equal on both sides of the boundary (here, a normal component implies the component perpendicular to the interface and the tangential component implies the one at a tangent to that boundary). After using a similar approach for a magnetic field, the conditions become:

$$B_{2n} - B_{1n} = 0 \qquad (2.6a) \qquad\qquad H_{2t} - H_{1t} = J_{ext}, \qquad (2.6b)$$

or, in other words, the normal component of magnetic induction remains continuous and the difference in tangential components of the magnetic field is equal to the surface current density J_{ext}. It should be noted that, in the absence of free external charges or currents (for example, in two adjacent dielectrics) all of the above mentioned components (D_n, E_t, B_n, H_t) become continuous.

2.2.4 Wave equation

If no external charges and currents are present, the wave equation can be derived from the Maxwell's equations by taking the time derivative in Eq. 2.2d and then substituting Eq. 2.4a and Eq. 2.4b into it:

$$\mu_0\mu\left(\nabla\times\frac{\partial\vec{B}}{\partial t}\right) = \varepsilon_0\varepsilon\frac{\partial^2\vec{E}}{\partial t^2}. \qquad (2.7)$$

After using Eq. 2.2c, applying the properties of the curl operator, and also assuming a media with a relative permittivity of $\mu = 1$ (which is true for nonmagnetic materials), Eq. 2.7 becomes:

$$-\varepsilon_0\varepsilon\frac{\partial^2\vec{E}}{\partial t^2} = \mu_0\left(\nabla\times\nabla\times\vec{E}\right) = \mu_0\left(\nabla\left(\nabla\cdot\vec{E}\right) - \nabla^2\vec{E}\right). \qquad (2.8)$$

Since external charges are not taken into account, Eq. 2.2a may be rewritten as:

$$0 = \nabla\cdot\vec{D} = \nabla\cdot\varepsilon\varepsilon_0\vec{E} = \varepsilon\varepsilon_0\nabla\cdot\vec{E} + \varepsilon_0\vec{E}\nabla\cdot\varepsilon \qquad (2.9a)$$

$$\nabla\cdot\vec{E} = -\frac{1}{\varepsilon}\vec{E}\nabla\cdot\varepsilon. \qquad (2.9b)$$

Then, Eq. 2.8 changes to:

$$-\varepsilon_0\varepsilon\frac{\partial^2\vec{E}}{\partial t^2} = \mu_0\left(\nabla\left(-\frac{1}{\varepsilon}\vec{E}\nabla\cdot\varepsilon\right) - \nabla^2\vec{E}\right). \qquad (2.10)$$

For small spatial variations in the dielectric permittivity, the first term on the right-hand side becomes zero. After considering the harmonic time dependence $\vec{E}(\vec{r},t) = \vec{E}(\vec{r})e^{-i\omega t}$, the link between c, ε_0 and μ_0 (Eq. 2.1), and denoting the wave vector in vacuum to be $k_0 = \frac{\omega}{c}$, Eq. 2.10 finally becomes:

$$\nabla^2 \vec{E} + k_0^2 \varepsilon \vec{E} = 0 . \tag{2.11}$$

This equation is known as the Helmholtz equation and describes the propagating wave with amplitude E and wavenumber $k_0^2\varepsilon$.

2.3 Surface plasmons

2.3.1 Introduction to plasmonics

Surface plasmon polaritons can be defined as electromagnetic excitations that propagate along the interface between a metal and dielectric and are confined to that boundary. SPPs were first mathematically predicted at the beginning of the 20th century during studies of radio waves on the surface of an ideal conductor **[58]**. Simultaneously, Wood observed a sharp drop in the intensity of a spectra produced by a visible light, which illuminated a metal grating (Wood's anomaly) **[59]**. However, it was not until the 1960s that Ritchie *et al.* linked this drop to their own work on metallic surfaces **[60]**. Finally, after Sommerfeld's surface waves were experimentally demonstrated using a prism coupler **[61]**, researchers were able to provide a rigid description of SPP waves.

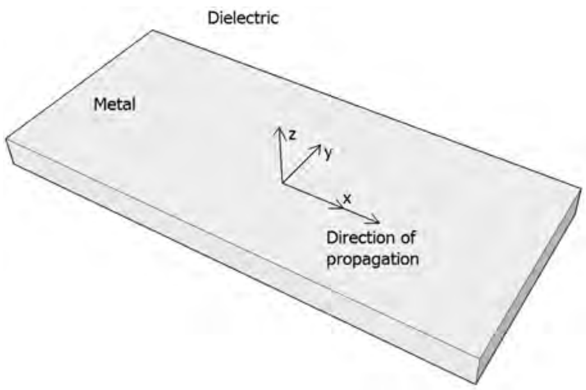

Fig. 2.1 – One-dimensional SPP propagation on metal-dielectric interface

2.3.2 Defining transverse electric and transverse magnetic modes

The derivation of a SPP wave should start by defining the wave equations for transverse electric (TE) and transverse magnetic (TM) modes. In a one-dimensional problem, they can be obtained from Eq. 2.11 by considering a plane wave propagating in the x-direction along the flat interface between two media, as shown in Fig. 2.1. In this geometry, the boundary corresponds to the z = 0 plane, while the dielectric permittivity component in the y-direction ε_y doesn't have any variation in value. If $\beta = k_x$ is the propagation constant, the wave is described as $\vec{E}(x,y,z,t) = \vec{E}(z)e^{i\beta x}e^{-i\omega t}$ (note that in electrical engineering textbooks the time term is typically written with an opposite sign, i.e., $e^{i\omega t}$). Then the Helmholtz equation transforms to:

$$\frac{\partial^2 \vec{E}(z)}{\partial z^2} + \left(k_0^2 \varepsilon - \beta^2\right)\vec{E} = 0. \tag{2.12}$$

For the x-component of the fields, the curl equation Eq. 2.2c becomes:

$$\frac{\partial\left(E_z e^{i\beta x} e^{-i\omega t}\right)}{\partial y} - \frac{\partial\left(E_y e^{i\beta x} e^{-i\omega t}\right)}{\partial z} = -\frac{\partial\left(H_x e^{i\beta x} e^{-i\omega t}\right)}{\partial t}. \tag{2.13}$$

After taking a derivative on the right-hand side and cancelling the periodical time term $e^{-i\omega t}$, Eq. 2.13 is simplified to:

$$\frac{\partial E_z}{\partial y} - \frac{\partial E_y}{\partial z} = i\omega\mu_0 H_x. \tag{2.14a}$$

Now, if the same procedure is repeated coordinate-wise with the other field components in Eq. 2.2c-2.2d, they become:

$$\frac{\partial H_z}{\partial y} - \frac{\partial H_y}{\partial z} = -i\omega\varepsilon_0\varepsilon E_x \tag{2.15a}$$

$$\frac{\partial E_x}{\partial z} - \frac{\partial E_z}{\partial x} = i\omega\mu_0 H_y \tag{2.14b}$$

$$\frac{\partial H_x}{\partial z} - \frac{\partial H_z}{\partial x} = -i\omega\varepsilon_0\varepsilon E_y \tag{2.15b}$$

$$\frac{\partial E_y}{\partial x} - \frac{\partial E_x}{\partial y} = i\omega\mu_0 H_z \tag{2.14c}$$

$$\frac{\partial H_y}{\partial x} - \frac{\partial H_x}{\partial y} = -i\omega\varepsilon_0\varepsilon E_z. \tag{2.15c}$$

For a considered wave $\vec{E}(x,y,z,t)=\vec{E}(z)e^{i\beta x}e^{-i\omega t}$, which propagates in plane $z=0$ along the x-axis without any inhomogeneities in the y-direction, these equations reduce to:

$$-\frac{\partial E_y}{\partial z}=i\omega\mu_0 H_x \quad (2.16a) \qquad \frac{\partial H_y}{\partial z}=i\omega\varepsilon_0\varepsilon E_x \quad (2.17a)$$

$$\frac{\partial E_x}{\partial z}-i\beta E_z=i\omega\mu_0 H_y \quad (2.16b) \qquad \frac{\partial H_x}{\partial z}-i\beta H_z=-i\omega\varepsilon_0\varepsilon E_y \quad (2.17b)$$

$$i\beta E_y=i\omega\mu_0 H_z \quad (2.16c) \qquad i\beta H_y=-i\omega\varepsilon_0\varepsilon E_z\,. \quad (2.17c)$$

Based on this set of equations, the TE and TM modes can be determined as waves with only H_x, H_z and E_y, and E_x, E_z and H_y non-zero components respectively **[56]**. Now, the TE and TM sets of equations (Eq. 2.18a-c and Eq. 2.19a-c) can be rewritten as:

$$H_x=\frac{i}{\omega\mu_0}\frac{\partial E_y}{\partial z} \quad (2.18a) \qquad E_x=\frac{-i}{\omega\varepsilon_0\varepsilon}\frac{\partial H_y}{\partial z} \quad (2.19a)$$

$$H_z=\frac{\beta}{\omega\mu_0}E_y \quad (2.18b) \qquad E_z=\frac{-\beta}{\omega\varepsilon_0\varepsilon}H_y \quad (2.19b)$$

$$\frac{\partial^2 E_y}{\partial z^2}+\left(k_0^2\varepsilon-\beta^2\right)E_y=0 \quad (2.18c) \qquad \frac{\partial^2 H_y}{\partial z^2}+\left(k_0^2\varepsilon-\beta^2\right)H_y=0\,. \quad (2.19c)$$

2.3.3 SPPs on single interface

Let the upper half-space (positive z-direction) in Fig. 2.1 corresponds to a dielectric medium with $\varepsilon=\varepsilon_d(\omega)$ (which is real and positive) and the lower half-space (negative z-direction) corresponds to a metallic medium with $\varepsilon=\varepsilon_m(\omega)$ (which is complex and $\mathrm{Re}\,(\varepsilon_m(\omega))<0$ in the considered frequency region). A wave propagating along the x-axis on the interface between the metal and dielectric will be confined from the bottom because of the evanescent decay in the negative z-direction (metal is lossy). As is shown later in this chapter, the surface wave also becomes confined from the dielectric side because the wave vector in the insulator is smaller than the SPP propagation constant.

The TE solution for a surface wave obtained from Eq. 2.18c is defined by Eq. 2.20a-c in the upper half-space (z > 0) and by Eq. 2.21a-c in the lower half-space (z < 0):

$$E_y(z) = A_d e^{i\beta x} e^{-k_d z} \quad (2.20a) \qquad E_y(z) = A_m e^{i\beta x} e^{k_m z} \quad (2.21a)$$

$$H_x(z) = \frac{-iA_d}{\omega\mu_0} k_d e^{i\beta x} e^{-k_d z} \quad (2.20b) \qquad H_x(z) = \frac{iA_m}{\omega\mu_0} k_m e^{i\beta x} e^{k_m z} \quad (2.21b)$$

$$H_z(z) = \frac{A_d \beta}{\omega\mu_0} e^{i\beta x} e^{-k_d z} \quad (2.20c) \qquad H_z(z) = \frac{A_m \beta}{\omega\mu_0} e^{i\beta x} e^{k_m z}, \quad (2.21c)$$

where subscripts *m* and *d* denote metal and dielectric media respectively. The continuity of the electromagnetic components along the metal-dielectric interface (z = 0) means that Eq. 2.20a-c should be equal to the corresponding Eq. 2.21a-c, which (after dividing both sides on the same terms) gives:

$$A_d e^{-k_d z} = A_m e^{k_m z} \quad (2.22a)$$

$$-A_d k_d e^{-k_d z} = A_m k_m e^{-k_m z} \quad (2.22b)$$

$$A_d e^{-k_d z} = A_m e^{k_m z}. \quad (2.22c)$$

As can be seen, Eq. 2.22a is identical to Eq. 2.22c and, after substituting either of them in Eq. 2.22b, this equation transforms into:

$$-A_m k_d e^{-k_m z} = A_m k_m e^{-k_m z},$$

which can be further simplified to:

$$A_m(k_d + k_m) = 0. \quad (2.23)$$

Since Re (k_d) > 0 and Re (k_m) > 0 Eq. 2.23 is valid only if $A_m = 0$ and, consequently, $A_d = 0$. Thus, TE polarization doesn't support any surface modes.

The TM solution for Eq. 2.19c can be found in a similar fashion. Eq. 2.24a-c and Eq. 2.25a-c describe the field components in the upper half-space (z > 0) and lower half-space (z < 0) respectively as:

$$H_y(z) = A_d e^{i\beta x} e^{-k_d z} \tag{2.24a}$$

$$H_y(z) = A_m e^{i\beta x} e^{k_m z} \tag{2.25a}$$

$$E_x(z) = \frac{iA_d}{\omega\varepsilon_0\varepsilon_d} k_2 e^{i\beta x} e^{-k_d z} \tag{2.24b}$$

$$E_x(z) = \frac{-iA_m}{\omega\varepsilon_0\varepsilon_m} k_m e^{i\beta x} e^{-k_m z} \tag{2.25b}$$

$$E_z(z) = \frac{-A_d\beta}{\omega\varepsilon_0\varepsilon_2} e^{i\beta x} e^{-k_2 z} \tag{2.24c}$$

$$E_z(z) = \frac{-A_m\beta}{\omega\varepsilon_0\varepsilon_m} e^{i\beta x} e^{k_m z}. \tag{2.25c}$$

Again, after using the conditions of continuity of D_z and H_y along the interface of metal and dielectric (z = 0), these equations are transformed to:

$$A_d e^{-k_d z} = A_m e^{k_m z} \tag{2.26a}$$

$$A_d \frac{k_d}{\varepsilon_d} e^{-k_d z} = -A_m \frac{k_m}{\varepsilon_m} e^{-k_m z} \tag{2.26b}$$

$$-A_d e^{-k_d z} = -A_m e^{-k_m z}. \tag{2.26c}$$

The substitution of Eq. 2.26a (or Eq. 2.26c) in Eq. 2.26b results in the simple relation between the wave vectors and dielectric permittivities of the media:

$$\frac{k_d}{k_m} = -\frac{\varepsilon_d}{\varepsilon_m}. \tag{2.27}$$

The wave vectors k_d and k_m must satisfy the wave equation (Eq. 2.19c), which means that:

$$k_d^2 = \beta^2 - k_0^2\varepsilon_d \tag{2.28a}$$

$$k_m^2 = \beta^2 - k_0^2\varepsilon_m. \tag{2.28b}$$

Combining these equations in Eq. 2.27 leads to:

$$\beta = k_0\sqrt{\frac{\varepsilon_1\varepsilon_2}{\varepsilon_1+\varepsilon_2}}. \tag{2.29}$$

Eq. 2.29 describes the propagation of a surface electromagnetic wave on the interface between metal and dielectric media. Since no modes exist in TE polarization, it could be concluded that SPPs are only obtained for TM polarization. Depending on the value of the SPP wave vector, surface plasmons at first behave similarly to photons (for frequencies below mid-infrared), but then approach the surface plasma frequency given by **[25]**:

$$\omega_{sp} = \frac{\omega_p}{\sqrt{1+\varepsilon_d}} \tag{2.30}$$

$$\omega_p = \sqrt{\frac{n_e q_e^2}{\varepsilon_0 m}}, \tag{2.31}$$

where ω_p is the plasma frequency of the free electron gas, m is an effective optical electron mass, q_e is an elementary electron charge and n_e is the electron density.

The dispersion relations of SPP waves on silver/air (blue solid line) and silver/quartz (black dashed line with dots) interfaces are shown in Fig. 2.2. The silver is modelled using the experimentally measured optical constants taken from **[62]** and only the real part of SPP wave vector is plotted. The abscissa axis in the figure is given in normalized units of βc and the axis of ordinates in ω. As can be seen from this plot, for small wave vectors, the corresponding SPP acts similarly to a wave propagating in either air (cyan dashed line) or quartz (grey line with dots). The large oscillations in the wave vector profiles occur around a plasmon's resonant frequency.

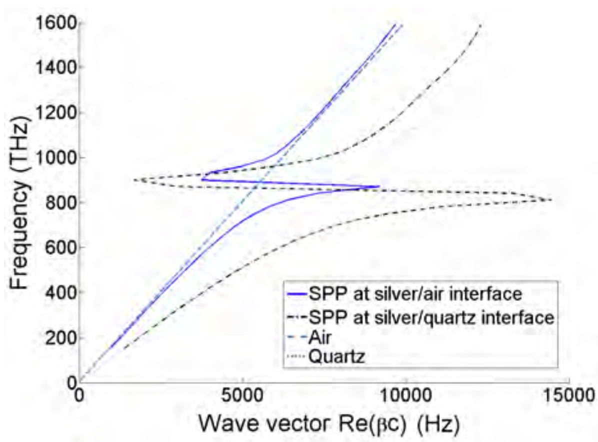

Fig. 2.2 – Dispersion relations of SPP waves

As real materials are intrinsically lossy, surface plasmon waves inevitably decay as they propagate along the surface of a conductor. The SPP propagation distance is calculated as $L = (2\mathrm{Im}\,(\beta))^{-1}$ and depends on the particular material combination. For example, at a silver/air boundary, the propagation distance is only $L \approx 16$ μm at $\lambda_0 = 450$ nm and then increases for longer wavelengths, becoming $L \approx 1080$ μm at $\lambda_0 = 1500$ nm **[56]**.

The energy confinement of the plasmonic mode is characterized by the evanescent attenuation lengths of the field components perpendicular to the interface between two media (i.e., along the *z*-axis in Fig. 2.1) that is equal to $\hat{z} = 1 / |k_z|$. The attenuation lengths also depend on the wavelength, which at $\lambda_0 = 450$ nm is $\hat{z} \approx 180$ nm, but at $\lambda_0 = 1500$ nm already increases to $\hat{z} \approx 2600$ nm **[56]**. Thereby, a longer propagation distance comes at a cost of a weaker field confinement.

2.3.4 SPPs on multiple interfaces

SPP modes can also exist in multilayer structures consisting of alternating metal and dielectric films. In such geometry, each interface is capable of supporting an independent SPP wave and, if the thicknesses of the layers are less than the attenuation length $\hat{z}$, the interaction between individual plasmonic modes results in the formation of a coupled mode, with its dispersion equation revealing the existence of two independent solutions denoted as ω_- and ω_+. The first solution corresponds to an even vector parity ($E_x(z)$ is an even function, while $H_y(z)$ and $E_z(z)$ are odd) and the second to an odd vector parity ($E_x(z)$ is an odd function, while $H_y(z)$ and $E_z(z)$ are even) **[56]**. Assuming lossless metal in a dielectric-metal-dielectric (DMD) geometry with a conductor thickness of $2h$ and for large wave vectors, the coupled mode frequency is limited by:

$$\omega_- = \frac{\omega_p}{\sqrt{1+\varepsilon_d}} \sqrt{1 - \frac{2\varepsilon_d e^{-2\beta h}}{1+\varepsilon_d}} \tag{2.32a}$$

$$\omega_+ = \frac{\omega_p}{\sqrt{1+\varepsilon_d}} \sqrt{1 + \frac{2\varepsilon_d e^{-2\beta h}}{1+\varepsilon_d}} \,. \tag{2.32b}$$

Such coupled modes are typically used in plasmonic metal-dielectric-metal (MDM) waveguides **[63]** and are further discussed in Chapter 6 for a case of a metamaterial slot waveguide. The other examples of SPP-based plasmonic devices include sensors **[64]**, gratings **[65]** and other sub-wavelength optic components **[66-68]**.

2.3.5 Localized surface plasmons

Localized surface plasmons are non-propagating excitations (in contrast to *propagating* SPP) of the free electrons that occur in metallic nano-structures coupled to the external electromagnetic field. Due to the small sizes of nano-particles, the curvatures of their surfaces affect the generation of LSPs, and, thus, localized surface plasmon resonance can be directly excited by incident radiation **[56]**.

In the simplest case of quasi-static approximation, an illuminated spherical nano-particle with dielectric permittivity ε and diameter d ($d << \lambda$, λ is the wavelength of light in the surrounding media) can be treated as an electric dipole. Then, the field potential outside the particle Φ_{out} and dipole moment p can be written as **[56]**:

$$\Phi_{out} = -E_0 r \cos\theta + \frac{\vec{p}\cdot\vec{r}}{4\pi\varepsilon_0\varepsilon_{out} r^3} \tag{2.33}$$

$$\vec{p} = 0.5\pi\varepsilon_0\varepsilon_{out} d^3 \frac{\varepsilon - \varepsilon_{out}}{\varepsilon + 2\varepsilon_{out}} \vec{E}_0 . \tag{2.34}$$

Here ε_{out} is the dielectric permittivity of the surrounding medium and the polar coordinates, r and θ, correspond to the radius vector and azimuthal angle (which is calculated in respect to the direction of the external field E_0). The dipole moment and E_0 are also linked via:

$$\vec{p} = \varepsilon_0 \varepsilon_m \alpha \vec{E}_0 ,$$

which gives the following expression for a polarizability α:

$$\alpha = 0.5\pi d^3 \frac{\varepsilon(\omega) - \varepsilon_{out}}{\varepsilon(\omega) + 2\varepsilon_{out}} . \tag{2.35}$$

The polarizability function exhibits resonance behaviour, which is associated with the excitation of LSPs, and reaches its maximum, when the denominator becomes minimum. Assuming a slowly varying or small Im (ε), this resonant condition can be simplified to:

$$\mathrm{Re}(\varepsilon(\omega)) = -2\varepsilon_{out} , \tag{2.36}$$

which is known as the Fröhlich condition for a spherical metallic nano-particle in a quasi-static approximation. In the literature, the corresponding excited mode is referred to as a dipole surface plasmon **[25]**.

A spherical nano-particle is a special case of a more general ellipsoid shape. Ellipsoid with semi-axes $a_1 \geq a_2 \geq a_3$, which is placed in the origin of a Cartesian coordinate system and is aligned with its axes, is defined by a standard equation as:

$$\frac{x^2}{a_1^2}+\frac{y^2}{a_2^2}+\frac{z^2}{a_3^2}=1\,.$$

The polarizability in such geometry can be calculated as **[69]**:

$$\alpha_i = 4\pi a_1 a_2 a_3 \frac{\varepsilon(\omega)-\varepsilon_{out}}{3L_i\left(\varepsilon(\omega)-\varepsilon_{out}\right)+3\varepsilon_{out}} \tag{2.37}$$

$$L_i = 0.5 a_1 a_2 a_3 \int_0^\infty \frac{dq}{\left(a_i^2+q\right)\sqrt{\left(a_1^2+q\right)\left(a_2^2+q\right)\left(a_3^2+q\right)}}\,. \tag{2.38}$$

Here index *i* represents the component along one of the main axes (i.e., *x*, *y* or *z*) and the geometrical factor L_i is normalized so that $\Sigma L_i = 1$. As, in the case of a sphere, $a_1 = a_2 = a_3 = 0.5d$ and $L_1 = L_2 = L_3 = 1/3$, thereby, Eq. 2.37 reduces to the earlier obtained Eq. 2.35. The other special case of an ellipsoid is a spheroid obtained by rotating an ellipse along one of its principal axes. For example, a prolate spheroid with $a_2 = a_3$ has a polarizability α_1 along its *x*-axis (i = 1) equal to:

$$\alpha_1 = 4\pi a_1 a_2^2 \frac{\varepsilon(\omega)-\varepsilon_{out}}{3L_1\left(\varepsilon(\omega)-\varepsilon_{out}\right)+3\varepsilon_{out}} \tag{2.39}$$

$$L_1 = \frac{a_1 a_2^2}{a_2^2-a_1^2}\left(\frac{1}{a_1}+\frac{1}{\sqrt{a_2^2-a_1^2}}\left(\arctan\frac{a_1}{\sqrt{a_2^2-a_1^2}}-\frac{\pi}{2}\right)\right). \tag{2.40}$$

The absolute value of polarizability as a function of frequency is shown in Fig. 2.3 for spherical (d = 10 nm) and spheroid ($a_1 = d/2$, $a_2 = a_3 = d/16$) shapes. The nano-particle material is assumed to be silver modelled according to **[62]** and the ambient medium is treated as air ($\varepsilon_{out} = 1$). As can be seen, for this geometry, the spheroid is excited at lower resonant frequencies than the spherical particle. It should be noted that the magnitudes of the resonant polarizabilities are of the same order of 10^{-22} A^2s^4/kg for both particles (which is reasonable because α is proportional to d^3).

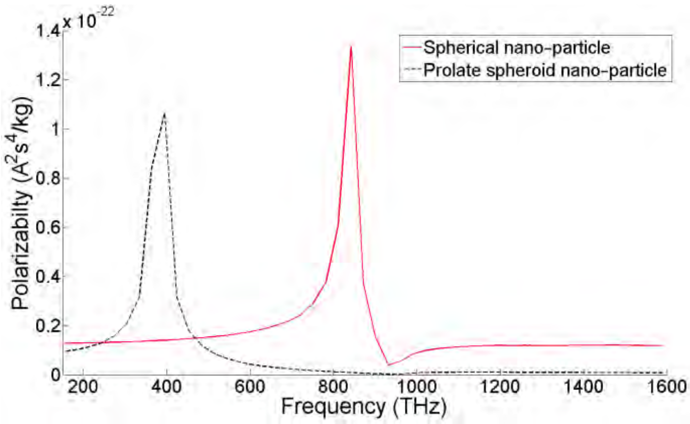

Fig. 2.3 – Polarizability magnitudes for spherical and spheroid ($a_2 = a_3$) nano-particles

In practice, LSP excitation plays a crucial role in applications involving:

1) Nano-particles (bio-medical applications for imaging **[27, 28]** or cancer treatment **[29, 30]**, optical tweezers **[26],** solar cells **[70, 71]** and metallic nano-particle waveguides **[72]**);
2) Nano-antennas (including dipole **[73, 74]**, bow-tie **[75]**, Yagi-Uda **[76, 77]** and other antennas);
3) Metamaterials (fishnet **[78]** and split ring resonators **[79]**);
4) SERS-based sensors **[80, 81]**.

Two of the plasmonic devices further considered in the present research are titanium and gold dipole nano-antennas (Chapter 5) and a fishnet metamaterial (Chapter 7).

2.4 Plasmonic heating

2.4.1 Conversion of light into heat

The plasmonic heating could be approximated by applying the Poynting's theorem, which represents the conservation of electromagnetic energy in an absorptive medium. According to it, the energy transmission rate per unit volume equals to the rate of work done on a charge distribution plus the energy flux leaving the considered volume **[82]**. The Poynting's theorem is derived from the Maxwell's equations (Eq. 2.2a-2.2d) and can be given in the following form:

$$\int_{\delta V} \vec{S} \cdot d\left(\delta\vec{V}\right) = -\int_{V} \left(\vec{E} \cdot \frac{\partial \vec{D}}{\partial t} + \vec{H} \cdot \frac{\partial \vec{B}}{\partial t} \right) dV \tag{2.41a}$$

$$\vec{S} = \vec{E} \times \vec{H} \ , \tag{2.41b}$$

where δV is the closed surface that surrounds the space region with volume V, and S is the Poynting vector representing the energy flux. It should be noted that Eq. 2.41a is typically written having a term $-\int_V J \cdot E dV$ on the right-hand side, which corresponds to the contribution of conduction current J, however in the following discussion this term is instead implicitly contained in the dielectric response **[83].**

For a lossy and dispersive material, the electric polarization P induced by an external electric field can be found as **[24]**:

$$\frac{\partial^2 \vec{P}}{\partial t^2} + \gamma_e \frac{\partial \vec{P}}{\partial t} + \omega_e^2 \vec{P} = \varepsilon_0 \omega_{ep}^2 \vec{E} \ . \tag{2.42}$$

Here γ_e is the electric damping constant, ω_e and ω_{ep} are the resonant and plasma frequencies of electric oscillators. The similar expression can be also obtained for magnetization M:

$$\frac{\partial^2 \vec{M}}{\partial t^2} + \gamma_m \frac{\partial \vec{M}}{\partial t} + \omega_m^2 \vec{M} = \omega_{mp}^2 \vec{H} \ , \tag{2.43}$$

where magnetic components γ_m, ω_m and ω_{mp} have the same meaning as electric counterparts and are used to describe the magnetic oscillators. Now, after rewriting Eq. 2.42 and Eq. 2.43 by using Eq. 2.4a and Eq. 2.4b, and substituting the results into Eq. 2.41b, the latter, finally, becomes **[24]**:

$$-\int_V \frac{\partial u}{\partial t} dV = \int_{\delta V} \left(\vec{E} \times \vec{H}\right) \cdot d\left(\delta V\right) + \int_V \left(\frac{\gamma_e}{\varepsilon_0 \omega_{ep}^2} \left| \frac{\partial \vec{P}}{\partial t} \right|^2 + \frac{\mu_0 \gamma_m}{\omega_{mp}^2} \left| \frac{\partial \vec{M}}{\partial t} \right|^2 \right) dV \tag{2.44}$$

$$u = 0.5\varepsilon_0 |E|^2 + 0.5\mu_0 |H|^2 + \frac{1}{2\varepsilon_0 \omega_{ep}^2} \left(\left| \frac{\partial \vec{P}}{\partial t} \right|^2 + \omega_e^2 |P|^2 \right) + \frac{\mu_0}{2\omega_{mp}^2} \left(\left| \frac{\partial \vec{M}}{\partial t} \right|^2 + \omega_m^2 |M|^2 \right). \tag{2.45}$$

Here u is the total energy density, which takes into account both electric and magnetic excitations. Eq. 2.44 means that the energy flux through the boundaries δV plus the total absorption losses in the system (represented by both electric and magnetic components in the second term of Eq. 2.44) is equal to the negative time derivative of the electromagnetic energy within considered volume **[24]**.

Now, the time-averaged dissipative energy density q can be obtained from Eq. 2.44 as:

$$q = q_e + q_m = \left\langle \frac{\gamma_e}{\varepsilon_0 \omega_{ep}^2} \left| \frac{\partial \vec{P}}{\partial t} \right|^2 + \frac{\mu_0 \gamma_m}{\omega_{mp}^2} \left| \frac{\partial \vec{M}}{\partial t} \right|^2 \right\rangle =$$

$$= 0.5\varepsilon_0 \omega \operatorname{Im}(\varepsilon(\omega))|E|^2 + 0.5\mu_0 \omega \operatorname{Im}(\mu(\omega))|H|^2 , \tag{2.46}$$

where q_e and q_m correspond to electric and magnetic components of the dissipative energy. For a nonmagnetic medium Eq. 2.46 simplifies to:

$$q = q_e = 0.5\varepsilon_0 \omega \operatorname{Im}(\varepsilon(\omega))|E|^2 . \tag{2.47}$$

For a case of a plasmonic device the incident light always becomes scattered and/or absorbed. Thereby, it could be concluded that the dissipated energy of the electromagnetic wave eventually converts into heat Q:

$$A \equiv Q = \int_V q dV . \tag{2.48}$$

Here A is the total absorption of the plasmonic structure, which could be found, for example, from scattering matrix as is shown in Chapter 7.

2.4.2 Thermal modelling in plasmonic structures

The heat conduction in medium can be described by introducing a heat flux density vector q, which corresponds to the rate of heat energy passing through a given surface per unit area **[23]**. Assuming a one-dimensional problem, in which the heat propagates along the x-axis in a symmetrical channel with length dx and cross-section area S (Fig. 2.4), the total amount of heat transferred during the time interval dt becomes:

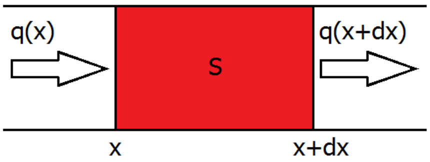

Fig. 2.4 – Heat transfer in one-dimensional case

$$Q = \left(q(x) - q(x+dx)\right)Sdt = -\frac{\partial q}{\partial x} Sdxdt \,. \tag{2.49}$$

The same amount of heat can be also found by considering the temperature changes inside the channel:

$$Q = \rho S c_v dT \,, \tag{2.50}$$

where ρ is the density of the channel material and c_v is its volumetric heat capacity. Combining Eq. 2.49 and Eq. 2.50 and cancelling the same terms gives:

$$\rho c_v \frac{\partial T}{\partial t} = -\frac{\partial q}{\partial x} \,. \tag{2.51}$$

The heat flux density is linked to the temperature difference by the Fourier's law **[23]**:

$$q = -\chi \frac{\partial T}{\partial x} \,. \tag{2.52}$$

Here χ is a positive material parameter called thermal conductivity. Inserting Eq. 2.52 into Eq. 2.51 leads to the heat conduction equation:

$$\rho c_v \frac{\partial T}{\partial t} = \frac{\partial}{\partial x}\left(\chi \frac{\partial T}{\partial x}\right). \tag{2.53}$$

In a uniform medium where χ doesn't depend on a spatial coordinate, it could be factored outside the derivative sign:

$$\rho c_v \frac{\partial T}{\partial t} = \chi \frac{\partial^2 T}{\partial x^2} \,. \tag{2.54}$$

For a more general case, when the heat propagates in the arbitrary direction and other external heat sources exist, Eq. 2.54 should be rewritten as:

$$\rho c_v \frac{\partial T}{\partial t} = \chi \nabla^2 T(r) + Q_s(r), \tag{2.55}$$

where $Q_s(r)$ represents the total source heat density, which becomes strongly non-uniform for a plasmonic device (this happens because hot-spots may occur simultaneously in multiple regions across the structure **[84]**). Assuming the steady state regime **[85]** the time derivative turns zero and the heating in system becomes governed by the Poisson's equation:

$$\chi \nabla^2 T(r) = -Q_s(r), \tag{2.56}$$

The general solution to Eq. 2.56 can be obtained by using the scalar thermal Green functions as shown in [**22**], however a further detailed discussion on this topic will be out of the scope of present work, since the heat propagation inside plasmonic devices will be similar to that of the conventional bulk materials.

2.5 Summary

This chapter studies the foundations of plasmonics by deriving the Helmholtz and SPP wave equations from the Maxwell's equations. It is shown that the SPP mode can only exist for TM polarization (E_x, E_z, and H_y), which is important for further experiment design. The dispersion relations are demonstrated for both single and double interfaces, and the link between the energy confinement and propagation distance is discussed. The excitation of LSPs for spherical and ellipsoid nano-particles is also addressed, with the polarizability as a function of an external driving field provided for both cases. Finally, the origin of plasmonic heating is explained and the thermal dissipative energy density is linked with the amplitude and frequency of the incident light.

While the outlined equations provide a useful insight in the underlying physical processes, in practice, the analysis of plasmon excitations and the calculation of temperature distributions are typically performed by implementing specially designed numerical software packages, which are discussed in the next chapter. Although the presented material covers only the general issues in light-material interactions, the more specified cases, such as slot waveguide operation or formation of microbumps, are not discussed yet, and are to be considered in the following chapters.

Chapter 3 – Numerical modelling

3.1 Introduction

This chapter describes the numerical algorithms used during the conducted research. Firstly, the equations of finite-difference time-domain (FDTD) method are derived from the Maxwell's equations and the concept of Yee cell is explained. Secondly, the commercial software RSoft FullWAVE is in details discussed and the material dispersion model is provided. Thirdly, MATLAB codes for data processing are briefly outlined and, finally, the information on thermal modelling by using COMSOL software is described.

3.2 Numerical methods

3.2.1 Introduction to FDTD

The FDTD method is a popular computational approach in the electrodynamics of a continuous medium, which relies on the numerical solutions to the differential Maxwell's equations. It was initially based on the Yee algorithm proposed in 1966 **[86]** for linear and lossless media. Later, this method was generalized by Taflove for more complex cases of anisotropic materials **[87]**.

Originally, the necessity to find solutions to Maxwell's equations was motivated by military defence applications during World War II and the following Cold War. The rapid advances in radar technologies aimed at early aircraft and missile recognition required a fast and simple algorithm to interpret the acquired data. On the other hand, low-detection and stealth technologies demanded an understanding of materials' scattering properties, which, in turn, led to the need to solve the Maxwell's equations. Since the last decade of the 20^{th} century, the interest in computational electrodynamics has shifted to civil and electrical engineering in commercial applications, with particular importance placed on communications and computing areas. As for the research field, FDTD has become widely used for studying photonic crystals, metamaterials, waveguides, integrated optic devices, antennas and other plasmonics structures **[88]**.

3.2.2 Derivation of FDTD equations

The FDTD method could be explained by using the approach discussed in **[87]**. Assuming the absence of external charges ($\rho_{ext} = 0$), the Maxwell's equations Eq. 2.2a-2.2d can be rewritten in the following form:

$$\nabla \cdot \vec{D} = 0 \quad (3.1a) \qquad \nabla \cdot \vec{B} = 0 \quad (3.1b)$$

$$\frac{\partial \vec{B}}{\partial t} = -\nabla \times \vec{E} - \vec{M} \quad (3.1c) \qquad \frac{\partial \vec{D}}{\partial t} = \nabla \times \vec{H} - \vec{J}\,, \quad (3.1d)$$

where M is the equivalent magnetic current density, which is added to obtain symmetry of the equations. The electric and equivalent magnetic current densities can be interpreted as source-like functions (J_0 and M_0 respectively) with losses introduced through electric conductivity σ and equivalent magnetic loss σ^* as:

$$\vec{J} = \vec{J}_0 + \sigma\vec{E} \quad (3.2a) \qquad \vec{M} = \vec{M}_0 + \sigma^*\vec{H}\,. \quad (3.2b)$$

Substituting Eq. 3.2a and Eq. 3.2b in Eq. 3.1c and Eq. 3.1d, and assuming linear, isotropic and non-dispersive media gives:

$$\frac{\partial \vec{H}}{\partial t} = -\frac{1}{\mu}\nabla \times \vec{E} - \frac{1}{\mu}(\vec{M}_0 + \sigma^*\vec{H}) \quad (3.3)$$

$$\frac{\partial \vec{E}}{\partial t} = \frac{1}{\varepsilon}\nabla \times \vec{H} - \frac{1}{\varepsilon}(\vec{J}_0 + \sigma\vec{E})\,. \quad (3.4)$$

Now, if written in Cartesian coordinates, these equations become:

$$\frac{\partial H_x}{\partial t} = \frac{1}{\mu}\left[\frac{\partial E_y}{\partial z} - \frac{\partial E_z}{\partial y} - \left(M_{0x} + \sigma^* H_x\right)\right] \quad (3.5a)$$

$$\frac{\partial H_y}{\partial t} = \frac{1}{\mu}\left[\frac{\partial E_z}{\partial x} - \frac{\partial E_x}{\partial z} - \left(M_{0y} + \sigma^* H_y\right)\right] \quad (3.5b)$$

$$\frac{\partial H_z}{\partial t} = \frac{1}{\mu}\left[\frac{\partial E_x}{\partial y} - \frac{\partial E_y}{\partial x} - \left(M_{0z} + \sigma^* H_z\right)\right] \quad (3.5c)$$

$$\frac{\partial E_x}{\partial t} = \frac{1}{\varepsilon}\left[\frac{\partial H_z}{\partial y} - \frac{\partial H_y}{\partial z} - \left(J_{0x} + \sigma E_x\right)\right] \tag{3.6a}$$

$$\frac{\partial E_y}{\partial t} = \frac{1}{\varepsilon}\left[\frac{\partial H_x}{\partial z} - \frac{\partial H_z}{\partial x} - \left(J_{0y} + \sigma E_y\right)\right] \tag{3.6b}$$

$$\frac{\partial E_z}{\partial t} = \frac{1}{\varepsilon}\left[\frac{\partial H_y}{\partial x} - \frac{\partial H_x}{\partial y} - \left(J_{0z} + \sigma E_z\right)\right]. \tag{3.6c}$$

3.2.3 Yee algorithm

The Yee algorithm, which lies at the basis of the FDTD method, has some distinctive features that make its solution straightforward and robust. Firstly, the Maxwell's equations for both electric and magnetic fields are solved simultaneously rather than a single electric (or magnetic) field equation being solved separately at a given moment in time. Secondly, the Yee mesh cell is designed in such a way that each *E* (*H*) component is connected to four *H* (*E*) components, as shown in Fig. 3.1. Thirdly, the computation is performed using a "leapfrogging" time approach, i.e., at a fixed moment in time, all *E*-components are calculated based on the *H*-data stored in memory, and, in the next time step, all the *H*-components are computed from previously acquired *E*-data and then the cycle is repeated again to calculate the *E*-field **[87]**.

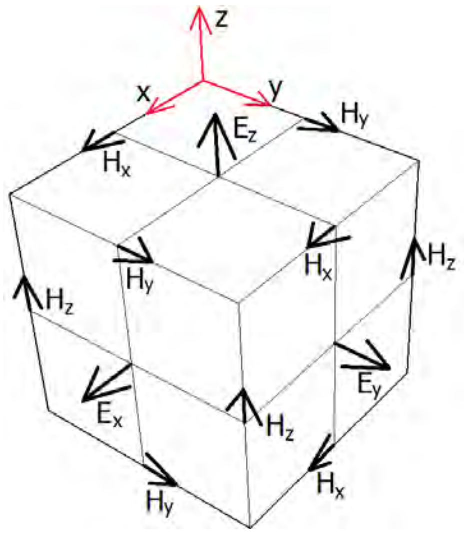

Fig. 3.1 – Three-dimensional Yee cell

The Yee algorithm can be explained by taking an arbitrary function *f* at a discrete time ($n\Delta t$) and space ($i\Delta x$, $j\Delta y$, $k\Delta z$) point as:

$$f\left(i\Delta x, j\Delta y, k\Delta z, n\Delta t\right) = f^{n}_{i,j,k}, \tag{3.7}$$

where Δ symbol denotes the step in either of the coordinates or time, and *i*, *j*, *k* and *n* are integers. Then, the first derivative in the *x*-direction is expressed as:

$$\frac{\partial f}{\partial x}(i\Delta x, j\Delta y, k\Delta z, n\Delta t) = \frac{f^{n}_{i+0.5,j,k} - f^{n}_{i-0.5,j,k}}{\Delta x} + O\left[(\Delta x)^2\right]. \tag{3.8}$$

Note that, although the increment in the *x*-direction is $\pm 0.5\Delta x$, the spacing between the values of function *f* still remains Δx. The reason for doing this is to rewrite the derivative as a central difference. Similarly, the time derivative can be written as:

$$\frac{\partial f}{\partial t}(i\Delta x, j\Delta y, k\Delta z, n\Delta t) = \frac{f^{n+0.5}_{i,j,k} - f^{n-0.5}_{i,j,k}}{\Delta t} + O\left[(\Delta t)^2\right]. \tag{3.9}$$

Now, a same approach is used for Eq. 3.5a-3.6c. After substituting and regrouping, the set of finite-difference equations obtained for the magnetic field components becomes **[87]**:

$$H^{n+1}_{x,i-0.5,j+1,k+1} = \left(\frac{1-\dfrac{\sigma^{*}_{i-0.5,j+1,k+1}\Delta t}{2\mu_{i-0.5,j+1,k+1}}}{1+\dfrac{\sigma^{*}_{i-0.5,j+1,k+1}\Delta t}{2\mu_{i-0.5,j+1,k+1}}}\right) H^{n}_{x,i-0.5,j+1,k+1} - M^{n+0.5}_{0x,i-0.5,j+1,k+1}\left(\frac{\dfrac{\Delta t}{\mu_{i-0.5,j+1,k+1}}}{1+\dfrac{\sigma^{*}_{i-0.5,j+1,k+1}\Delta t}{2\mu_{i-0.5,j+1,k+1}}}\right) +$$

$$+\left(\frac{\dfrac{\Delta t}{\mu_{i-0.5,j+1,k+1}}}{1+\dfrac{\sigma^{*}_{i-0.5,j+1,k+1}\Delta t}{2\mu_{i-0.5,j+1,k+1}}}\right)\left(\frac{E^{n+0.5}_{y,i-0.5,j+1,k+1.5} - E^{n+0.5}_{y,i-0.5,j+1,k+1.5}}{\Delta z} - \frac{E^{n+0.5}_{z,i-0.5,j+1.5,k+1} - E^{n+0.5}_{z,i-0.5,j+0.5,k+1}}{\Delta y}\right) \tag{3.10a}$$

$$H^{n+1}_{y,i,j+0.5,k+1} = \left(\frac{1-\dfrac{\sigma^{*}_{i,j+0.5,k+1}\Delta t}{2\mu_{i,j+0.5,k+1}}}{1+\dfrac{\sigma^{*}_{i,j+0.5,k+1}\Delta t}{2\mu_{i,j+0.5,k+1}}}\right) H^{n}_{y,i,j+0.5,k+1} - M^{n+0.5}_{0y,i,j+0.5,k+1}\left(\frac{\dfrac{\Delta t}{\mu_{i,j+0.5,k+1}}}{1+\dfrac{\sigma^{*}_{i,j+0.5,k+1}\Delta t}{2\mu_{i,j+0.5,k+1}}}\right) +$$

$$+\left(\frac{\frac{\Delta t}{\mu_{i,j+0.5,k+1}}}{1+\frac{\sigma^{*}_{i,j+0.5,k+1}\Delta t}{2\mu_{i,j+0.5,k+1}}}\right)\left(\frac{E^{n+0.5}_{z,i+0.5,j+0.5,k+1}-E^{n+0.5}_{z,i-0.5,j+0.5,k+1}}{\Delta x}-\frac{E^{n+0.5}_{x,i,j+0.5,k+1.5}-E^{n+0.5}_{x,i,j+0.5,k+0.5}}{\Delta z}\right) \tag{3.10b}$$

$$H^{n+1}_{z,i,j+1,k+0.5}=\left(\frac{1-\frac{\sigma^{*}_{i,j+1,k+0.5}\Delta t}{2\mu_{i,j+1,k+0.5}}}{1+\frac{\sigma^{*}_{i,j+1,k+0.5}\Delta t}{2\mu_{i,j+1,k+0.5}}}\right)H^{n}_{z,i,j+1,k+0.5}-M^{n+0.5}_{0z,i,j+1,k+0.5}\left(\frac{\frac{\Delta t}{\mu_{i,j+1,k+0.5}}}{1+\frac{\sigma^{*}_{i,j+1,k+0.5}\Delta t}{2\mu_{i,j+1,k+0.5}}}\right)+$$

$$+\left(\frac{\frac{\Delta t}{\mu_{i,j+1,k+0.5}}}{1+\frac{\sigma^{*}_{i,j+1,k+0.5}\Delta t}{2\mu_{i,j+1,k+0.5}}}\right)\left(\frac{E^{n+0.5}_{x,i,j+1.5,k+0.5}-E^{n+0.5}_{x,i,j+0.5,k+0.5}}{\Delta y}-\frac{E^{n+0.5}_{y,i+0.5,j+1,k+0.5}-E^{n+0.5}_{y,i-0.5,j+1,k+0.5}}{\Delta x}\right), \tag{3.10c}$$

and, for the electric field components:

$$E^{n+0.5}_{x,i,j+0.5,k+0.5}=\left(\frac{1-\frac{\sigma_{i,j+0.5,k+0.5}\Delta t}{2\varepsilon_{i,j+0.5,k+0.5}}}{1+\frac{\sigma_{i,j+0.5,k+0.5}\Delta t}{2\varepsilon_{i,j+0.5,k+0.5}}}\right)E^{n-0.5}_{x,i,j+0.5,k+0.5}-J^{n}_{0x,i,j+0.5,k+0.5}\left(\frac{\frac{\Delta t}{\varepsilon_{i,j+0.5,k+0.5}}}{1+\frac{\sigma_{i,j+0.5,k+0.5}\Delta t}{2\varepsilon_{i,j+0.5,k+0.5}}}\right)+$$

$$+\left(\frac{\frac{\Delta t}{\varepsilon_{i,j+0.5,k+0.5}}}{1+\frac{\sigma_{i,j+0.5,k+0.5}\Delta t}{2\varepsilon_{i,j+0.5,k+0.5}}}\right)\left(\frac{H^{n}_{z,i,j+1,k+0.5}-H^{n}_{z,i,j,k+0.5}}{\Delta y}-\frac{H^{n}_{y,i,j+0.5,k+1}-H^{n}_{y,i,j+0.5,k}}{\Delta z}\right) \tag{3.11a}$$

$$E^{n+0.5}_{y,i-0.5,j+1,k+0.5}=\left(\frac{1-\frac{\sigma_{i-0.5,j+1,k+0.5}\Delta t}{2\varepsilon_{i-0.5,j+1,k+0.5}}}{1+\frac{\sigma_{i-0.5,j+1,k+0.5}\Delta t}{2\varepsilon_{i-0.5,j+1,k+0.5}}}\right)E^{n-0.5}_{y,i-0.5,j+1,k+0.5}-J^{n}_{0y,i-0.5,j+1,k+1}\left(\frac{\frac{\Delta t}{\varepsilon_{i-0.5,j+1,k+0.5}}}{1+\frac{\sigma_{i-0.5,j+1,k+0.5}\Delta t}{2\varepsilon_{i-0.5,j+1,k+0.5}}}\right)+$$

$$+\left(\frac{\frac{\Delta t}{\varepsilon_{i-0.5,j+1,k+0.5}}}{1+\frac{\sigma_{i-0.5,j+1,k+0.5}\Delta t}{2\varepsilon_{i-0.5,j+1,k+0.5}}}\right)\left(\frac{H^{n}_{x,i-0.5,j+1,k+1}-H^{n}_{x,i-0.5,j+1,k}}{\Delta z}-\frac{H^{n}_{z,i,j+1,k+0.5}-H^{n}_{z,i-1,j+1,k+0.5}}{\Delta x}\right) \tag{3.11b}$$

$$E^{n+0.5}_{z,i-0.5,j+0.5,k+1} = \left(\frac{1 - \dfrac{\sigma_{i-0.5,j+0.5,k+1}\Delta t}{2\varepsilon_{i-0.5,j+0.5,k+1}}}{1 + \dfrac{\sigma_{i-0.5,j+0.5,k+1}\Delta t}{2\varepsilon_{i-0.5,j+0.5,k+1}}} \right) E^{n-0.5}_{z,i-0.5,j+0.5,k+1} - J^{n}_{0z,i-0.5,j+0.5,k+1} \left(\frac{\dfrac{\Delta t}{\varepsilon_{i-0.5,j+0.5,k+1}}}{1 + \dfrac{\sigma_{i-0.5,j+0.5,k+1}\Delta t}{2\varepsilon_{i-0.5,j+0.5,k+1}}} \right) +$$

$$+ \left(\frac{\dfrac{\Delta t}{\varepsilon_{i-0.5,j+0.5,k+1}}}{1 + \dfrac{\sigma_{i-0.5,j+0.5,k+1}\Delta t}{2\varepsilon_{i-0.5,j+0.5,k+1}}} \right) \left(\frac{H^{n}_{y,i,j+0.5,k+1} - H^{n}_{y,i-1,j+0.5,k+1}}{\Delta x} - \frac{H^{n}_{x,i-0.5,j+1,k+1} - H^{n}_{x,i-0.5,j,k+1}}{\Delta y} \right). \qquad (3.11c)$$

These equations provide an important link between the field components calculated at different time and space points. For example, E_x at a moment in time (n+0.5) depends only on:

1) Its value in the previous time step (n-0.5);
2) The values of the magnetic field in the previous time step (n) at adjacent space points;
3) The values of the electric current source in the previous time step (n) at adjacent space points.

Fig. 3.2 illustrates a simple 1D space-time chart of the Yee algorithm **[87]**. As previously discussed, in different time steps, the electric (magnetic) fields are calculated from the values obtained in the previous time steps for the magnetic (electric) fields.

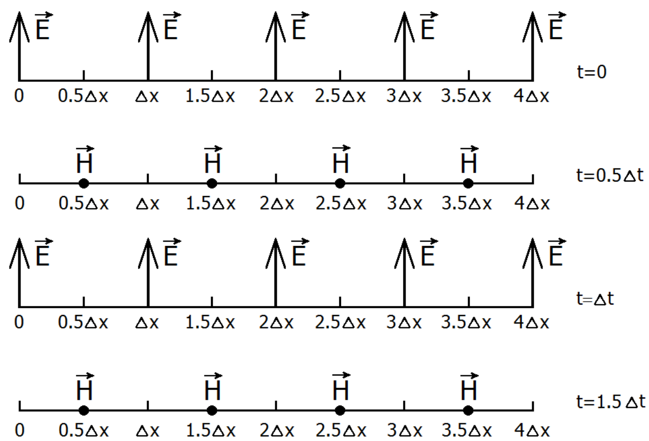

Fig. 3.2 – One-dimensional space-time chart of Yee algorithm

The stability of the FDTD method is determined by satisfying the Courant–Friedrichs–Lewy (CFL) condition, which means not exceeding the value of the Courant number S_{max} **[89]**. If this condition is not met the numerical scheme quickly diverges producing the incorrect results of the fields' values. For a *n*-dimensional problem with a spatial step along each axis denoted Δx_i, the CFL is condition is defined as:

$$S = \Delta t \sum_{i=1}^{n} \frac{c}{\Delta x_i} \leq S_{\max} . \tag{3.12}$$

3.2.4 RSoft FullWAVE

There are many software packages that calculate the electromagnetic wave propagation in a medium based on the FDTD method. Some were developed by companies as commercial products (Lumerical, EEsof - FDTD element) while others were originally designed as open-source tools (openEMS, WOLFSIM). In current research, the RSoft FullWAVE **[90]** is widely used for field computations in nano-antenna geometry (Chapter 5) and a multilayer metal-dielectric slot waveguide (Chapter 6).

FullWAVE is a typical computer-aided design (CAD) environment developed for operating at micrometric wavelengths (0.2 μm ≤ λ ≤ 6 μm). It allows high flexibility for studying arbitrary geometries, controlling numerical meshes, and adjusting source parameters and boundary conditions according to problem requirements. The software supports both graphical user interface (GUI) and command line operations, and can run user-defined scripts written in Perl, Python, C or C++.

FullWAVE is normally used to study passive photonic structures, i.e., structures with no explicit gain regions (i.e., quantum dots, quantum wells or any other active media). The modelled geometries include waveguides, nano-antennas, photonic crystals, ring resonators, metamaterials and other plasmonic devices. The software has large amounts of inbuilt dispersive materials, which allow users to operate in a wide range of frequencies. The incorporated dispersion model determines electric permittivity as **[90]**:

$$\varepsilon(\omega_{Fullwave}) = 1 + \sum_{k}^{6} \frac{\Delta\varepsilon_k}{-a_k(\omega_{Fullwave})^2 - b_k(i\omega_{Fullwave}) + c_k} , \tag{3.13}$$

where $\omega_{FullWAVE}$ denotes the FullWAVE's computational frequency (which is the angular frequency normalized on the speed of light in a vacuum: $\omega_{FullWAVE} = \omega_0 / c_{vac}$;

$c_{vac} = 3\times10^{14}$ μm/s) and a, b, c and $\Delta\varepsilon$ are the numerical coefficients from the software's material library (their exact values are given in respective chapters).

FullWAVE uses micrometres as standard units of length, with time also expressed in microns (i.e., its units are given as $c_{vac}T$). In all simulations, the boundaries are set as perfectly matching layers (PML), which results in a complete absorption of the electromagnetic radiation crossing them. From a physics point of view, this means that the wave freely leaves the simulation area and then propagates to infinity without being reflected back.

The spatial grid can be set to both uniform and non-uniform regimes. The first is used to simulate dielectrics and the second is utilized to either model fine features or when metal is involved. Usually, the spacing resolution should be at least several times smaller than the tiniest presented feature. Typical mesh sizes for a device with dimensions of approximately 1 micrometre are $\Delta x = \Delta y = \Delta z = 20$ nm for dielectric and $\Delta x = \Delta y = \Delta z = 3$ nm for metallic regions. The temporal grid is defined by the Courant number **[89]** and FullWAVE uses the following stability criterion **[90]**:

$$c_{vac}\Delta t < \frac{1}{\sqrt{1/\Delta x^2 + 1/\Delta y^2 + 1/\Delta z^2}} \, . \tag{3.14}$$

It should be mentioned that, in particular situations, even satisfying the Courant criterion does not prevent the simulation diverging (this could be attributed to the possible accumulation of round-off errors in FDTD calculations). However, the significant improvements obtained in both spatial and time resolutions normally solve this problem.

The radiation source in simulations can operate in two regimes. The CW regime is used to calculate the electric or magnetic field magnitude at a particular point or find the average power transmitted through the selected area. The pulsed regime is utilized to calculate the Q-factor for a set of wavelengths, for example, when modelling an operation of a micro-laser.

During numerical calculations, field distributions are usually visualized as coloured images and can be selected at any point inside the simulation area. The values of the fields are normalized on the source values, with the colour bar ranging from -1 to 1. The exact magnitudes of the wave components can be recorded at any space point by inserting a so-called field monitor there. Depending on the selected regime, it records and averages over time either the field in the middle of the monitor, or the total amount of power transmitted through the monitor area. The output data is saved as an ASCII text file, which allows further processing, for example, using MATLAB. Typically, this information is a simple 2D table with the first column representing time and others corresponding to the field (or power) values recorded by the respective monitors.

3.2.5 MATLAB

Data processing is performed with the help of MATLAB, which is a high-level programming language developed by MathWorks **[91]**. It is quite popular among researchers due to its simple interface, large library of prescribed functions and wide range of possible applications, including image and video recognition, signal processing and numerical analysis. In the present research, MATLAB is used for:

1) Generating and visualizing patterns for AutoScript (Section 4.4.2);
2) Extracting the effective refractive index of the metamaterial (Section 7.3.2);
3) Plotting most of the figures and field distributions.

3.2.6 Thermal modelling with COMSOL

Temperature distributions are calculated using a Heat Transfer module of COMSOL Multiphysics software **[92]**. This numerical package based on finite element method (FEM) has the design capabilities similar to that of RSoft FullWAVE, which includes creating arbitrary geometries, adjusting the boundaries (i.e., thermally conducting or insulating), selecting the primary heat transfer mechanisms (conduction, convection or radiation) and controlling nonlinear effects. The heat source could be selected as either having given temperature or given heat flux enabling estimation of the absorbed power using Eq. 2.48. The modelling is not limited only to heat transfer in solids, gas or flowing liquids, but also includes bio-heating and allows to study complex designs by incorporating effects from different COMSOL numerical packages (AC/DC, Acoustics, Corrosion, Fatigue, and others).

However, it should be noted that the thermal distributions presented in the following chapters should be treated rather qualitative than quantitative. This occurs for two reasons:

1) Despite having a large inbuilt material library, the provided thermal characteristics are mostly given for bulk materials and do not take into account the materials' fabrication methodology or surface morphology (which is especially important for nano-scale plasmonic structures) **[93, 94]**.
2) The lasers, utilized in the experiments, are operating close to their stability limit meaning that the peak power may change with time. These power variations affect the heat flux density and, consequently, the temperature of the considered nano-structures. Thus, the laser parameters used in simulations represent an ideal situation corresponding to some averaged values, which may significantly differ from the instant values obtained during exposure.

In spite of these shortcomings, the calculated thermal profiles provide a general idea of heat distribution inside plasmonic devices and correspond to thermal plots found in literature **[85, 95]**.

3.3 Summary

The numerical methods discussed here play a crucial role in a theoretical modelling of plasmonic devices in Chapters 5-7. Without robust FDTD algorithm it would be nearly impossible to calculate the field distributions in complex media, and draw any conclusions on the wave propagation character. Additionally, the studies on light-matter interactions can't be complete without a discussion on thermal modelling, which provides a qualitative insight on temperature profiles inside plasmonic devices.

While calculation algorithms are important for theoretical modelling in developing and optimizing the designs of nano-structures, they represent an ideal situation and, thereby, the numerical results may differ from that obtained in experiment. However, before moving to experimental data, it is worth of describing the fabrication facilities and patterning methodologies used to produce the plasmonic nano-devices as is outlined in the next chapter.

Chapter 4 – Fabrication equipment and methodologies

4.1 Introduction

Chapter 4 describes the main operating principles of the Electron Beam Evaporator (EBE), Sputter and Focused Ion Beam (FIB) systems. The first two are used for material nano-deposition and the last – for surface milling. The present chapter also addresses the sample preparation as well as some FIB fabrication issues, which include using scripting language and material re-deposition.

While some of the above topics are briefly mentioned in later chapters, this is done purely for reference purposes, since detailed descriptions of the utilized equipment are given in the following sections.

4.2 Nano-fabrication setups

4.2.1 EBE/Thermal evaporator

Fig. 4.1 – EBE/Thermal evaporator

EBE/thermal evaporator (Fig. 4.1) is used to deposit metallic films with the thickness typically ranging from several to hundreds of nanometres. These coatings are then routinely utilized in the lift-off process **[96]** or are patterned by the FIB. The deposited films are formed from the source material, which is heated to boiling temperature (or directly sublimated) and then condensed on the sample surface. Any arbitrary solid surface can be metalized in this fashion providing the deposited material doesn't chemically interact with its substrate.

In the experiments, all depositions are performed using the Temescal BJD-2000 E-beam/thermal evaporator system (BJD-2000), which allows utilization of up to 6 different materials within one fabrication cycle **[97]**. A deposition starts with loading the crucibles with source metals (Al, Au, Cr, Ge, Ni, Pt or Ti) and mounting the samples (usually quartz or GaAs substrates) on one of the five 6" wafers. Then, the system is pumped by scroll and cryo pumps to a 5×10^{-6} Bar pressure. The selected crucible is intensively heated by the electron gun and the metal inside it starts melting, creating a flow of evaporated atoms towards the mounted sample. The wafers spin at a speed of 25 rotations per minute, which makes the film deposition more uniform, with the deposition rates varying from 1 to 2 Å per second depending on the desired final thickness. A sufficient distance between the crucible and wafers helps to avoid excessive heating during the metallization required for lift-off processes **[97]**.

BJD-2000 is also capable of providing a thermal evaporation regime, whereby the evaporation source is not a crucible with the selected material but a metallic wire, which is heated via a current supplied by the system. However, this method is not used in the described fabrications as all depositions are made only via e-beam evaporation.

It should be also mentioned that due to its lattice constant mismatch, gold does not stick very well to a quartz substrate **[98]**, thus, an additional thin titanium adhesion layer is used in all devices containing gold. While this layer is of the order of several nanometres, it still affects a micro-device's performance **[99]**, which is also taken into account in numerical simulations.

4.2.2 Sputter system

Fig. 4.2 – Sputter system

The Sputter system presented in Fig. 4.2 is another device commonly used for thin film depositions. During this process, material atoms are expelled from a solid target bombarded by a particle source. The interaction between the target's surface and bombarding particles exhibits a collision cascade character: if the incoming particles have higher energy levels than the target atoms' binding energy, these atoms will likely gain sufficient momentum to leave the surface, i.e., will be sputtered. Then, they will be re-deposited on the internal surface of the chamber, including that of the prepared sample. The amount of sputtered atoms per single bombarding particle (sputter yield) depends on different aspects, such as the incident angle, original bombardment energy and target's binding energy. The bombarding particles can be produced by plasma, an ion source, an accelerator or even radioactive material.

Film depositions are performed with the help of an ATC 2000 UHV **[100]**, which uses DC or microwave sputtering, and the setup has six available guns, with the maximum wafer size of 100 mm. A wide range of materials available for deposition include Au, Co, Cu, Er, Fe, Ge, ITO, Mo, Nb, Ni, Pd, Pt, SiO2, SnO_2, Si_3N_4, TeO_2, Al_2O_3 and TiO_2. The ATC 2000 UHV can be adjusted for confocal, direct and off-axis operations, which determines the mutual orientation of the source and sample. Although the advantages of particular settings depend greatly on the desired application, typically, direct deposition is the fastest, while confocal provides the best film uniformity **[100]**.

In the present research, the sputter system is used only for TiO_2 deposition in confocal geometry. It takes about 33 minutes to deposit 50 nm of material, which is a rate of 0.25 Å/sec.

4.2.3 FIB system

Fig. 4.3 – FIB system

The FIB system shown in Fig. 4.3 is a type of multi-purpose research and industrial equipment used for surface analysis, milling and deposition of materials. It is similar to the scanning electron microscope (SEM) in the sense that it also uses a beam of charged particles, but, instead of electrons, FIB operates with ions (primary Ga+). Due to the heavier mass of Ga+ ions (114000 of electron mass), they have less velocity than electrons accelerated with the same voltage. Also, as they are significantly larger, ions only interact with the outer shells of the scanned material, and not with the atomic nuclei. However, the FIB system should not been mistaken for direct-write lithography, which also utilizes a focused flow of charged particles (for example, proton beam writing **[101, 102]**), since these setups use different operational mechanisms.

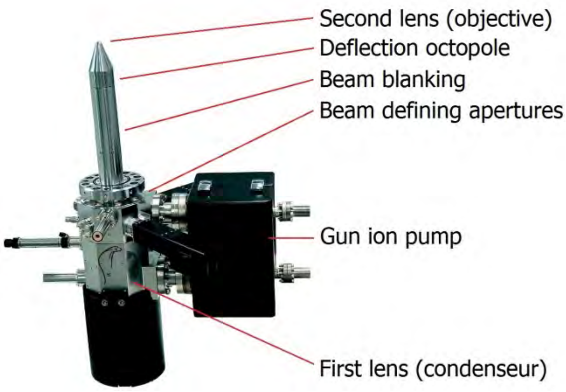

Fig. 4.4 – FIB column

In FIB system, the ion source is incorporated in the ion beam's column (Fig. 4.4) and operates by gallium being placed close to the tungsten needle and then heated until it wets the metal. Then the melted material flows to the needle's tip, where it forms a micro-cone. Due to the high electric field applied to the needle's end, the gallium is ionized and emitted from the cone in the direction of the sample. The electrostatic lens focuses gallium particles into a beam and a set of different apertures helps to determine its spot size **[103]**. After collision with the sample, gallium effectively mills a nano-hole by removing some of the material from the target's surface. The acceleration voltage determines the momentum of Ga+ ions: small values result in exact patterning, but require longer exposures in order to achieve the desired depth, while higher voltages lead to faster, but less accurate outcomes. However, in both cases, precision remains at the submicron scale providing the system is correctly focused **[104]**.

All millings described further are conducted using the FEI Helios 600 NanoLab FIB system **[105]**. It incorporates a 30 kV e-beam SEM capable of resolutions up to 0.9 nm and can perform all standard tasks, such as simple milling, 3D reconstruction (slicing and SEM) and transmission electron microscopy (TEM) lamellae preparation (also available in the automatic mode). In addition, this setup is able to deposit Au, Pt and SiO_2, and perform an etching with XeF_2 (for SiO_2) or I_2 (for III-V group material) gases **[97]**.

During fabrication, the sample is placed on the sample stage inside the FIB chamber, which is then pumped to a vacuum (10^{-3} Pa), and after this the ion and electron beams can be activated. The flexible sample stage allows the following degrees of freedom:

1) ±20 cm in the horizontal *x*-*y* plane;
2) 0-10 mm in the vertical *z*-direction;
3) 0-360° rotation in the *x*-*y* plane;
4) 0-90° tilting of the *x*-*y* plane with respect to the vertical *z*-axis.

For standard 2D milling, the work distance is 4 mm from the ion source and the tilt angle is 52°. The milling current varies between 9.7 pA and 21 nA depending on the scale of the pattern, but, typically, is set to 28 pA for the fabrication of most near-infrared devices. While specific details regarding the pattern geometries are given in respective chapters, the generic milling and most common troubleshooting approaches are described in the next section.

4.3 Fabrication methodologies

4.3.1 Sample preparation

Sample preparation starts by cutting a small piece of the required size and shape from a larger sample lamina using a diamond cutting tool, carefully cleaning it with acetone and isopropanol (IPA), and manually removing any visible grease and dust using a wet cotton swab. Then, the sample is placed in an ultrasonic bath for several minutes for further cleaning and, finally, is dried by an air gun, which typically uses compressed nitrogen gas. To keep the samples clean, they are handled only while wearing latex gloves and are stored in a closed sample box. Immediately before material deposition or surface milling, the samples are cleaned again by the air gun to eliminate any possible dust.

4.3.2 Patterning with FIB

As previously mentioned, the primary task of the FIB system is milling arbitrary 2D patterns on the prepared sample surfaces. From a software point of view, this could be achieved in two ways:

1) Directly drawing the pattern in a CAD type of environment;
2) Using AutoScript and AutoFIB to create and manage the script, which controls the Ga+ ion source.

The first approach is quite simple and perfectly suits to small patterns, such as a single dipole nano-antenna or a set of gratings. However, with an increase in the number of elements, their mutual alignment becomes more complicated. For extremely complex patterns, such as that consisting of several non-periodic blocks or more than 50 elements, this approach is no longer viable and one should use the second method.

AutoScript is a Basic-like programming language capable of performing simple operations, such as introducing loops and using condition operators. A user can utilize AutoScript to define the structure's geometry, depth of milling, ion source current, position of the sample stage and other important patterning settings **[106]**. During fabrication, the prepared script is automatically executed by the AutoFIB environment **[107]** and requires no further actions by the user. A detailed description of a simple patterning code is presented in Appendix A, and advanced patterning methods and some complex micro-scale structures are discussed in Appendix B.

As would be expected, the focusing issue is very important during FIB milling. Since the micro-controller operating the ion source uses the distance between the source and sample surface as the crucial input information, poor focusing can result in patterns milled with incorrect dimensions (especially, when there is a problem with stigmation, i.e., beam stretching in either horizontal direction). This leads to scaling inaccuracies in the desired geometry that could be as large as nearly double for nano-size patterns and often become different in the *x*- and *y*-directions, thereby causing even more confusion. Improving focusing using an ion beam may be very challenging because its gallium atoms inevitably damage a sample surface. This makes it nearly impossible to obtain the surface's fine features at large magnifications, since they gradually decay with each subsequent scan. Such problem could be overcome by first patterning a dummy rectangular and then calculating the scaling coefficients to modify the desired pattern later.

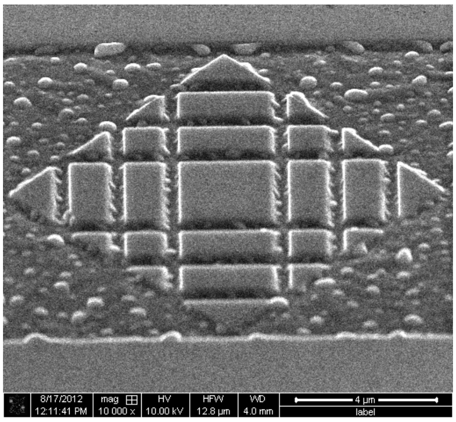
Fig. 4.5a – Material re-deposition

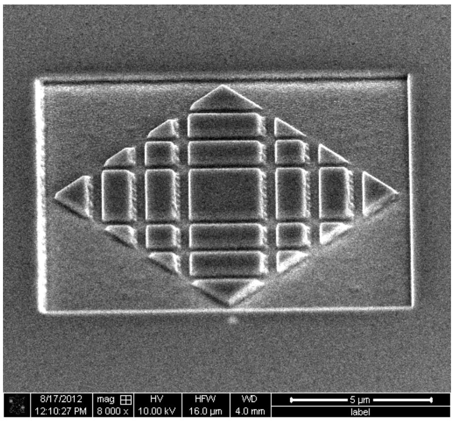
Fig. 4.5b – Patterning with activated gas needle

Finally, there is always an issue with gallium implantation and material re-deposition **[109, 110]**, when Ga+ ions are not scattered away, but, instead, form agglomerations on the sample surface, as clearly observed around the patterned area in Fig 4.5a. This can happen during long exposures or for narrow and deep patterns, when the gallium becomes trapped inside the milled hole. Any subsequent milling of such a region results in only replacing re-deposited Ga+ ions with a new portion of sputtered material. This situation greatly reduces the removing rate, but, fortunately, it can be solved by injecting a gas needle. A flow of XeF_2 for SiO_2 substrates and I_2 for III-V group compounds effectively prevents Ga+ ions from re-deposition (Fig. 4.5b). It should be noted that small currents also reduce re-deposition and, furthermore, improve the quality of the sidewalls during milling **[110]**.

4.4 Summary

The present chapter fully describes the fabrication facilities (EBE, Sputter system and FIB system) utilized during the candidature. This research equipment is used for precise nano-scale patterning of plasmonic devices, which are discussed in Chapter 5 and Chapter 7. Additionally, the issues on FIB milling are briefly outlined, while the samples of scripting code can be found further in Appendices A and B.

Chapter 5 – Titanium nano-antenna for high-power pulsed operation

5.1 Introduction

Plasmonic nano-antennas are generally used to produce intense electric fields in a very small area and are typically driven by external light sources. In a case of a Q-switched laser, the strong incident electric fields become further enhanced reaching very high values, and the heat, generated from plasmonic excitation and material absorption, may thermally damage these delicate nano-structures, thereby limiting their operational fluence range.

In order to increase the maximum peak power, which these devices can withstand, they can be fabricated from a durable material such as titanium instead of fragile gold. While this slightly reduces the field enhancement capabilities of nano-antennas, it greatly improves their overall heat resistivity, which enables exposure to larger incident fluences and, thus, boosts the structure's capacity to produce even higher electric fields.

This chapter begins the study of high-power plasmonic devices by first comparing the performances of dipole nano-antennas, one made from gold and another from titanium. For this comparison, the structures' field enhancement factors are calculated as a function of the gap width. Then, the electric field and temperature distributions are analyzed based on the numerical methods discussed in Chapter 3. Finally, the nano-antennas are fabricated and exposed to a 1053 nm Q-switched laser in order to determine their melting threshold fluence values and, thereby, find the maximum magnitudes of the incident electric fields that these structures can withstand.

It is shown that titanium-based nano-antennas can handle a more than 18 dB greater power density than their gold counterparts, which makes them useful in different high-power applications, including SERS and nano-imaging. The studies of nano-antennas outlined in this chapter are also published in **[111]** and were presented at *OSA Advanced Photonics 2013* (Rio Grande, Puerto Rico, USA) **[112]**.

5.2 General introduction to nano-antennas

The advent of plasmonic nano-antennas has brought a new era into the nano-world whereby freely propagating light can be converted into localized optical fields and vice versa **[113]**. These structures can confine an incident wave well below its diffraction limit **[114]** and generate highly intense electric fields that can be used in a multitude of applications, such as nonlinear optics, imaging, sensing and photovoltaics **[113]**.

The simplest nano-antenna device is a dipole antenna **[114**, **115]**, which is constructed by separating two metallic regions with a dielectric gap. The excitation of such a structure by a light source may result in a strong electric field enhancement of more than 50 times. Besides dipole antennas, more complex designs have also been studied, such as Yagi-Uda **[116, 117]**, spiral **[118-120]**, phased-array **[121]**, bow-tie **[75, 115, 122]**, staircase **[123]** and Charnia-like **[81]** nano-antennas, which either provide better directivity or operate over larger bandwidths.

Although most nano-antennas are made from metal, dielectric and semi-conductor devices have also been demonstrated recently **[124-126]**. Nano-antennas can be grouped in the following categories depending on their properties.

1) Directional nano-antennas are small replicas of radio-frequency Yagi-Uda antennas. They possess the properties of their larger counterparts **[127, 128]** and also consist of a reflector, feed and several directors. The incident light becomes coupled to the feed and the directors guide the optical radiation forward, while the reflector prevents it from traveling back.

2) Broadband nano-antennas are utilized in applications that are required to operate over a wide range of wavelengths. Typical examples are solar cell devices, in which antennas are used to improve conversion of the sun’s energy over the broad spectrum of the incident light **[129-131]**.

3) Plasmonic nano-antennas are a type of integrated devices, which can be excited by a tiny external light source, such as a quantum cascade laser **[132, 133]** or polygonal micro-laser **[44]**. These nano-antennas help to characterize an excitation signal or are used to trap nano-particles.

4) Sensing nano-antennas are used in applications, such as SERS, since they provide strong field localization and high field enhancement, which are crucial for detecting separate molecules and chemical compounds **[134-136]**.

Nano-antennas can be fabricated using different types of equipment, such as electron beam lithography (EBL) followed by a lift-off process, FIB milling **[123]** and nano-stencil lithography **[137]**. Regardless of the technique chosen, gold is generally deposited on top of a thin titanium film **[99]** to provide better adhesion between the gold layer and substrate. However, as mentioned by Lahiri and co-workers **[99]**, the presence of titanium changes the performance of a plasmonic device and results in the shifting of its resonant frequency, which is caused by different material properties, i.e., increased absorption and modification of the plasma frequency.

5.3 Theoretical analysis of dipole nano-antenna

5.3.1 Nano-antenna design

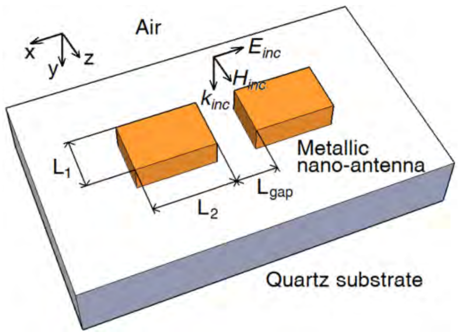

Fig. 5.1 – Schematic of nano-antenna structure

The considered dipole nano-antenna is shown in Fig. 5.1. It consists of two metallic regions (orange areas in Fig. 5.1) placed on top of a quartz substrate and separated by an air gap. The metallic material is either gold (with a very thin 2 nm titanium adhesion layer) or titanium and has a metallization thickness of 300 nm and length $L_1 = 100$ nm. The studied structures have air gap widths L_{gap} ranging from 30 to 120 nm and the width of each metallic region L_2 (the nano-antenna arms have equal dimensions) is such that $2L_2 + L_{gap} = 425$ nm.

The optical properties of the nano-antenna are numerically analyzed using the commercial FDTD software FullWAVE **[90]** discussed in Chapter 3. The light is modelled as incident normal to the nano-antenna, with the orientation of a wave vector k_{inc} parallel to the y-axis and the main electric field component E_{inc} directed across the air gap (x-axis), as shown in Fig. 5.1. The computational region is terminated by PMLs.

The grid is non-uniform, being refined at the boundaries between the metal and dielectric. The mesh sizes for the dielectric and metallic regions are $\Delta x = \Delta y = \Delta z = 20$ nm and $\Delta x = \Delta y = \Delta z = 3$ nm respectively. Although insulator grid sizes for cases of narrower gaps have been reduced to $\Delta y = \Delta z = 20$ nm and $\Delta x = 5$ nm, the results showed only a 1% variation from those for coarser meshes. To satisfy the CFL condition, the time step is chosen to be 8×10^{-18} s, which corresponds to less than half of the stabilization limit determined by FullWAVE.

The dispersive model for metals is defined by Eq. 3.13 in Chapter 3 as:

$$\varepsilon(\omega_{Fullwave}) = 1 + \sum_{k}^{6} \frac{\Delta\varepsilon_k}{-a_k(\omega_{Fullwave})^2 - b_k(i\omega_{Fullwave}) + c_k},$$

and the numerical coefficients for titanium and gold are given in Table 5.1 below.

Table 5.1 – Dispersion coefficients from FullWAVE material database **[90]**

Titanium				Gold			
Δε	a	b	c	Δε	a	b	c
201.7403	1	0.41529	0	1589.516	1	0.268419	0
1225.436	1	11.52684	15.48524	50.19525	1	1.220548	4.417455
535.7023	1	12.75245	61.22558	20.91469	1	1.747258	17.66982
254.9016	1	8.42229	161.4646	148.4943	1	4.406129	226.0978
1.36311	1	8.923677	9683.258	1256.973	1	12.63	475.1387
0	0	0	0	9169	1	11.21284	4550.765

In this simulation, the incident wave is considered to be plane, which is a good approximation because the actual spot diameter of the source is much larger than the computational area (the latter is 10 μm by 10 μm, while the laser beam is several millimetres in diameter). When the structure is aligned to the position of the maximum peak power, the magnitude of the incident electric field $|E_{inc,\,peak}|$ can be estimated as:

$$|\boldsymbol{E}_{inc,peak}| \cong \sqrt{\frac{8Z_{air}P_{peak}}{\pi\varphi_{spot}^2}}, \tag{5.1}$$

where Z_{air} is the intrinsic impedance of air (~ 377 Ω), P_{peak} is the peak power of the wave (its value can be controlled by an attenuator in experiments) and φ_{spot} is the spot diameter of the pulse, which is defined by containing 95% of the total incident power. For example, the peak power of $P_{peak} = 15$ μW, spot diameter of 1 cm and total attenuation of 0.4 dB (1.097 times) result in $|E_{inc,\,peak}| = 11.5$ V/m.

5.3.2 Electric field enhancement in nano-antennas

The space between the metallic regions in a nano-antenna generates a higher electric field than incident field due to the excitation of a plasmonic wave. The relationship between the magnitudes of the electric fields is the field enhancement factor F_{gap}, which is given by:

$$F_{gap} = \frac{|\boldsymbol{E}_{gap,peak}|}{|\boldsymbol{E}_{inc,peak}|}, \tag{5.2}$$

where $|E_{gap,peak}|$ is the magnitude of the electric field measured in the middle of a nano-antenna gap. The obtained electric field enhancement can be quite high and makes these structures attractive in a variety of applications, including nano-imaging, detection of nano-particles, sensing and harnessing nonlinear effects. For example, in SERS devices, the enhancement factor is proportional to the fourth power, i.e., F_{gap}^4, which offers huge potential for using nano-antennas there **[123]**.

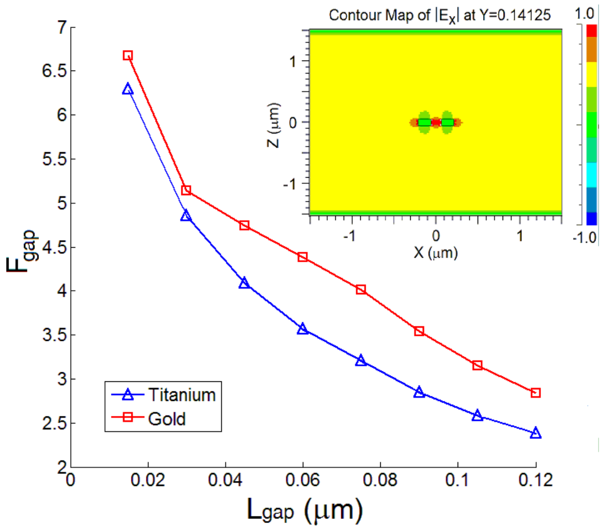

Fig. 5.2 – Electric field enhancement factors as a function of gap width. Inset – electric field strength profile for L_{gap} = 120 nm

Based on FDTD simulations, the electric field enhancement factor as a function of the gap width is plotted for both the gold and titanium nano-antennas in Fig. 5.2 at a wavelength of 1053 nm. This factor changes very little with the spot size of the source given that it is much larger than the area occupied by nano-antennas. It can be seen that, on average, the field enhancement factor for gold is about 19% higher than that for titanium mainly because the latter has larger absorption losses. The inset demonstrates the E_x-field strength profile in the *x*-*z* plane for a gap width of 120 nm. The values of the field enhancement factors for both materials are presented in Table 5.2.

Table 5.2 – Electric field enhancement factors as a function of gap width

L_{gap}, nm	F_{gap} (gold)	F_{gap} (titanium)
120	2.84	2.39
105	3.15	2.59
90	3.54	2.85
75	4.01	3.21
60	4.39	3.56
45	4.74	4.09
30	5.14	4.86
15	6.67	6.29

It should be noted that the electric field strength can be higher at the edges of a nano-antenna (i.e., on the interface between the metal and air gap). For example, a gold nano-antenna with a gap width of 60 nm has F_{gap} in the middle equal to 4.39, while the field enhancement at the side walls can reach values as high as 7.3. However, the higher electric fields at the edges are not achieved in practice because of fabrication imperfections, which inevitably make the side walls tilt angle smooth rather than abrupt.

To obtain a more precise comparison of gap widths, the total length of a nano-antenna should be optimized to produce the highest field enhancement. The optimization process (for gold and titanium) is conducted for two gaps – 60 nm and 120 nm – which results in a field enhancement change of less than 6%. Therefore, in the experiments, it is decided to vary only the gap width, while keeping the total length of the nano-antennas constant.

5.3.3 Electric field distributions in nano-antennas

In order to obtain sufficient data on E_x-field distribution from the simulations, an extensive number of electric field monitors (marked in red in Fig. 5.3) is placed in the region surrounding the nano-antenna. The values in the intermediate spatial points (marked in grey in Fig. 5.3) are approximated using cubic Hermit splines and the recorded $|E_x|$ values are then normalized with respect to the magnitude of the incident electric field. Note that the electric field does not penetrate the metallic parts of nano-antenna outlined by black lines in Fig. 5.3. Thereby, no monitors are placed there.

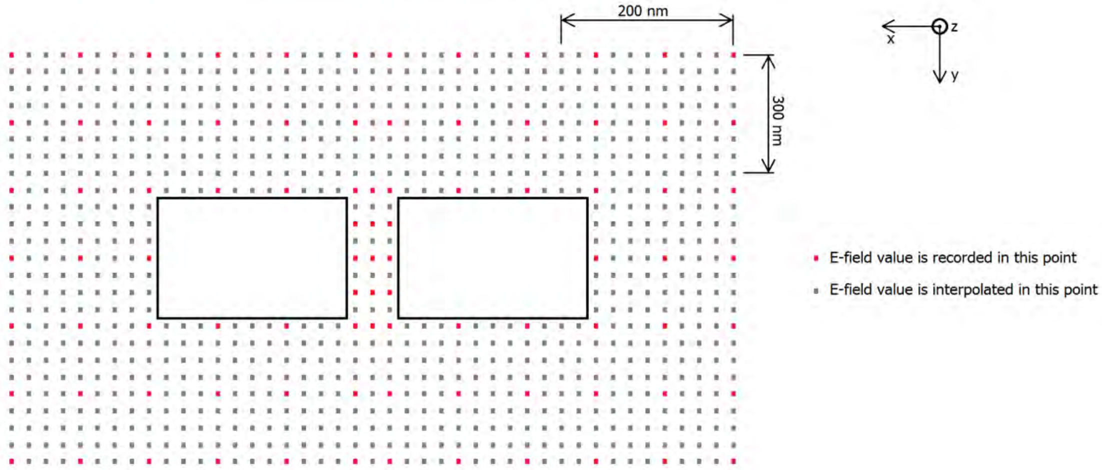

Fig. 5.3 – Spatial positions of points for recorded (red) and interpolated (grey) electric field values in nano-antenna with 60 nm gap width

2D plots of the normalized electric field profiles for the gold and titanium nano-antennas with 60 nm gap width are presented in Figs. 5.4a-d. Fig. 5.4a and Fig. 5.4b show the field distributions along the *x-y* plane (z = 0 nm, a slice taken in the middle of the gap) and Fig. 5.4c and Fig. 5.4d demonstrate those along the *x-z* plane (y = 150 nm, a slice taken at the half-height of the structure) for the gold and titanium nano-antennas respectively.

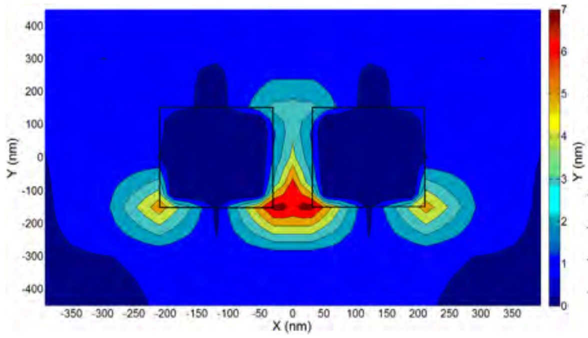

Fig. 5.4a – Normalized electric field strength (*x-y* plane) for gold nano-antenna with 60 nm gap width

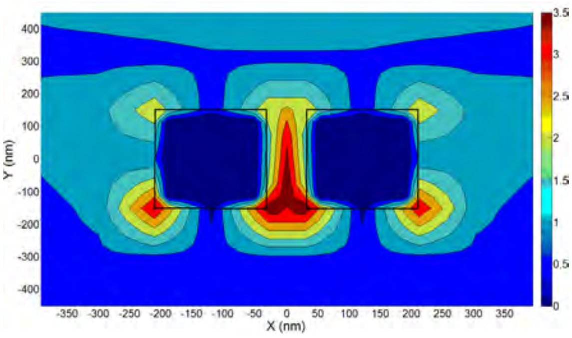

Fig. 5.4b – Normalized electric field strength (*x-y* plane) for titanium nano-antenna with 60 nm gap width

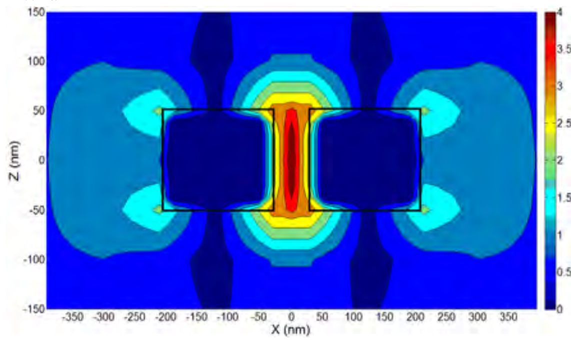

Fig. 5.4c – Normalized electric field strength (*x-z* plane) for gold nano-antenna with 60 nm gap width

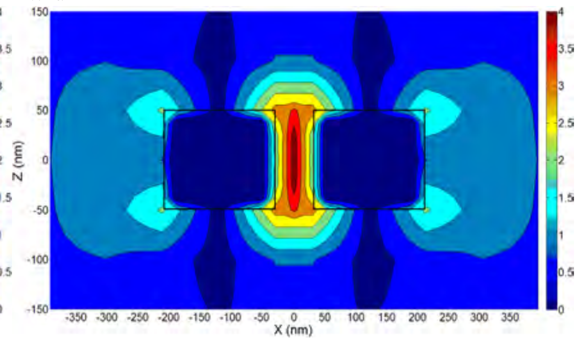

Fig. 5.4d – Normalized electric field strength (*x-z* plane) for titanium nano-antenna with 60 nm gap width

Figs. 5.5a-5.6d show the normalized $|E_x|$ distributions as 3D wire-frame plots (note that the vertical axis in each plot always represents the normalized electric field strength not the spatial coordinate). As can be seen from these figures, for both metals, the wider gap of 120 nm has a smaller $|E_x|$ component than the 60 nm gap counterpart. While the *x*-*y* cross-sections of the gold nano-antenna have significantly higher magnitudes of the electric field than those of the titanium device (Figs. 5.5a-d), in the *x*-*z* plane, the results for both structures are very close (Figs. 5.6a-d). The simulations for other gap width demonstrate similar field distributions for the considered materials with the highest field values localized inside the gaps and close to the nano-antennas' corners.

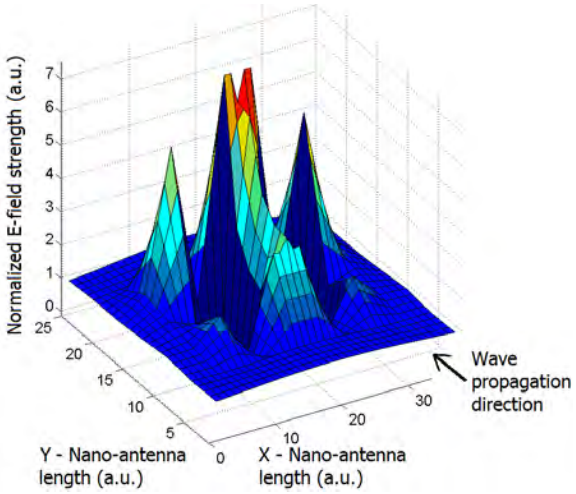

Fig. 5.5a – Normalized electric field strength (*x-y* plane) for gold nano-antenna with 60 nm gap width

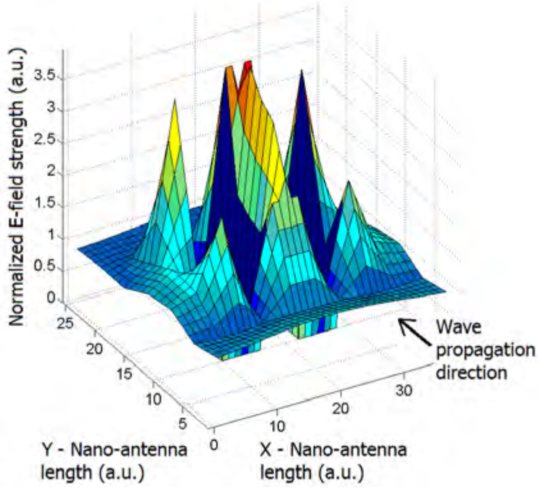

Fig. 5.5b – Normalized electric field strength (*x-y* plane) for titanium nano-antenna with 60 nm gap width

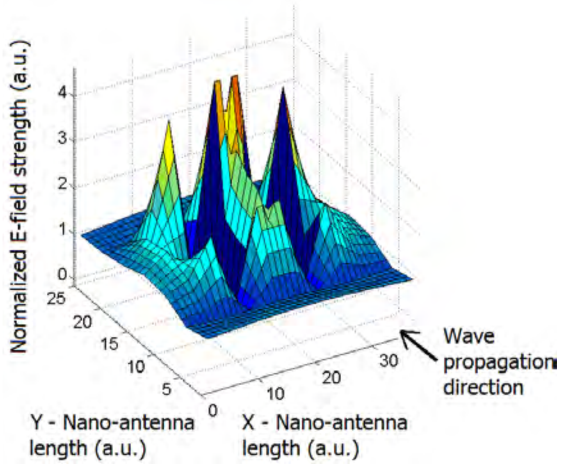

Fig. 5.5c –Normalized electric field strength (*x-y* plane) for gold nano-antenna with 120 nm gap width

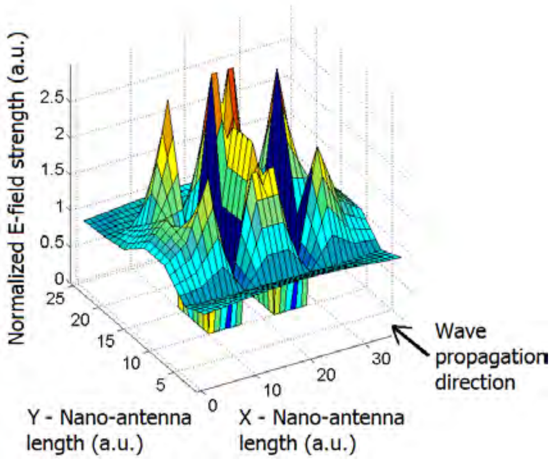

Fig. 5.5d – Normalized electric field strength (*x-y* plane) for titanium nano-antenna with 120 nm gap width

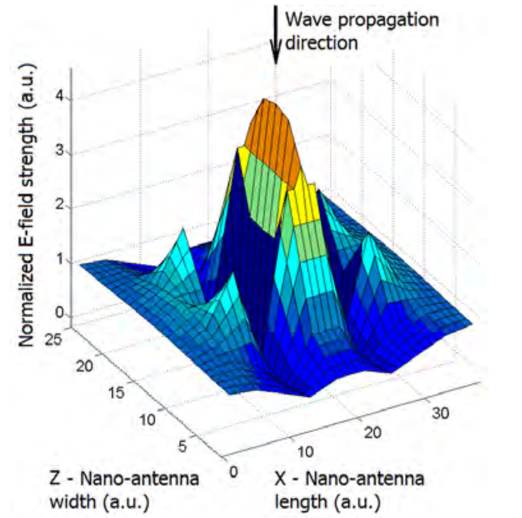

Fig. 5.6a – Normalized electric field strength (*x-z* plane) for gold nano-antenna with 60 nm gap width

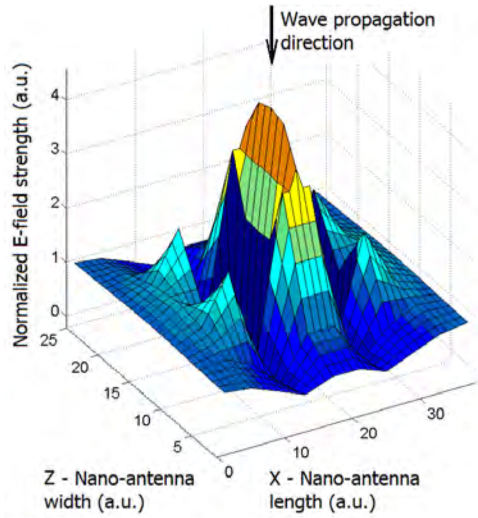

Fig. 5.6b –Normalized electric field strength (*x-z* plane) for titanium nano-antenna with 60 nm gap width

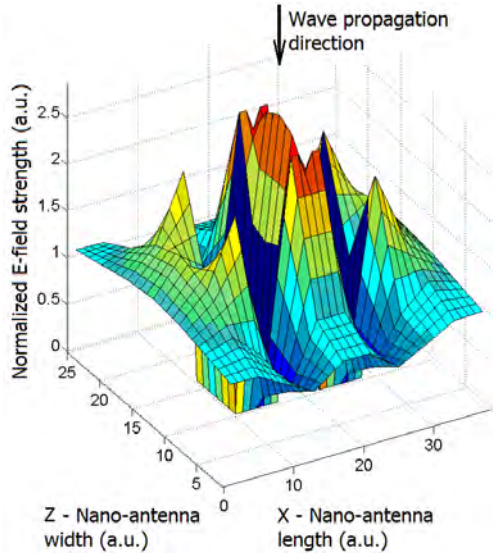

Fig. 5.6c – Normalized electric field strength (*x-z* plane) for gold nano-antenna with 120 nm gap width

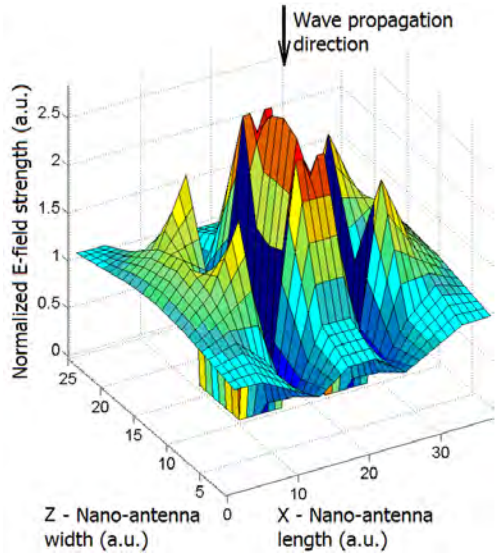

Fig. 5.6d – Normalized electric field strength (*x-z* plane) for titanium nano-antenna with 120 nm gap width

It can be also observed that the electric field is larger at the edges of a nano-antenna, but only over a very limited region. More importantly, the electric field distribution is more uniform in the titanium nano-antenna, which provides a lower power density than the gold one. This result can partially explain why the titanium-based nano-antennas are capable of handling more power than their gold counterparts.

In the experiments, a 2 nm thick titanium film is deposited as the adhesion layer prior to gold deposition. In order to study the impact of this film on the electric field enhancement of the nano-antenna, the thickness of the titanium/gold bi-layer is varied from 0 to 300 nm, with the total height fixed at 300 nm. The results are presented in Fig. 5.7 for 120 nm (○ – magenta) and 60 nm (□ – blue) gap widths. The maximum value of F_{gap} is reached when the thickness of the titanium in the nano-antenna becomes 50% resulting in an increase in F_{gap} of about 15% over its value for pure gold structure. This can be partially explained by the stronger field localization close to the interface between the gold and titanium, as shown in the inset in Fig. 5.7.

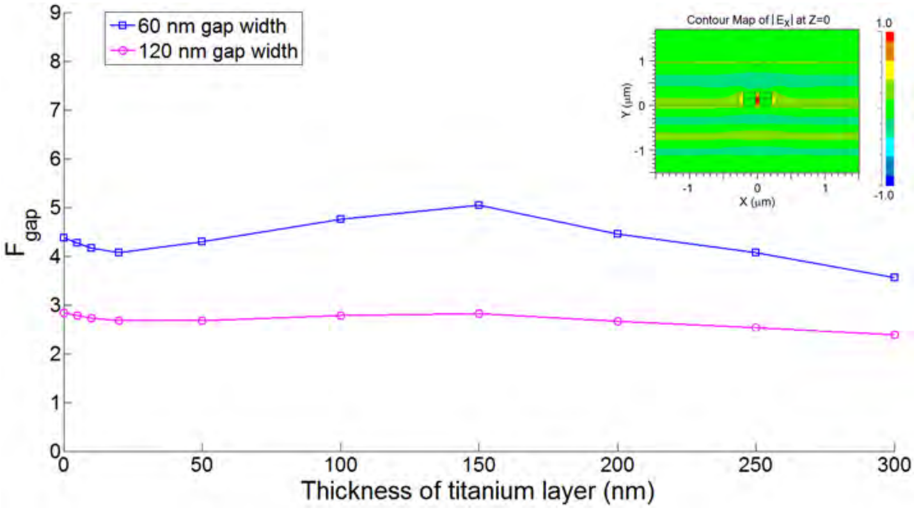

Fig. 5.7 – *E*-field enhancement for different thicknesses of titanium. Inset – *E*-field profile in *x-y* plane for 50% titanium ratio

5.3.4 Laser-material interactions

The physical parameter generally associated with laser damage of a material is fluence **[19]**. In the case of a Q-switched laser, the single pulse energy W_s and fluence F_s are calculated as:

$$W_s = \int_{t_1}^{t_2} P(t)dt = P_{peak}\tau_{eff} \tag{5.3}$$

$$F_s = W_s \frac{4}{\pi\varphi_{spot}^2}, \tag{5.4}$$

where $P(t)$ is the envelope of the power as a function of time, t_1 and t_2 are the arbitrary instants when the pulse power is not negligible ($t_1 < t < t_2$) and τ_{eff} is the effective duration of the pulse. In a given exposure interval T_{ref} and repetition rate f_{rep}, the number of pulses in that time period N_{pulse} is $N_{pulse} = T_{ref} \cdot f_{rep}$. Then, the exposure F_{ex} and effective F_{eff} fluences can be found as:

$$F_{ex} = N_{pulse} W_s \frac{4}{\pi\varphi_{spot}^2} \tag{5.5}$$

$$F_{eff} = N_{pulse}^{p} W_s \frac{4}{\pi\varphi_{spot}^2}. \tag{5.6}$$

Calculations of the effective pulse energy during a fixed exposure time follow the procedures provided in the Australian/New Zealand laser safety standards **[18]**. Parameter *p* is a variable with values between 0 and 1, which takes into account the fact that the structures can cool in the interval between two consecutive pulses. If, during this time, the devices return to the ambient temperature, $p = 0$ and the effect of each pulse on a nano-antenna will be independent. On the other hand, if thermal effects are very slow, exposure to successive pulses will have a cumulative effect and $p = 1$. An example of an intermediate situation ($0 < p < 1$) is the human eye, for which $p = 0.25$ **[18]** at low repetition rates (f_{rep} below 10 kHz).

Both Chang *et al.* **[138]** and Link *et al.* **[139]** have studied the melting of gold nano-particles using nano-second **[138]** and femto-second **[139]** lasers. Chang observed that different laser fluences can lead to different phase transitions and shapes of nano-rods. In another experiment, Link found that it takes tens of pico-seconds for nano-rods to melt, which seems to imply that a small volume of nano-particles results in rapid heating and cooling effects. In the case of a nano-second laser, a longer pulse duration leads to cumulative temperature effects **[138]**, but the nano-antennas may cool down more quickly because of their small footprint, which suggests that each pulse is independent in the heating of these structures ($p = 0$). However, it should be mentioned that it takes a much longer time for the substrate to completely return to room temperature because of its considerably larger volume.

Rigorous modelling of melting effects in plasmonic nano-antennas is generally hard to achieve. For nano-second pulses, the duration of each pulse is significantly longer than the lattice heating time, which results in thermalization between the electron subsystem and the lattice **[138]**, whereby the system can be studied by solving the heat diffusion equation.

5.3.5 Heat distribution modelling

The temperature distribution in the structures illuminated by a laser is analyzed by solving a heat equation using COMSOL software **[92]**. Generally, the heat transfer in the system can be written as:

$$Q = c_v \frac{\partial T}{\partial t} + \nabla(-\chi \nabla T)\,, \tag{5.7}$$

where Q is the heat source term proportional to the laser intensity, $c_v = \rho \cdot c_p$ is the volumetric heat capacity (ρ is the material density and c_p is the specific heat capacity), T is the temperature and χ is the thermal conductivity. In the first approximation, it is assumed that the studied structures are considerably smaller than the laser spot area, which is true for nano-antennas and mm-sized beam diameters, thus, the laser intensity can be treated as a constant for the examined space. Also, the adduced calculations imply nano-second pulses that are significantly longer than the lattice heating time (0.01-0.1 ns). This means that, at each given moment, the system will remain in thermal equilibrium ($\partial T / \partial t = 0$) and both electrons and lattice can be described as having the same temperature T **[140]**. The heat coefficients used in Eq. 5.7 are summarized in Table 5.3.

Table 5.3 – Heat coefficients for gold, air, titanium and quartz

Material	Volumetric heat,capacity, $J \cdot cm^{-3} \cdot K^{-1}$	Thermal conductivity, $W \cdot m^{-1} \cdot K^{-1}$
Gold	2.492	318
Air	0.00121	0.0257
Titanium	2.359	22
Quartz	1.661	1.3

There are two main mechanisms that can cause thermal damage to the considered structures:

1) Direct laser heating of the exposed material;

2) Heating due to the enhanced localized electric field (plasmonic heating) that arises in the region around the nano-antenna gap.

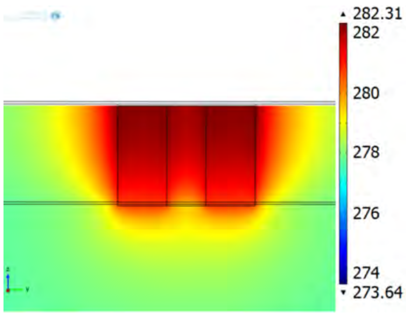

Fig. 5.8 – Qualitative temperature distribution in titanium nano-antenna (temperature is given in °C)

Fig. 5.8 shows the qualitative temperature profile inside the titanium nano-antenna when the laser light reaches its surface. It is clear that the metallic and air gap regions have higher temperatures than the surrounding air and quartz substrate. This thermal distribution indicates that the heat generated by the nano-antenna is not efficiently dissipated, which leads to a formation of hot spots in the metallic areas.

5.4 Experimental Results

5.4.1 Experimental setup overview

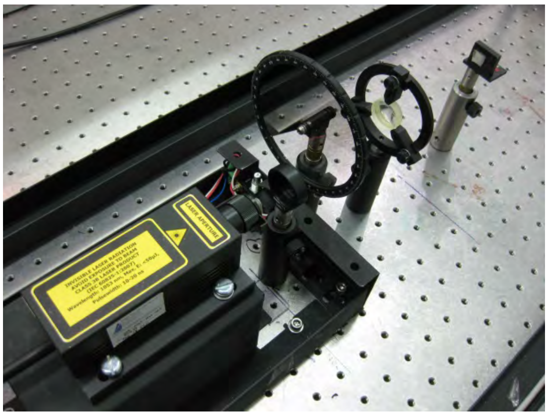

Fig. 5.9 – Q-switch laser setup

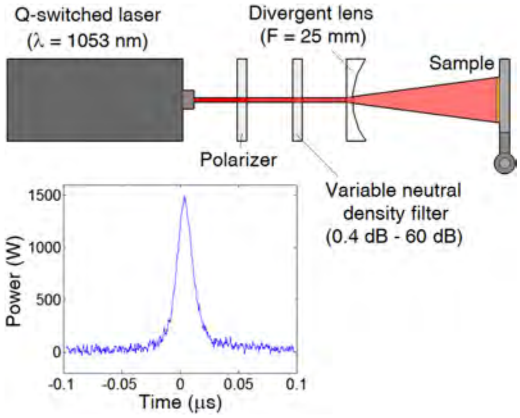

Fig. 5.10 – Experimental setup. Inset – single-pulse profile

The experimental setup is presented in Fig. 5.9 (photo) and Fig. 5.10 (sketch). A commercial Q-switched laser operating at 1053 nm with a single-pulse energy of 15 μJ is used in the experiments (the single pulse profile is shown in the inset in Fig. 5.10). The duration of each pulse is 10 ns, the total exposure time is 300 s and standard repetition rate is 5 kHz. Although, in some experiments, the repetition rate is varied from 2 to 10 kHz and the exposure time is changed from 300 to 1000 s, no significant differences in the results are observed. A variable metallic-film neutral density filter that allows the attenuation to be altered from 0.4 to 60 dB is used to control the incident fluence. The original spot size of the laser beam φ_{spot} is 2 mm in diameter, but it can be expanded to larger values using a divergent lens with a focal length of 25 mm. On the whole, it is possible to change the laser fluence over a wide range of values (by more than 80 dB). Also, to ensure that the main electric field is along the *x*-axis, as in Fig. 5.1, a polarizer is placed between the Q-switched laser and lens.

Sample positioning is performed at the maximum attenuation of 60 dB and the invisible radiation of 1053 nm is visualized using a fluorescent laser viewing card. During the experiments, the laser is enclosed in a laser safety box and is externally modulated by a signal generator with the On-Off shift keying.

5.4.2 Nano-antenna fabrication

As previously mentioned, the thickness of the metal (gold or titanium) is 300 nm and the materials are deposited using EBE. In the case of the gold nano-antennas, a 2 nm thick titanium layer is added on top of the quartz to improve adhesion. Then, the structures are milled using a FEI Helios NanoLab 600 dual-beam FIB system, as discussed in Chapter 4. The area occupied by the patterns is about 100 µm by 100 µm and the total sample area is 1 cm^2. The refractive indices of gold and titanium at 1053 nm are $n_{Au} = 0.23 - 7.10i$ and $n_{Ti} = 3.453 - 4.004i$, and their reflectivities are about 98% and 62% respectively.

5.4.3 Assessment of thermal damage using SEM

Figs. 5.11a-5.14b show SEM images of the fabricated gold and titanium nano-antennas before and after the experiments. They are grouped in pairs, which consist of the original (left, with index *a*) and melted (right, with index *b*) structures. It can be seen that, even for the intact nano-antennas (Figs. 5.11a-5.14a), the walls are not perfectly vertical and, therefore, the gap widths are always estimated at the mid-height of the gold (or titanium) region. In Fig. 5.11a and Fig. 5.12a, the gap width is about 60 nm and, in Fig. 5.13a and Fig. 5.14a, it is 120 nm.

After exposure to the laser light at a given fluence, the potential damage to the nano-antennas is assessed by taking more SEM images (Figs. 5.11b-5.14b). The experiments are primarily focused on two samples with gap widths of 60 nm and 120 nm, while structures with other gap widths are also fabricated. The damage fluence thresholds are measured mainly for the 60 nm gap nano-antennas and, for the gold one, the single-pulse damage fluence is $F_s = 0.059$ J/m^2 and total exposure fluence is $F_{ex} = 88.5$ kJ/m^2 ($T_{ref} = 300$ s, $f_{rep} = 5$ kHz). Note that the main damage to the gold nano-antenna occurs around its central gap region, where the field enhancement value is the highest (Fig. 5.11b and Fig. 5.13b). In fact, the melting of the metallic regions fills this space with gold. The 120 nm gap gold nano-antenna becomes thermally damaged at a higher fluence, but it is difficult to determine its exact threshold fluence because of the discrete attenuation steps of the variable metallic-film neutral density filter. However, based on the experimental results, it is approximately less than double the fluence of the 60 nm gap.

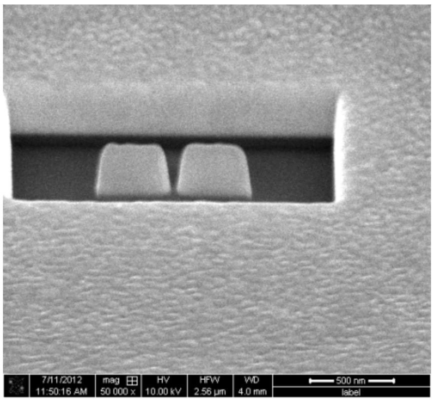

Fig. 5.11a – SEM image of original 60 nm gap gold nano-antenna

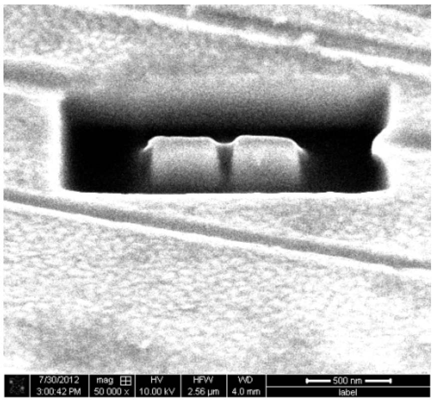

Fig. 5.11b – SEM image of melted 60 nm gap gold nano-antenna

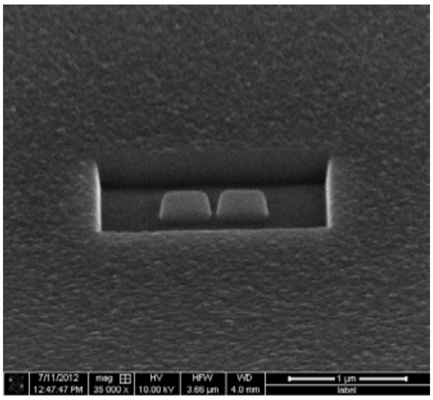

Fig. 5.12a – SEM image of original 60 nm gap titanium nano-antenna

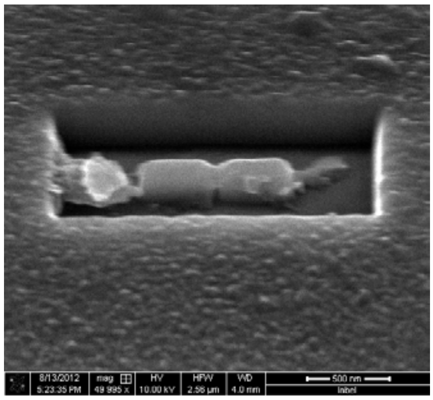

Fig. 5.12b – SEM image of melted 60 nm gap titanium nano-antenna

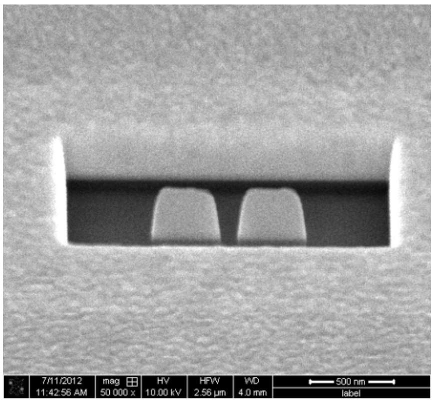

Fig. 5.13a – SEM image of original 120 nm gap gold nano-antenna

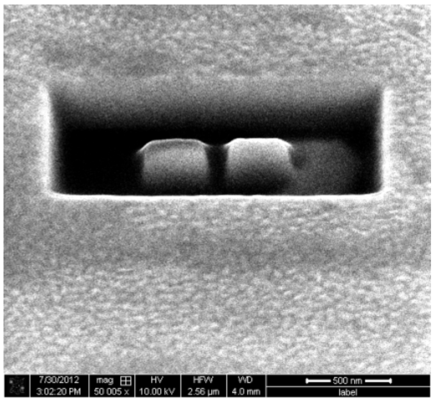

Fig. 5.13b – SEM image of melted 120 nm gap gold nano-antenna

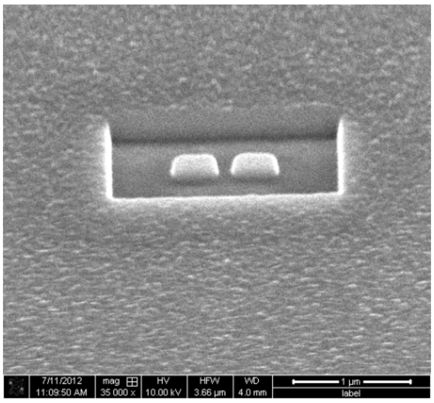

Fig. 5.14a – SEM image of original 120 nm gap titanium nano-antenna

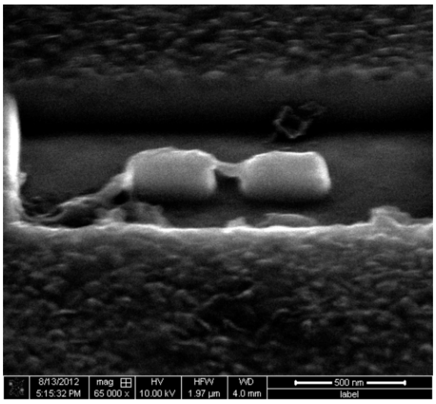

Fig. 5.14b – SEM image of melted 120 nm gap titanium nano-antenna

As expected, the titanium nano-antennas prove to be more resistant. After exposing the 60 nm gap titanium structure (Fig. 5.12a) to laser light for a period of 5 minutes, the damage single-pulse fluence is estimated to be 4.35 J/m^2, while the total exposure fluence is 6525 kJ/m^2. The 120 nm gap titanium nano-antenna (Fig. 5.14a) also eventually melts, but, like for its gold counterpart, it is difficult to determine the exact damage fluence.

The damaged titanium nano-antennas are shown in Fig. 5.12b and Fig. 5.14b. In comparison with the gold structure, for a 60 nm gap, the damage threshold fluence increases by a factor of 74, although the electric field enhancement reduces by 19% (see the data presented in Table 5.2). Thus, the titanium-based structures can withstand and create about 7 times higher electric fields than the gold nano-antennas and are considerably more power resistant.

Possible explanations for the better performance of the titanium devices over their gold counterparts include: 1) higher melting temperature (1668˚C compared with 1064˚C); 2) greater mechanical strength; and 3) increased penetration depth, which means that the electric fields permeate deeper into metal and the power density is less localized on the surface of a device.

5.4.4 Thermal damage in nano-antennas with different gap widths

While exact measurements are only performed for structures with 60 nm gap, other nano-antennas are also fabricated and qualitatively studied. These gold structures with gap widths varying from 30 to 120 nm are presented in Figs. 5.15a-5.18c. The figures with index *a* correspond to the original intact nano-antennas and those with indices *b* and *c* – to the exposed structures. For figures with index *c*, the stage is tilted at 45˚ to show additional features of the thermal damage. As can be seen from adduced SEM images, although all the samples melt, the structures with narrow gaps experience more damage, which supports the idea of plasmonic heating playing the major role in this process.

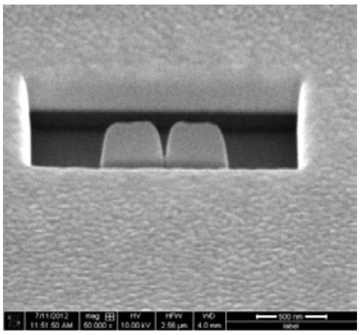

Fig. 5.15a – Original 30 nm gap gold nano-antenna

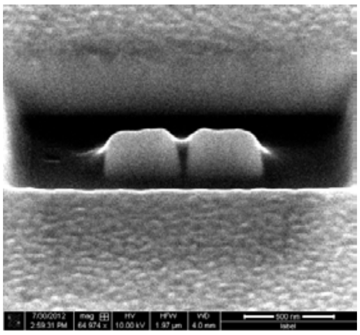

Fig. 5.15b – Melted 30 nm gap gold nano-antenna

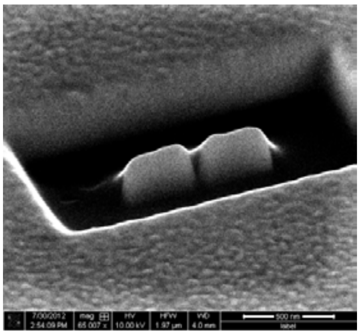

Fig. 5.15c – Melted 30 nm gap gold nano-antenna (tilt 45˚)

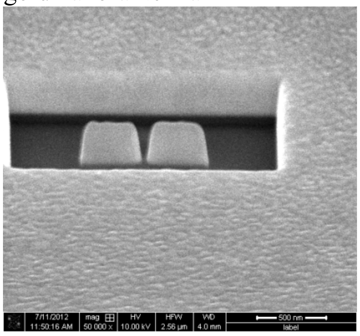

Fig. 5.16a – Original 60 nm gap gold nano-antenna

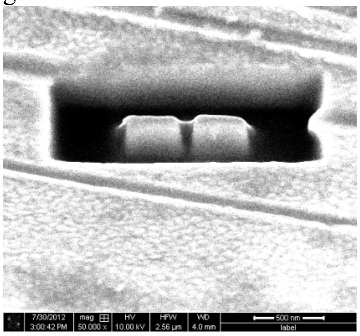

Fig. 5.16b – Melted 60 nm gap gold nano-antenna

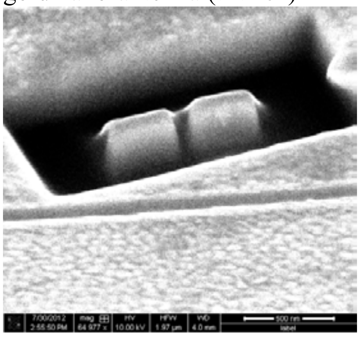

Fig. 5.16c – Melted 60 nm gap gold nano-antenna (tilt 45˚)

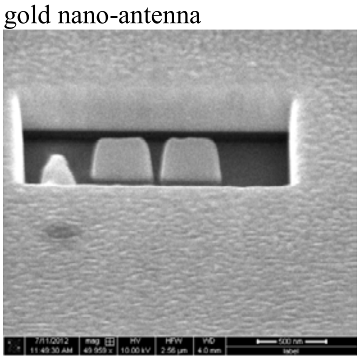

Fig. 5.17a – Original 90 nm gap gold nano-antenna

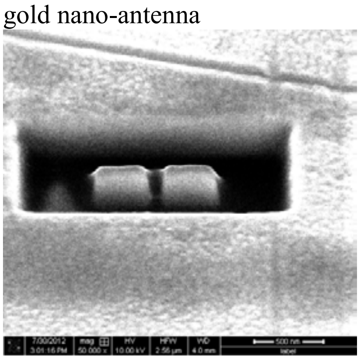

Fig. 5.17b – Melted 90 nm gap gold nano-antenna

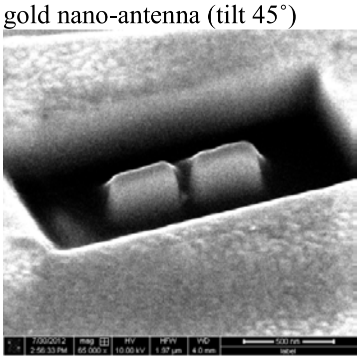

Fig. 5.17c – Melted 90 nm gap gold nano-antenna (tilt 45˚)

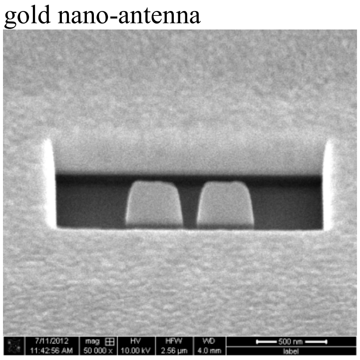

Fig. 5.18a – Original 120 nm gap gold nano-antenna

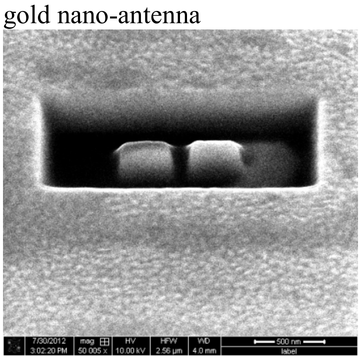

Fig. 5.18b – Melted 120 nm gap gold nano-antenna

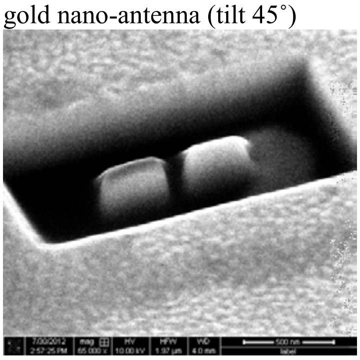

Fig. 5.18c – Melted 120 nm gap gold nano-antenna (tilt 45˚)

5.5 Summary

High-power nano-antennas made of gold or titanium are compared in this chapter. They are excited by nano-second pulses coming from a large spot-size Q-switched laser and are studied both theoretically and experimentally. Firstly, the considered structures are numerically analyzed and the electric field enhancement factor is calculated for gap widths ranging from 15 to 120 nm. This factor varies from 6.67 to 2.84 for gold and from 6.29 to 2.39 for titanium, being on average 19% larger for gold nano-antennas. Secondly, the electric field profiles are considered and it is shown that the highest magnitudes of the field are inside the air gap between the two nano-antenna arms. Also, it can be seen that the field distributions of both nano-antennas are very similar for the *x*-*z* cross-section (the plane perpendicular to the incident radiation) and different for the *x*-*y* cross-section (the plane parallel to the incident radiation). Thirdly, interactions between the laser pulses and nano-antennas are reviewed. It is assumed that, for a nano-second pulse, temperature equilibrium is reached during a single-pulse exposure and then the qualitative heat distribution is calculated. Fourthly, an experiment is conducted, in which the nano-antennas are exposed to laser radiation in order to obtain their threshold damage fluences. The potential thermal damage is later assessed by studying SEM images of the irradiated surfaces and it is shown that titanium-based devices can withstand about 74 times higher fluence than their gold counterparts.

Such combination of a higher damage threshold, but slightly lower field enhancement factor for a titanium nano-structure results in it being capable of producing an almost 7 times higher magnitude of the electric field than a gold nano-antenna. Such titanium-based nano-antennas have potential applications for SERS, nano-imaging, nano-particle detection, nonlinear optics and other high-power designs.

While the nano-antennas considered here are simply excited by an external laser, the light can also be coupled into them using different approaches, as discussed in the introductory chapter. One such possible design is a slot waveguide, which is studied in detail in Chapter 6.

Chapter 6 – Analysis of silica-filled slot waveguides based on hyperbolic metamaterials

6.1 Introduction

While many plasmonic devices can be studied independently, in many applications it is necessary to couple different structures together to form a plasmonic circuit. Typically, the incident light drives only a single element of such a circuit and then the signal is carried to other parts of the circuit through a set of waveguides. Due to their lossy nature, the stable operation of plasmonic circuits requires much larger powers to be pumped into them to ensure that the signal reaches its destination. The strict size requirements for plasmonic circuits always imply a sub-wavelength confinement of light, which, in the case of a nanometre-scale plasmonic waveguide connected to a large high-power source (for example, an optical fiber), results in a substantial increase in power density around the coupling region and makes the temperature handling of a waveguide to be an important issue.

This chapter focuses on such a plasmonic structure, in particular, a silica-filled slot metamaterial waveguide, which is chosen because of the strong field localization inside its gap. Firstly, different methods for light confinement on a nano-scale are discussed and the concept of a slot waveguide is introduced. Secondly, the slot waveguide's geometry and the formation of its fundamental mode are addressed. Thirdly, qualitative temperature distributions are found and the performance of the structure is analyzed over a broad range of wavelengths (1.39-1.7 μm). Fourthly, the problem of power coupling from a wider slab waveguide is considered and the electric field confinements of different slot waveguide configurations are compared.

The obtained data shows that the multilayer structure of the lateral regions provides a reasonable balance between the electric field confinement and propagation losses inside the considered slot waveguide. The proposed device geometry also demonstrates a capability to operate in high power regime and the studies on its optical properties were published in **[141]** and presented at *CLEO 2014* (San Jose, California, USA) **[142]**.

It should be also noted that the material discussed in present chapter is only theoretical due to fabrication difficulties. Although the slot can be milled using FIB, the desired gap is too narrow and its side walls will become significantly tilted during the fabrication process (similar to the nano-antennas discussed in Chapter 5 (Section 5.4)). Alternatively, the slot could be etched with acid, but, this approach doesn't allow the precise control of the gap width, as in the studied multilayer structure the amount of the removed matter could vary between different material layers (the acid will likely considerably corrode the metallic parts of the lateral regions).

6.2 Background information

6.2.1 Light confinement on nano-scale

A general trend in integrated circuit technology is the reduction in sizes of optical components and the increase in their speeds. In this sense, photonics can provide an ideal platform in achieving very high signal transmission rates **[143]**, however its components have to be miniaturized to match the dimensions of current nanometric electronic elements and simple scaling is ultimately limited by the light diffraction. In recent years, many different physical phenomena have been proposed to further reduce the size of current optical components, such as the photonic bandgap effect **[144-149]**, total internal reflection in large-index contrast structures **[150-153]** and excitation of plasmonic waves **[154-159]**. Compared with the other two, plasmonics offers the most promising technology for creating ultra-compact devices, but at the cost of higher propagation losses in metals.

After light is generated and eventually processed inside an optical chip, it must be transported to different regions of that chip by optical waveguides. In contrast to electrical wires, optical waveguides can transmit information at very high rates **[162]**. In general, photonic crystal **[163]** and total internal reflection **[164]** waveguides can reach distances of greater than 100 μm with acceptably small propagation losses. If light is required to be transmitted over longer distances, it can be coupled to optical fibers by using, for example, grating couplers **[165]**. If electro-magnetic radiation needs to be confined in tighter spaces, plasmonic waveguides can be used despite their considerably higher losses **[166-169]**. Slot waveguides are particularly attractive because they can confine light in very small spaces, which is useful for a wide range of applications in nonlinear optics **[160, 161, 170]**.

6.2.2 Introduction to slot waveguides

Dielectric slot waveguides were first demonstrated by Almeida *et al.* **[170]** and were used to guide infrared radiation in areas tens of nanometres in width. Their operating principle is based on the behaviours of the vectors of the electric field E and electric flux density D at the interface of two media. At the boundary, the normal component of D depends only on the free charge density and, for dielectrics, always remains constant, as discussed in Chapter 2 (Section 2.2.3). This, in turn, results in the E-field exhibiting a strong discontinuity, as demonstrated in Section 6.3.2. For a symmetric geometry, in which a narrow low-index "slot" is sandwiched between wide high-index "claddings", such discontinuity leads to strong electric field localization in the former region. Therefore, the slot acts as a guiding medium for modes with their main electric field components directed across it. Simultaneously, the high-index lateral regions on either side of the slot act as a cladding similar to that of a conventional waveguide.

Another important feature of a slot waveguide is its capability to bend without reducing power transmission **[171]**. For example, the silicon on insulator (SOI) slot waveguide (gap width – 50 nm, lateral slab regions – 180 nm wide and 300 nm high, bending radius – 5 μm) embedded in SiO_2 has a transmission in a 360˚ loop of more than 99%, which is equal to 11 dB/cm bending losses **[170]**.

While slot waveguides do offer a tight light confinement, if made only of dielectric materials, they still have some mode leakage, particularly, when the light becomes coupled into them from a conventional stripe waveguide. On the other hand, the presence of metal (as in a MDM waveguide) can considerably increase absorption losses, thereby reducing the transmitted power. In the latter case, the optical radiation is transferred by SPPs propagating along the metal-dielectric interface. It is also possible to guide light by exciting long-range SPPs with typical propagation losses of a 6 dB/cm at infrared frequencies **[68]**. However, this requires the construction of a symmetric geometry, in which a nanometre-thick metallic film is placed between two adjacent cladding dielectric layers **[172, 173]**.

6.3 Theoretical analysis of device

6.3.1 Modelling of lateral slab regions using Maxwell-Garnett theory

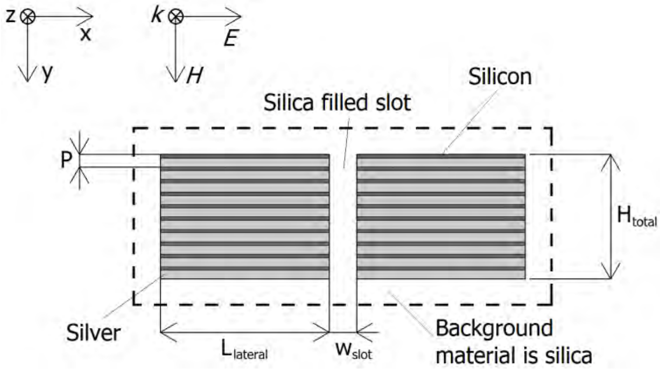

Fig. 6.1 – Cross-section of slot waveguide

A typical slot waveguide is formed by a narrow, low-index slot placed between two high-index slab regions. In the proposed geometry (Fig. 6.1), these slab regions are constructed from hyperbolic metal-dielectric metamaterials capable of supporting large wave vectors (i.e., they exhibit large modal effective refractive index values). Each metamaterial region consists of ten alternating silver-silicon pairs with a period of P = 25 nm **[166]**. The surrounding medium (including the slot) is filled with silica (n_{SiO2} = 1.444) and the waveguide is designed to operate at 1550 nm. A practical benefit of embedding the structure in silica is that this protects the silver inclusions from oxidizing, and filling the slot also prevents the cladding from thermally expanding into it. According to the Maxwell-Garnett theory, the components of the anisotropic homogeneous permittivity tensor can be calculated as **[174, 175]**:

$$\varepsilon_x = \varepsilon_z = f_{Ag}\varepsilon_{Ag} + (1 - f_{Ag})\varepsilon_{Si} \quad (6.1)$$

$$\varepsilon_y = \frac{\varepsilon_{Ag}\varepsilon_{Si}}{f_{Ag}\varepsilon_{Si} + (1 - f_{Ag})\varepsilon_{Ag}}, \quad (6.2)$$

where the directions of the axes are shown in Fig. 6.1, f_{Ag} is the metal filling factor (i.e., the ratio of the silver volume to the volume of the whole lateral slab region) and ε_{Si} = 12.447 is the permittivity of silicon. The Maxwell-Garnett theory is valid when: a) the thickness of the metal-dielectric pairs is significantly smaller than the wavelength of interest (each material layer has nanometre-scale dimensions that are considerably smaller than the optical wavelength); and b) the scattering from the incursions is low (which implies a low density of the conducting domains) **[176]**. Although the given formulae have their limitations, they provide a useful physical insight into the results, but, nevertheless, the model discussed here still remains only a mathematical approximation used to calculate complex permittivity.

The permittivity of silver is found using the Drude model as:

$$\varepsilon_{Ag}(\omega) = \varepsilon_{\infty} - \frac{\omega_p^2}{\omega^2 - i\omega\gamma_c}, \tag{6.3}$$

where $\varepsilon_{\infty} = 5$ is the background dielectric constant, $\omega_p = 1.38\times10^{16}$ rad/s is the plasma resonant frequency, and $\gamma_c = 5.07\times10^{13}$ rad/s is the collision frequency **[62]**. The effective permittivity components ε_x, ε_y and ε_z as a function of the wavelength for $f_{Ag} = 0.6$, calculated using the Maxwell-Garnett theory, are presented in Fig. 6.2.

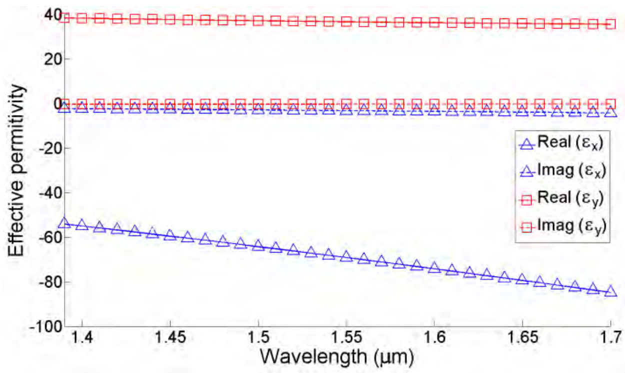

Fig. 6.2 – Effective dielectric permittivities of slab's metal-dielectric regions ($f_{Ag} = 0.6$) calculated using the Maxwell-Garnet theory **[174, 175]**

6.3.2 Formation of slot mode

The slot waveguide can be considered as being the result of interaction between two separate slab waveguides placed close to each other. Each adjacent slab metal-dielectric region can support an eigenmode and, their coupling leads to the formation of either symmetric or anti-symmetric modal profiles in the slot waveguide **[170]**. If the modal profile is symmetric, the electric field strength inside the slot is enhanced and the wave is strongly confined (Fig. 6.3a), while, if it is anti-symmetric, the opposite electric fields cancel each other out and the optical confinement becomes relatively weak (Fig. 6.3b). As previously mentioned, in the considered geometry only modes with their main electric field component directed across the gap (the *x*-axis in Fig. 6.1) are strongly confined inside the slot, whereas those that have their main electric field component parallel to the faces of the gap (the *y*-axis in Fig. 6.1) leak away and rapidly decay **[166]**. Therefore, only the quasi-TM_{00} modes (with, primarily, field components E_x, H_y,

E_z) are considered in this discussion. Although a quasi-TM_{00} mode may contain a residual longitudinal mode component of the electric field, its magnitude is considerably weaker than that of the transverse field (in the mode notations, the first and second sub-indices refer to the numbers of nodes along the *x*- and y-directions respectively).

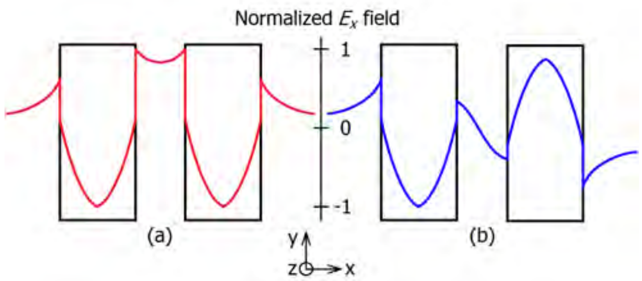

Fig. 6.3 – Electric field profiles for (a) symmetric and (b) anti-symmetric modes (note that the field inside the slot is only amplified for the symmetric case)

For the quasi-TM_{00} coupled mode of a slot waveguide with the width of its lateral slab metal-dielectric regions denoted by $L_{lateral}$ and that of the slot by w_{slot}, the main electric field component inside the gap can be written as **[177]**:

$$E_x = E_0 \begin{cases} n_{eff,z} \cos(-0.5k_x L_{lateral} + \varphi)\Theta(x), & 0 < x < 0.5w_{slot} \\ (n_{eff,z} / \varepsilon_x)\cos(k_x(x - 0.5(L_{lateral} + w_{slot})) + \varphi), & 0.5w_{slot} < x < 0.5w_{slot} + L_{lateral} \\ n_{eff,z} \cos(0.5k_x L_{side} + \varphi)\exp(-\gamma(x - 0.5w_{slot} - L_{lateral})), & x > 0.5w_{slot} + L_{lateral} \end{cases} \quad (6.4)$$

where φ is the phase shift at the middle of each metal-dielectric region that arises from the mode coupling, $\gamma = (k_0^2 - k_z^2)^{0.5}$ is the field decay rate in the silica (k_z is the wave vector in the propagation direction and k_0 is the wave vector for the free space), and $\Theta(x)$ is:

$$\Theta(x) = \begin{cases} \cosh(\gamma x) / \cosh(0.5\gamma w_{slot}) \\ \sinh(\gamma x) / \sinh(0.5\gamma w_{slot}) \end{cases}, \quad (6.5)$$

where the first line corresponds to symmetric and the second – to anti-symmetric modes. The values of the electric fields on opposite sides of the slot (i.e., in the negative *x*-direction) are exactly the same for symmetric and have opposite signs for anti-symmetric modes. As can be seen in Eq. 6.4, at the slot-cladding interface, E_x exhibits a strong jump in magnitude, changing from higher values inside the slot to lower values inside the lateral slab regions.

The electric field confinement in the vertical direction (i.e., along the y-axis) is provided by the lateral high-index regions. Since these regions (which form a cladding of the slot) are sufficiently large to confine the propagating modes vertically, the slot mode originating from their interaction also becomes confined.

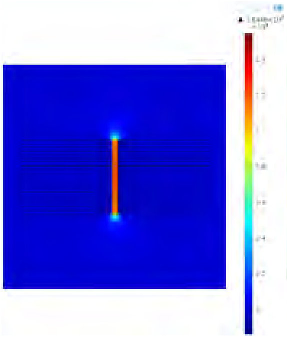

Fig. 6.4a – E_x profile for quasi-TM_{00} fundamental slot mode

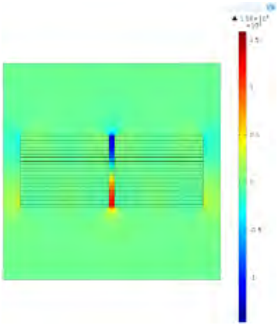

Fig. 6.4b – E_x profile for quasi-TM_{01} slot mode

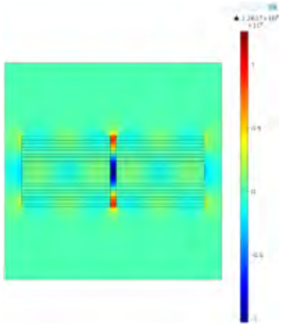

Fig. 6.4c – E_x profile for quasi-TM_{02} slot mode

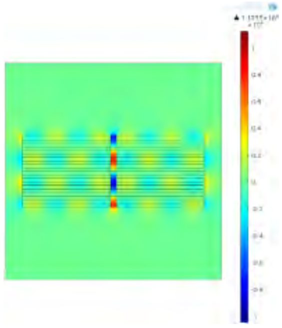

Fig. 6.4d – E_x profile for quasi-TM_{03} slot mode

6.4 Analysis of slot waveguide

6.4.1 Optical properties of slot waveguide

The optical properties of the layered slot waveguide are studied by calculating the modal effective refractive index $n_{eff,z} = k_z / k_0$ of the symmetric quasi-TM_{00} mode using the COMSOL Multiphysics software **[92]**. The waveguide's geometry is simulated as an *x-y* profile, which is semi-infinite in the *z*-direction and each slab metal-dielectric region has a height of H_{total} = 250 nm and width of $L_{lateral}$ = 320 nm (refer to Fig. 6.1 for details). The structure is embedded in a background silica medium with dimensions of 1.5 µm by 1.5 µm, and is surrounded by PMLs. This waveguide geometry is capable of supporting different mode orders: quasi-TM_{00}, quasi-TM_{01}, quasi-TM_{02} and quasi-TM_{03}, which are plotted in Figs. 6.4a-d respectively.

Firstly, the propagation problem is studied by considering the fundamental quasi-TM_{00} mode (Fig. 6.4a) and varying the metal-layer/dielectric-layer thickness ratio for a fixed gap width of 20 nm and wavelengths ranging from 1.39 to 1.7 µm. The calculated effective mode indices are plotted in Fig. 6.5 (real parts) and Fig. 6.6 (imaginary parts) using the following notation: no additional symbol – 25 nm/0 nm (only silver), • – 20 nm/5 nm, ○ – 15 nm/10 nm, × – 10 nm/15 nm, Δ – 7.5 nm/17.5 nm, ▽ – 5 nm/20 nm and □ – 0 nm/25 nm (only silicon). The modal effective refractive index gradually increases as the volume fraction of the dielectric material (i.e., silicon) becomes larger, which may be attributed to the slot waveguide's resonance that arises from the enhanced field coupling between its lateral slab regions. On the other hand, $n_{eff,z}$ decreases with an increasing metallic fraction and demonstrates a tendency to match the properties of a purely silver plasmonic slot waveguide. It is possible to achieve even higher values of the modal effective refractive index by using very thin silver films but, as a trade-off, the imaginary part of $n_{eff,z}$ will also become larger, thereby increasing propagation losses.

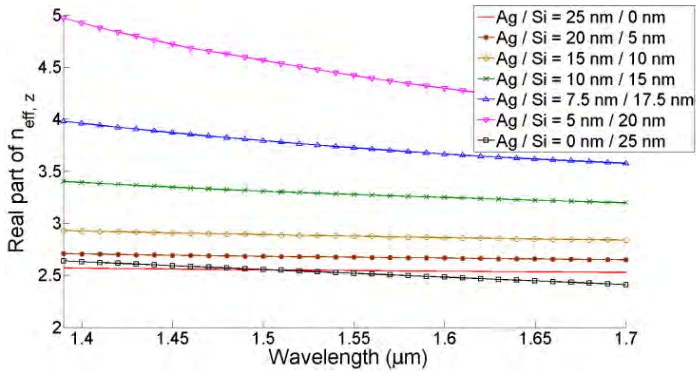

Fig. 6.5 – Real parts of modal effective refractive indices

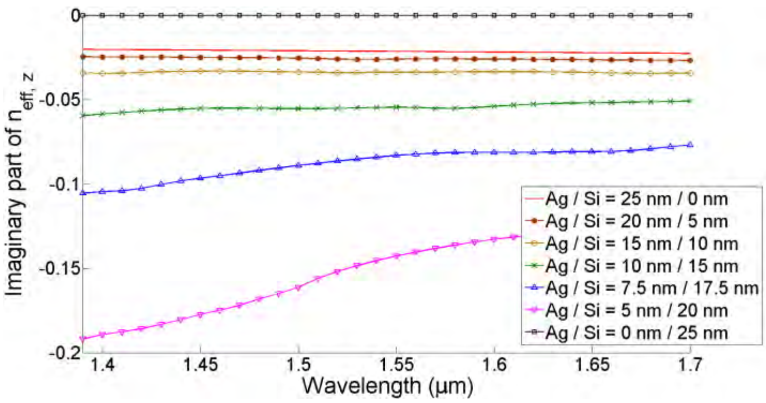

Fig. 6.6 – Imaginary parts of modal effective refractive indices

Now, the slot waveguide's effective indices are examined for several different gap widths. The Ag/Si ratio is selected to be 15 nm/10 nm and the distance between the two metal-dielectric slab regions is increased progressively from 10 to 300 nm, as shown in Fig. 6.7. As expected, the narrow gap of 10 nm has the highest modal effective refractive index of $n_{eff,z} = 4$ due to the strong field localization inside the slot region while gaps wider than 140 nm show poor confinement since the structure effectively transforms into two weakly coupled, finite-width slab waveguides. For this case, the further reduction in the modal effective refractive index of the silica-filled slot is explained by its gradual approach to the refractive index of a bulk silica region, i.e., $n_{SiO2} = 1.444$.

The variations of the external dimensions of the metamaterial cladding do not considerably affect $n_{eff,z}$ (~5% magnitude changes), while gap width and silver filling factor are kept constant, allowing a reasonable structure scaling to fit the geometry requirements of a particular application. In addition to that, the modal effective refractive index is neither influenced by the partial silica removal from outer sides of the lateral slab regions as long as this material is still filling the slot, which enables even more flexibility in an integration of the proposed waveguide into existing plasmonic devices.

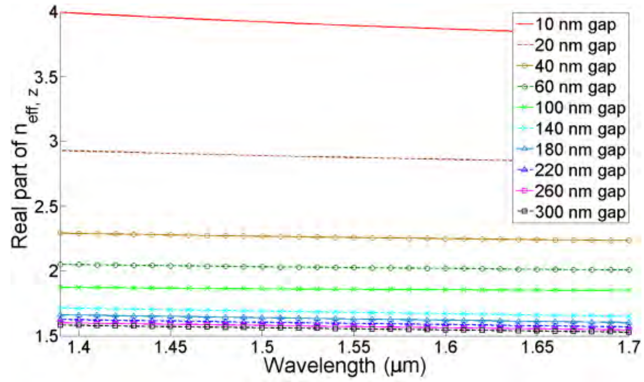

Fig. 6.7 – Waveguide modal effective indices for different slot widths

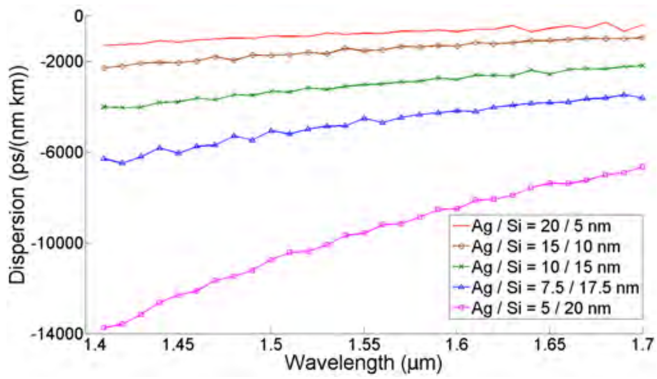

Fig. 6.8 – Dispersion properties of waveguide with 20 nm slot width

The slot waveguide is also studied for its dispersion properties, which are calculated via the dispersion coefficient defined by:

$$D(\lambda) = -\frac{\lambda_0}{c}\frac{\partial^2 n_{eff,z}}{\partial \lambda_0^2}. \tag{6.6}$$

The dispersion coefficients, expressed in units of ps/(nm×km), for a 20 nm wide silica-filled slot are shown in Fig. 6.8. All the silver/silicon thickness ratios have negative dispersions with magnitudes in the order of 10^4 ps/(nm×km) or lower. As previously mentioned, larger values of the silicon fraction (such as the Ag/Si ratio of 5 nm/20 nm) allow stronger coupling between the modal electric field and highly dispersive metallic regions, which results in higher magnitudes for the slot waveguide's dispersion. The oscillations in the dispersion curves are attributed to round-off errors and the precision of the numerical calculation of $n_{eff,z}$ is accurate to 4 significant digits after the decimal point. Since no smoothing is performed for the effective refractive index data, possible numerical and round-off errors can accumulate and lead to random fluctuations in the calculation of the second derivative. Although high dispersion magnitudes can be disadvantageous for some devices, the wave will decay to virtually zero before the group delay will affect the guided mode significantly.

Finally, for the slot waveguide with a gap width of 20 nm, a metal/dielectric ratio of 15 nm/10 nm and wavelength of 1550 nm, the ratio of the group delay $\Delta\tau$ to the spectral line width $\Delta\lambda$, calculated as $\Delta\tau / \Delta\lambda = D \times L_{propag}$, is found to be -3.5×10^{-5} s/nm. In many applications, variations in the group delay are not crucial, but could become a problem in high-speed or broadband systems.

6.4.2 Thermal modelling of slot waveguide

The slot waveguide's temperature profile is calculated by assuming plasmonic heating originating from SPP excitation on the interface between the silver and silica inside the gap region. Calculations are performed for the Ag/Si thickness ratio of 15 nm/10 nm and gap width of 20 nm, with the heat coefficients presented in Table 6.1.

Table 6.1 – Heat coefficients for silver, silicon and silica

Material	Heat capacity at constant pressure, $J\cdot kg^{-1}\cdot K^{-1}$	Thermal conductivity, $W\cdot m^{-1}\cdot K^{-1}$
Silver	230	429
Silicon	700	130
Silica	703	1.38

As could be expected, the heat is mostly localized inside the slot and does not penetrate deep into the surrounding silica region because of the material's low thermal conductivity (Fig. 6.9). Both silica and silicon have melting points significantly higher than that of silver (~1900°K and ~1700°K compared with ~1240°K). This means that, if the silver film melts, it still remains locked by the surrounding medium; however, the differences between the volumetric heat expansion coefficients of the constituent materials may negatively affect the device's solidity. Such issue can be overcome by partially removing silica from the outer sides of the lateral slab regions to provide sufficient space for material expansion (note that the field confinement won't change since the silica remaining in the slot will prevent these regions from changing their dimensions). Additionally, even if both the silicon and silver layers melt and become intermixed, after cooling, the optical properties of the slot waveguide won't change since the numerical simulations in Section 6.4.1 assume an effective medium approach, i.e., they are already not constrained by the explicit geometry of the silver/silicon layers.

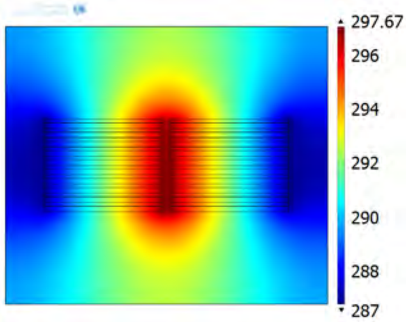

Fig. 6.9 – Qualitative temperature distribution in metamaterial slot waveguide (temperature is given in °C)

Finally, it should be noted that multilayer geometries similar to that of the considered metamaterial lateral regions, can be used as thermal emitters or absorbers for photovoltaics **[50, 54, 55]**. However, in these applications, the thermal energy propagates perpendicular rather than parallel to the structure's layers.

6.5 Coupling stripe and slot waveguides

6.5.1 Analysis of power transmission

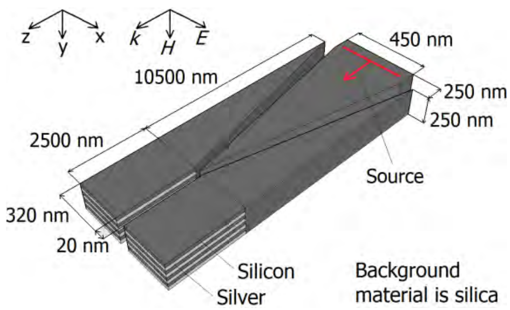

Fig. 6.10 – Slot waveguide coupled with stripe waveguide

Although a slot waveguide can be coupled directly to a conventional stripe waveguide, this may be very inefficient at infrared frequencies for nanometre-scale slots because of the large differences among the distributions of the optical modes **[178, 179]**. One way to improve the coupling efficiency between two butted waveguides is to combine mutually complementary tapers **[180]**: the end of the input stripe waveguide is tapered and then inserted into the slot; the lateral regions of the slot waveguide are also tapered and are formed into a Y-shaped channel to fit the tapered end of the stripe waveguide (as shown schematically in Fig. 6.10). With a reduction in the taper width, the light emitted by the stripe waveguide leaks into the two adjacent gaps between the complementary tapers. As the wave propagates further, these gaps also become narrower and eventually merge to form a single slot.

The coupled waveguide is further studied using the commercial FDTD software **[90]**. The quasi-TM_{00} wave originates at the beginning of the taper and propagates in the *z*-direction, as shown in Fig. 6.10. The source is positioned in the middle of the stripe waveguide's cross-section (in the *x*-*y* plane) and has a mode-field profile. The computational region is terminated by PMLs and the numerical mesh is set to be non-uniform, becoming denser close to the metal-dielectric interfaces. The grid sizes chosen for the silver regions are $\Delta x = \Delta y = \Delta z = 2.5$ nm and for the silicon regions are $\Delta y = 2.5$ nm, $\Delta z = 100$ nm and $\Delta x = 5$ nm. The results obtained for finer meshes ($\Delta y = 1.25$ nm) are only 2% different from those for coarser ones, but the simulation memory requirements increase by a factor of 2. The calculation time-step used in the simulations is 5×10^{-18} s, which is below the stability limit, and the material dispersion data is loaded from the software's inbuilt library **[90]**.

The input/output coupling efficiency is determined by the amount of transmitted power measured at several points along the waveguide's axis: a) before the source; b) immediately after the source; c) at the end of the taper; and d) equidistantly inside the slot waveguide. The calculated power levels are then normalized with respect to the power recorded next to the source and the geometrical dimensions of the structure are varied in order to find the maximum transmission. For a purely dielectric structure, almost 98% of the incident light is coupled into the slot waveguide, with most of the remaining light scattering back towards the source, and the normalized reflection level not exceeding approximately 1%. The transmitted power levels calculated as a function of the distance travelled are shown on common logarithmic scales in Fig. 6.11a and Fig. 6.11b for 20 nm and 60 nm slot widths respectively. The following notations are applied in the plots: no additional symbol – 25 nm/0 nm (only silver), • – 20 nm/5 nm, ○ – 15 nm/10 nm, × – 10 nm/15 nm, □ – 0 nm/25 nm (only silicon). For both slot widths, the highest power transmission is obtained for the purely silicon slot waveguide and the lowest for the MDM waveguide. For slot waveguides with lateral slab regions formed by the hyperbolic metamaterial, the power is transmitted by both SPP propagation at the metamaterial/silica interfaces and the fundamental slot-confined quasi-TM_{00} mode that originates from the lateral coupling between the silicon layers. Because of their high propagation losses, the SPP transmission components decay rapidly for all samples (except for an Ag/Si ratio of 15 nm/10 nm), which results in the slot-confined mode being the primary mechanism for power transmission for distances greater than 1.5 µm. The Ag/Si ratio of 15 nm/10 nm provides the smallest power attenuations of -13.85 dB (20 nm gap) and -8.56 dB (60 nm gap), which may be attributed to the partial excitation of long-range SPPs that can propagate for distances of tens of micrometres before fading. The lower input values for the slot waveguides with silver inclusions (i.e., the insertion losses) are explained by the weaker coupling of light into them as infrared radiation scatters more intensively from the metal-dielectric interface in the tapered region. The differences in the slopes of the curves for the considered silver/silicon ratios may be attributed to the simultaneous excitation of higher-order modes in addition to the fundamental quasi-TM_{00} slot mode. However, these modes decay swiftly due to the large imaginary parts of the modal effective refractive indices and their impact on power transmission at distances greater than 1 µm becomes negligible.

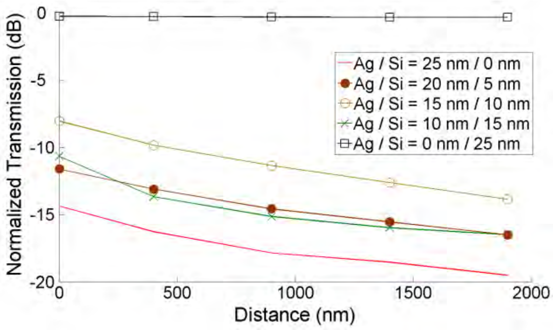

Fig. 6.11a – Normalized transmission for the 20 nm gap width

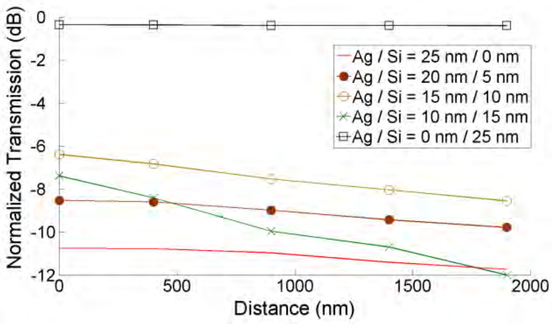

Fig. 6.11b – Normalized transmission for the 60 nm gap width

As can be seen in the plots, both gaps demonstrate similar behaviour of the normalized transmission. Generally, the wider gap is capable of transmitting more power, since the effective volume, in which the wave propagates, increases (the silica-filled slot is modelled as lossless), while the volume, where absorption takes place, doesn't change (the lateral slab regions have the constant outer dimensions of 320 nm by 250 nm). However, the improved transmission results in the reduction in *E*-field confinement as is discussed in Section 6.5.2.

6.5.2 Field confinement inside slot waveguide

To estimate the wave confinement inside the silica-filled slot waveguide, the electric field strength is compared for different silver/silicon layer thickness ratios. The modal E_x component is recorded at equidistantly spaced points (monitors) over the *x*-*y* cross-section at the slot waveguide's end. The distance between these monitors (marked in red in Fig. 6.12) is 20 nm in the lateral and 75 nm in the vertical directions. The field values in the vertical intermediate points (shown in grey in Fig. 6.12) are interpolated using cubic Hermite splines similar to the calculations performed in Chapter 5 (Section 5.3.3) with the spacing between interpolated points being equal to 18.75 nm. The positions of the lateral slab regions for a 60 nm gap width are schematically indicated by solid black lines.

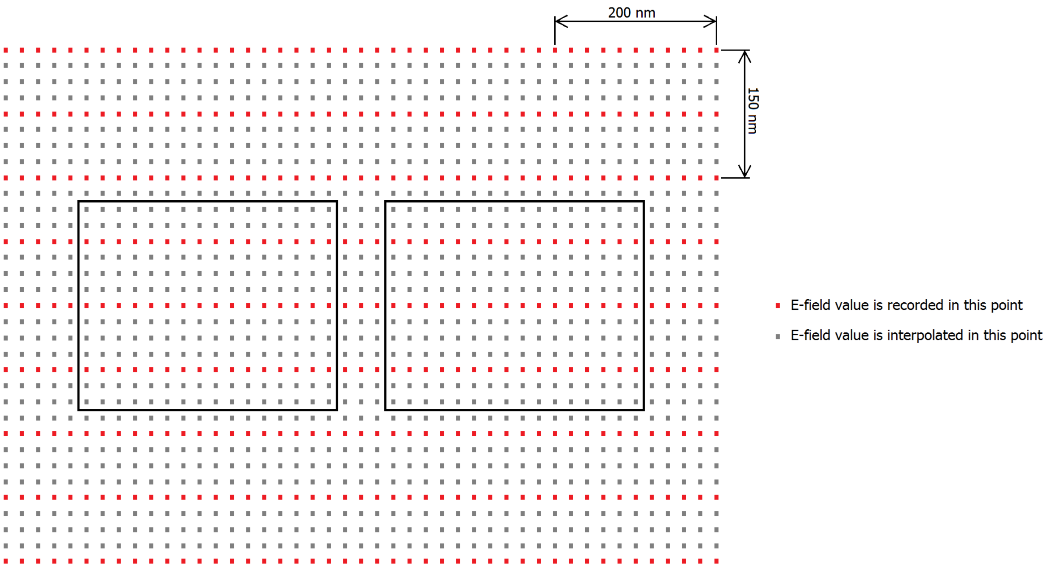

Fig. 6.12 – Spatial positions of points for recorded (red) and interpolated (grey) electric field values

The electric field distributions expressed on a base-10 logarithmic scale are shown in Figs. 6.13a-c for a 20 nm slot width and in Figs. 6.14a-c for a 60 nm slot width. The logarithmic values of E_x are normalized with respect to the highest logarithmic value in the middle of the slot. This means that the normalized values may vary between unity (the highest E_x magnitudes) and negative infinity (the lowest E_x magnitudes expressed in dB).

In the following discussion, the wave confinement is quantitatively evaluated as the ratio of the $|E_x|$ value in the middle of the slot to the $|E_x|$ value inside the lateral slab regions. Thus, higher ratios correspond to better confinement and vice versa.

The confinement for the purely dielectric waveguide (Fig. 6.13a/Fig. 6.14a) is not very strong as the electric field maximum is localized not only inside the slot, but also extend considerably into the adjacent lateral regions, as demonstrated by *Almeida et al.* in **[170]**. For a 20 nm gap width, the magnitudes of the modal electric field strengths in adjacent regions are approximately 20 times (in terms of absolute values) lower than the E_x magnitude for the field maximum inside the slot. The field distribution for a slot waveguide with a silver/silicon layer thickness ratio of 15 nm/10 nm shows better confinement (Fig. 6.13b/Fig. 6.14b). Although E_x is non-zero in the hyperbolic metamaterial lateral regions, it is less than 0.01% of the field maximum value inside the slot. Finally, for the MDM waveguide, the electric field is strongly confined inside the slot and no light significantly penetrates into the lateral slab regions (Fig. 6.13c/Fig. 6.14c).

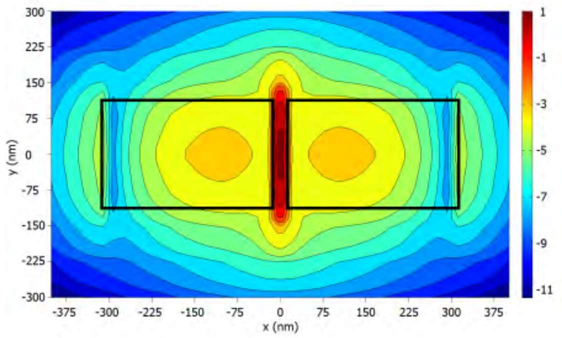

Fig. 6.13a – Normalized E_x profile on base-10 log scale for the 20 nm gap and Ag / Si = 0 nm/25 nm

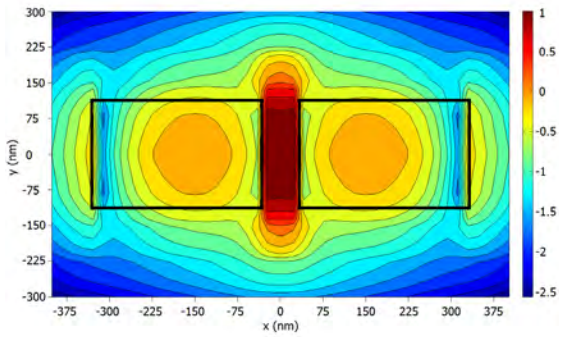

Fig. 6.14a – Normalized E_x profile on base-10 log scale for the 60 nm gap and Ag / Si = 0 nm/25 nm

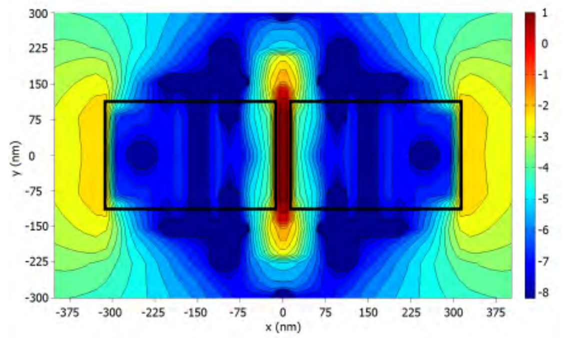

Fig. 6.13b – Normalized E_x profile on base-10 log scale for the 20 nm gap and Ag / Si = 15 nm/10 nm

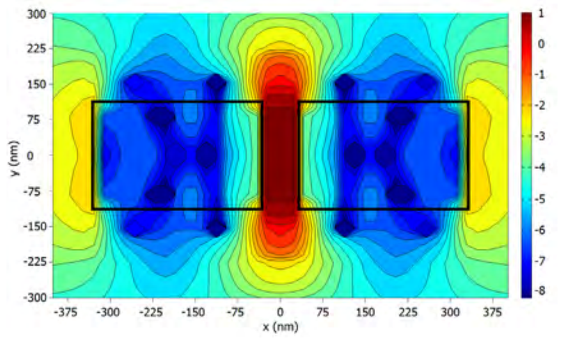

Fig. 6.14b – Normalized E_x profile on base-10 log scale for the 60 nm gap and Ag / Si = 15 nm/10 nm

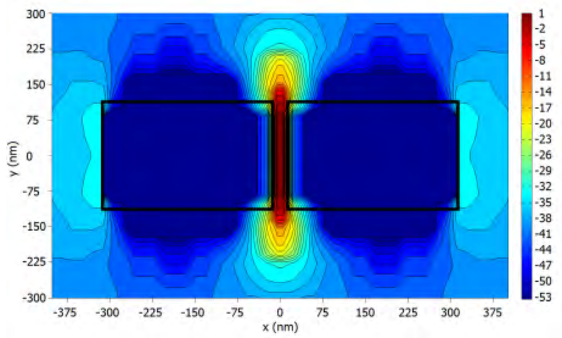

Fig. 6.13c – Normalized E_x profile on base-10 log scale for the 20 nm gap and Ag / Si = 25 nm/0 nm

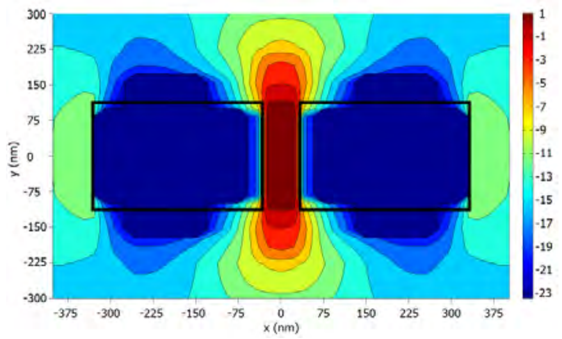

Fig. 6.14c – Normalized E_x profile on base-10 log scale for the 60 nm gap and Ag / Si = 25 nm/0 nm

As mentioned in the previous section, a wider slot results in a weaker field confinement in terms of E_x magnitude ratios. It is clear from the field profiles that the amount of radiation, which remains in the lateral slab regions, is much higher for 60 nm than for 20 nm gaps. It is most evident for a pure dielectric slot waveguide, as can be seen by comparing Fig. 6.13a and Fig. 6.14a.

6.6 Summary

This chapter discusses the silica-filled slot waveguide with lateral slab regions formed by alternating metal-dielectric multilayers. This structure is used for the sub-wavelength confinement of light in the silica-filled slot in the short-wavelength infrared region. Numerical simulations show that high modal effective indices can be obtained for propagating waves that have their main electric field component directed across the gap.

Initially, the performance of the slot waveguide is analyzed for different metal-dielectric ratios. It is found that $n_{eff,z}$ decreases as the amount of metal becomes higher, which is attributed to the progressive transformation of the considered structure into a purely silver plasmonic waveguide. The slot width variations demonstrate the increase of $n_{eff,z}$ in narrower gaps because of the tighter field confinement, and the calculations of waveguide's dispersion properties show that samples with smaller volumes of metal tend to be more dispersive.

The qualitative thermal simulation demonstrates heat localization inside the gap region, and, due to the structure's geometry, its optical properties shouldn't be greatly affected by a temperature rise, as long as the silica-filled slot does not change in width.

Chapter 6 also studies the light coupling from a conventional stripe waveguide. The highest transmitted power level is obtained for a coupled geometry with an Ag/Si ratio of 15 nm/10 nm, which is 3.5 times higher than that for the MDM structure of the same dimensions and is attributed to lower insertion losses. Finally, it is found that using hyperbolic metamaterials as a lateral cladding region for the silica-filled slot waveguide results in significant enhancement of the sub-wavelength confinement of light being 99% greater than for a silicon-only waveguide (in terms of the normalized electric field values inside the slot).

While guiding light over long distances (more than several micrometres) could be an important issue because of intrinsic metallic propagation losses, the proposed slot waveguide design has significant potential for the construction of photonic circuits and integrated devices such as micro-lasers or nano-antennas. These miniature waveguides can confine light in a very small transversal region (less than 100 nm) and may be used in the fabrication of very compact devices (with typical lengths of less than 1 μm), such as short-distance optical interconnects, modulators, switches and couplers. Other possible applications include optical trapping, nonlinear optical devices and dispersion compensation for sufficiently high-power modes.

The dipole nano-antenna and multilayer slot waveguide discussed in Chapters 5 and 6 are aimed at withstanding large fluences to allow these devices to operate in high-power regimes. Although, in both cases, the structures' designs and constituent materials are adjusted to prevent thermal damage, it would be interesting to exploit the thermal vulnerability of a plasmonic device instead of preserving it. A study of a thermal deformation that accompanies the melting process may provide useful insights into the underlying physical mechanisms triggered by light absorption and plasmonic heating. Such a study can be conducted by, for example, observing microbump and nanojet formations on the surface of a fishnet metamaterial exposed to high-power laser radiation, as discussed in the next chapter.

Chapter 7 – Fishnet metamaterials with incorporated titanium absorption layer

7.1 Introduction

The devices discussed in the two previous chapters were developed to operate stably even in a high-power regime. This was achieved by combining resilient materials with suitable structure designs, which made them mostly tolerant to heat effects. However, this does not mean that in high-power applications the exposed surfaces always remain intact. In some cases (such as thermal fuses), the melting process becomes an integral part of the device's performance **[181]**. In these situations, the structure's thermal resistivity usually turns out to be an obstacle and the sensitivity of its durability to a temperature rise is actively exploited. For plasmonic devices, such sensitivity can be easily observed in resonant structures, the temperatures of which may rise dramatically because of increased absorption around their resonant frequencies, for example, as it occurs in metamaterials **[182]**.

The present chapter focuses on thermal deformations in a fishnet metamaterial induced by intensive near-infrared laser radiation. As in all cases of laser-medium interactions, the heating in the exposed structure arises from both the absorption of light by the material itself and the excitation of plasmonic effects. The material component of absorption is further enhanced by depositing an additional titanium layer on top of a fishnet structure and the plasmonic heating is supplemented by the resonant behaviour of the effective refractive index (which becomes negative over a narrow band of wavelengths). The combination of these two factors reduces the damage threshold of the fishnet metamaterial by nearly 50% and leads to thermal deformation of the exposed areas.

This chapter begins by providing an overview of the metamaterial research field and different types of these structures. Then, details of the fishnet design and calculations of the effective refractive index are presented. Next, the absorption spectra of structures are found for different volume fractions of the titanium absorptive layer. In the experimental sections, the fabricated patterns are exposed to a 1064 nm CW Nd:YAG laser in order to determine their damaging power thresholds, and the process of thermal deformation is shown as a function of the incident laser fluence.

The results reveal that total absorption initially rises as the thickness of the top titanium layer increases, but then starts to drop, as the plasmonic resonance becomes weaker. The formation of microbumps and nanojets is also observed and is attributed to the net force of the surface tension, plastic deformation and thermal expansion of the melted material. The obtained data is published in **[183]** and was presented at *ANZCOP 2013* (Perth, Western Australia, Australia) **[184]**.

7.2 General introduction to metamaterials

7.2.1 Overview of different types of metamaterials

In general, the concept of metamaterials implies artificial micro- and nano-structures that allow the control of light propagation in a certain medium. Since the dimensions of metamaterials are significantly smaller than the wavelength of light, the incoming radiation does not distinguish among individual cells, but, instead, treats the whole array as a homogeneous medium. The most important feature of a metamaterial is that its geometry uniquely determines the effective refractive index of the medium and, as such, it is possible to tailor a metamaterial's macroscopic electromagnetic response and bend incident light in any prescribed direction. The strong dependence of the electromagnetic parameters on structure's geometry also provides the capability to change the operating frequency by simply scaling the dimensions of the device: the underlying physical mechanisms won't change as long as metamaterial size remains much smaller than the wavelength of interest.

Nearly all metamaterials rely on the excitation of their electromagnetic resonances, which means that they typically operate in a very narrow band of frequencies; however the broadband regime still can be achieved by making metamaterial tunable **[185-187]** or overlapping several of their resonant peaks **[188, 189]**. Nevertheless, the resonance's position always remains in the same frequency range, for example, ultraviolet, optical, or infrared. From the electromagnetic point of view, a metamaterial can be interpreted as a RLC circuit consisting of a resistor, inductor and capacitor connected in series. Often a structure's geometry is designed in such a way that the electric field is oriented across the capacitor element and the main magnetic field component penetrates the plane of the circuit **[49, 190]**.

Thus far, many different metamaterials operating from ultraviolet to radio frequencies have been experimentally reported. While these structures can have very exotic shapes, most of their geometries fall into one of the following categories:

1) Split-ring resonators (SRRs) are 2D structures, which resemble a letter *c* in the simplest case. They can be fabricated using FIB for infrared wavelengths **[191]** and optical lithography for terahertz frequencies **[185]**, and can be used to study optical magnetism **[192]** or transformation optics at microwaves **[193]**. Other uncommon geometries, such as electric SRRs (ESSRs), *H*-shaped patterns, tilted crosses and structures based on various planar wallpaper groups **[194]** also correspond to the SRR type.
2) Arrays of cut wires or pairs of nanorods are used to create negative-index materials (NIMs), which simultaneously have negative permittivity and negative permeability **[195, 196]**. The electric field in such systems is directed parallel to the rods, while the magnetic field is directed perpendicular to the rods' plane. This results in the formation of symmetric and anti-symmetric currents, which leads to resonant behaviour of the metamaterial's effective refractive index at particular frequencies.
3) Fishnet metamaterials are a further evolution of nanorods concept. These multilayer structures are discussed in more detail in later sections of the present chapter.
4) 3D chiral metamaterials are asymmetric micro- and nano-devices with strong nonlinear properties, with examples of their application including NIM [**197**] and polarization control of a propagating beam [**198**].
5) Complementary shapes of the aforementioned structures utilize the Babinet's principle by, for example, replacing opaque bodies with holes of identical shapes **[199, 200]**. In this situation, the diffraction pattern remains the same except that the complementary transmission T_c becomes $T_c = 1 - T$, where T is an original transmission of an opaque body, which is often realized to simplify the fabrication process.

Despite being a recently emerged concept, applications of metamaterials already vary from constructing NIM structures and observing the nonlinear effects in them **[201-203]** to achieving super resolution in meta-lenses and creating cloaking devices **[204-206]**. Indeed, metamaterial research has truly blossomed, with more than 2000 papers being published each year on various topics in optics, photonics and other related fields **[207]**.

7.2.2 Heating effects in metamaterials

Similar to nano-antennas, many optical metamaterials use gold as their metal component since it has relatively low losses in the optical frequency region. While it has a melting point of only 1064°C under normal conditions, gold is highly reflective and absorbs only a small fraction of the incoming radiation (~3%). On the other hand, materials such as titanium, which is commonly used in plasmonic devices for adhesion purposes **[99, 137]**, have higher absorption rates that can result in quick temperature rise of the surrounding media. While titanium has a higher melting point of 1660°C under normal conditions and remains mostly unaffected during exposure, it can induce deformations in the adjacent gold layers because of the elasto-plastic flow, which lead to microbump and nanojet formations **[208]**. Of all the different negative-index metamaterials microbumps and nanojets are most clearly observed in a fishnet type because of its flat and uniform surface, which makes the latter structure a good candidate for studying these thermal effects.

The impact of temperature-based deformations can play a crucial role in a metamaterial's performance, especially when it is expected to operate under high fluences. In this respect, the thermal damage threshold can be treated as either the maximum amount of power that could be handled by the device before melting (which is important for most optical applications) or the minimum amount of power required by the device to start working (for example, some sensors or thermal fuses in optical circuits). For the sake of clarity, in the following discussion, the damage threshold always implies the minimum power of the incident laser beam sufficient for deformations of the fishnet's surface to become visible. It should be noted that, although the melting process may start at slightly lower power levels, when the liquefied material initially flows inside the fishnet holes, due to their tiny sizes, such deformations are hardly observable without considering cross-sectional slices of the exposed regions.

7.3 Theoretical analysis of device

7.3.1 Fishnet design

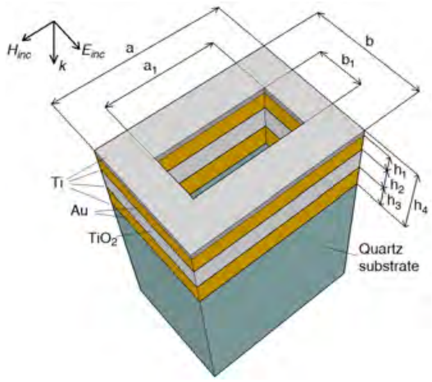

Fig. 7.1 – Fishnet metamaterial cell

As previously noted, the fishnet structure originated from the concept of combined nanorod pairs. In this metamaterial, the space between each metallic pair is first filled with a dielectric, and then the obtained multilayer structures are overlapped to form a double-grating pattern similar to a fisherman's fishing net. The negative refractive index is obtained by the combination of a permeability resonance (which arises from the excitation of anti-symmetric currents in wider metal pairs) and a background negative permittivity provided by shorter metal pairs (that act as a dilute metal) **[49]**.

The fishnet cell considered here consists of three alternating metal-dielectric layers separated by 2 nm-thick adhesive titanium layers, as shown in Fig. 7.1. This metamaterial array has periodical rectangular holes and is placed on top of a quartz substrate. Its upper metallic layer consists of a combination of a gold film and absorptive titanium layer, while its lower metallic layer is made from gold only. The titanium in the upper layer is selected because of its extensive use in plasmonic structures (as mentioned in the previous section) and the presence of this metal is expected to decrease the high reflectivity of the purely gold surface, thereby increasing total absorption. In this case, the titanium can be seen as an extrinsic material placed in immediate proximity to the metamaterial, thus representing either a contamination on the surface of the fishnet structure (that can occur in a non-cleanroom environment) or an unknown substance detected by the fishnet-based sensor.

The proposed geometry is studied using the numerical commercial software CST Microwave Studio 2012 to produce a negative refractive index at 1064 nm (which corresponds to the operating wavelength of the laser in the experiments) and is simulated using a frequency domain solver **[209]**. The metals are modelled as dispersive materials with multiple resonant frequencies according to a multi-resonance Lorentzian model. Due to the design of the measurement setup, the samples are placed in water during the experiments, thus, the superstratum is considered to have a refractive index of $n_{water} = 1.325$. The Floquet ports along the *k*-vector direction (input and output) are terminated by PMLs, while the boundary conditions in the *x*- and *y*-directions are periodical to represent a grating structure. The wave is normally incident on the structure and its mode is assumed to be TM (with the main electric field component directed as shown in Fig. 7.1). The dielectric media, titanium dioxide (TiO_2) and quartz, are assumed to be lossless with refractive indices of 2.7 and 1.53 respectively.

The numerical simulations provide the scattering parameters, which form the scattering matrix (*S*-matrix) of the considered system. This matrix gives the relationship between the incident and reflection amplitudes of the electro-magnetic waves in a *n*-port network **[210]**. Each scattering element S_{ij}, is calculated as a ratio of the reflected wave amplitude coming out of port *i* to the incident wave amplitude coming out of port *j* (all incident waves on all ports except port *j* are set to zero). This means that S_{ii} should be understood as the reflection coefficient from port *i*, when all other ports are terminated in matched loads (i.e., they have no reflection) and S_{ij} should be seen as the transmission coefficient from port *j* to port *i*, when all other ports are terminated in matched loads **[210]**. For a 2-port network problem schematically shown in Fig. 7.2, the transmission and reflectance spectra are calculated from numerically obtained *S*-parameters as $T = |S_{21}|^2$ and $R = |S_{11}|^2$, where index *1* corresponds to the input port (wave incident from the superstratum) and index *2* corresponds to the output port (wave propagating to the substrate).

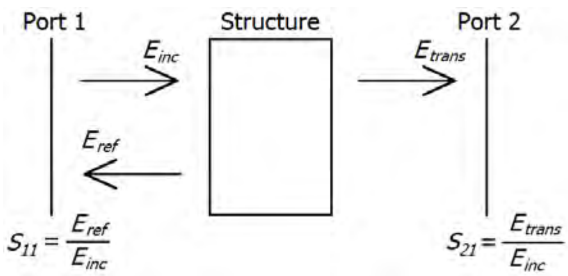

Fig. 7.2 – *S*-parameters in a 2-port network problem

7.3.2 Extraction of effective refractive index

In order to observe the resonant behaviour of the refractive index n, the latter should be first extracted from the calculated S-parameters. Note that for a metamaterial, only the macroscopic effective refractive index n_{eff} and impedance Z_{eff} have any physical meaning. The term “effective” implies that these are averaged values, which make sense only at distances much longer than the wavelength of interest, when the whole structure can be treated as a homogeneous medium **[49]**.

As both the impedance and refractive index are complex values, they should be written as:

$$n = n' + in'' \qquad (7.1) \qquad\qquad Z = Z' + iZ''. \qquad (7.2)$$

where $'$ and $''$ denote their real and imaginary parts respectively (the subscript *eff* is further omitted for the text simplicity). The refractive index and impedance are connected to the dielectric permittivity and magnetic permeability as:

$$\varepsilon = n / Z \qquad (7.3) \qquad\qquad \mu = nZ. \qquad (7.4)$$

According to the Fresnel formulas for a homogeneous slab of thickness h placed in a vacuum under normal incident radiation, the complex transmission coefficient S_{21} and complex reflection S_{11} are **[211]**:

$$S_{21} = \left(\cos(nkh) - 0.5i(Z + 1/Z)\sin(nkh)\right)^{-1} e^{-ikh} \qquad (7.5a)$$

$$S_{11} = -0.5i(Z - 1/Z)\sin(nkh) S_{21} e^{ikh}. \qquad (7.5b)$$

The phase shift e^{ikh} may be eliminated by assuming the normalization notation:

$$S_{21}^{0} = S_{21} e^{ikh} = \left(\cos(nkh) - 0.5i(Z + 1/Z)\sin(nkd)\right)^{-1} \qquad (7.6a)$$

$$S_{11} = -0.5i(Z - 1/Z)\sin(nkh) S_{21}^{0}. \qquad (7.6b)$$

Now, Eq. 7.6a and Eq. 7.6b can be explicitly rewritten for the refractive index and impedance as:

$$\cos(nkh) = \frac{1-(S_{11})^2 + (S_{21}^0)^2}{2S_{21}^0} \quad (7.7)$$

$$Z = \pm\sqrt{\frac{(1+S_{11})^2 - (S_{21}^0)^2}{(1-S_{11})^2 - (S_{21}^0)^2}}\,. \quad (7.8)$$

The obtained equations are ambiguous because of the trigonometric function and the sign in front of the square root. The ambiguity in Eq. 7.7 can be resolved by taking into account that, generally, for a passive material, $n'' > 0$, $\varepsilon'' > 0$, $\mu'' > 0$ and $Z' > 0$, while the imaginary part n'' in Eq. 7.8 can be found using a similar condition as:

$$n'' = \pm\frac{1}{kh}\mathrm{Im}\left(\cos^{-1}\left(\frac{1-(S_{11})^2 + (S_{21}^0)^2}{2S_{21}^0}\right)\right). \quad (7.9a)$$

However, in this situation, the real part n' gives:

$$n' = \pm\frac{1}{kh}\mathrm{Re}\left(\cos^{-1}\left(\frac{1-(S_{11})^2 + (S_{21}^0)^2}{2S_{21}^0}\right)\right) + \frac{2\pi m}{kh}, \quad (7.9b)$$

where m is an arbitrary integer. The sign in Eq. 7.9b is chosen so that it is the same as in Eq. 7.9a. Finally, the integer m for cases of very thin slabs ($h \ll \lambda$) is assumed to be zero **[211]**, thus eliminating any remaining ambiguity. Then, the effective permittivity and permeability can be found from Eq. 7.3 and Eq. 7.4 respectively.

For a more general case, in which a slab is surrounded by a material other than a vacuum, Eq. 7.8, Eq. 7.9a and Eq. 7.9b are modified to **[212]**:

$$Z = \pm\sqrt{\frac{(1+S_{11})^2 - (S_{21}^0)^2}{n_1^2(1-S_{11})^2 - n_3^2(S_{21}^0)^2}} \quad (7.10)$$

$$n_{eff} = \pm\frac{1}{kh}\cos^{-1}\left(\frac{1}{S_{21}^0}\frac{n_1(1-(S_{11})^2) + n_3(S_{21}^0)^2}{n_1 + n_3 + S_{11}(n_3 - n_1)}\right), \quad (7.11)$$

where n_1 is the refractive index of the superstratum (the region from which the light is coming) and n_3 is the refractive index of the substrate (the region to which the light is transmitted through the slab). For the considered fishnet metamaterial, h becomes its total thickness, $n_1 \equiv n_{water} = 1.325$ and $n_3 \equiv n_{quartz} = 1.53$.

7.3.3 Effective refractive index of fishnet

Plots of the real and imaginary parts of the effective refractive index as a function of frequency are shown in Fig. 7.3. Variations in the gold/titanium thickness ratio in the upper layer are described by a filling factor *G* that changes from 0 to 1 as:

$$G = \frac{h_{Ti}}{h_{Ti} + h_{Au}}, \qquad (7.12)$$

where h_{Ti} is the thickness of the titanium absorptive layer and h_{Au} is that of the gold remaining in the top layer of the fishnet (which is the only layer with titanium in it as the other metallic layer is made of gold only). Note that the total thickness of the top metallic layer is kept constant at 50 nm and that the thicknesses of the bottom Au and dielectric TiO_2 layers are not changed (refer to Fig. 7.1 for details). The different filling factors in Fig. 7.3 are represented in the following way: ○ – G = 0 (50 nm of Au), □ – G = 0.35 (32.5 nm of Au, 17.5 nm of Ti), × – G = 0.7 (15 nm of Au, 35 nm of Ti) and + – G = 1 (50 nm of Ti), with only the points for the real parts of the refractive indices connected by continuous lines. As expected, due to weaker plasmonic excitation, the resonance gaps become shallower with increases in the titanium fraction and eventually disappear. The values of the effective refractive indices for low filling factors G = 0 and G = 0.35 are -0.6125 and -0.0854 respectively. As can be observed in Fig. 7.3 for G = 0.7 and G = 1, n_{eff} is positive for all wavelengths in the region of interest. The simulations show that the effective refractive indices become positive for G > 0.42, although those for G = 0.7 and G = 1 are not negative, they are used to illustrate the impact of higher contents of titanium on absorption.

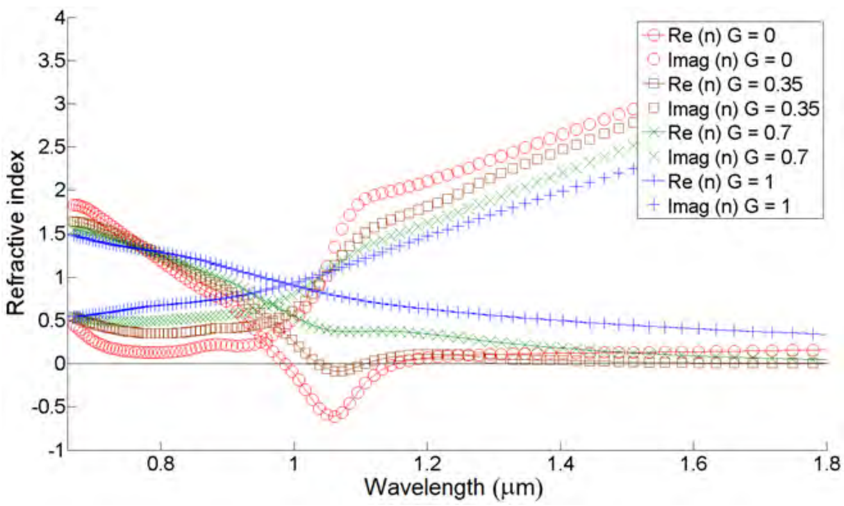

Fig. 7.3 – Extracted effective refractive indices

The fishnet structure is optimized to be a NIM at 1064 nm and to simultaneously have titanium in its upper absorptive layer. The dimensions of the metamaterial cell are summarized in Table 7.1 below.

Table 7.1 – Geometrical dimensions of metamaterial cell

Variable	Description	Value, nm
a	Length of cell	350
b	Width of cell	240
a_1	Length of gap	225
b_1	Width of gap	113
h_1	Thickness of upper Au layer	0-50
h_2	Thickness of TiO_2 layer	50
h_3	Thickness of lower Au layer	50
h_4	Total thickness	156

7.3.4 Absorption, transmission and reflection of fishnet

The fishnet's absorption A can be obtained from its transmission T and reflection R as $A = 1 - T - R$, with the frequency responses for absorption and reflection for the selected filling factors shown in Fig. 7.4a and Fig. 7.4b respectively. The resonant behaviour of the refractive indices results in the rise of absorption (Fig. 7.4a) as well as in the drop of reflectivity (Fig. 7.4b). For pure gold (G = 0), the absorption mainly occurs because of the NIM resonance, while the metamaterial with an incorporated titanium layer has a weaker electromagnetic resonance, and higher absorption is achieved because of the titanium itself (G = 1). Combinations of the metamaterial's resonance and material losses due to the titanium layer result in even higher absorption (G = 0.35, G = 0.7), as presented in Fig. 7.4a. It is also noted that, due to the differences in plasma frequencies of titanium and gold, the absorptive resonances red-shift and smooth with increasing filling factors.

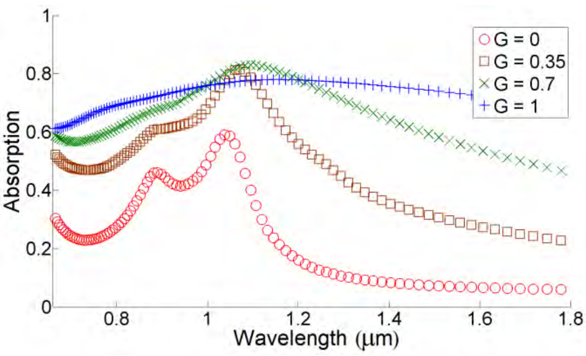

Fig. 7.4a – Absorption spectra for fishnet structure

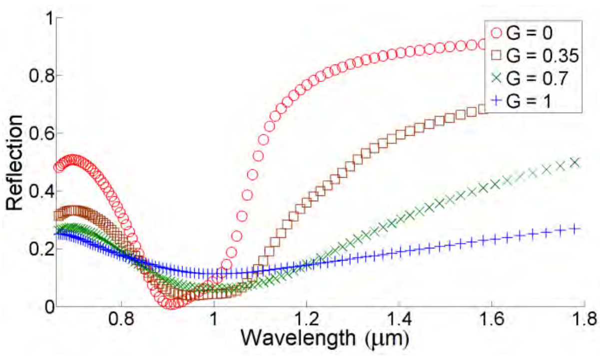

Fig. 7.4b – Reflection spectra for fishnet structure

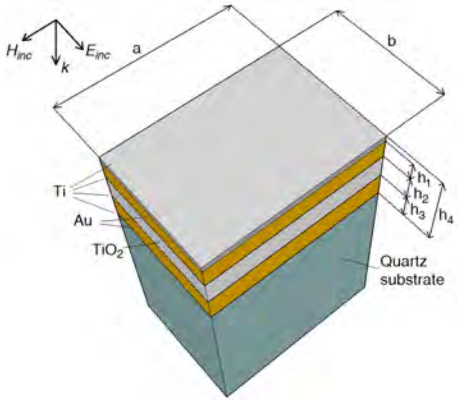

Fig. 7.5 – Layered metal-dielectric structure

The material's absorption can be studied by simulating a layered metal-dielectric structure that lacks a hole, but, otherwise, is identical to the considered metamaterial cell (Fig. 7.5). In such geometry, there is no resonance of the refractive index and all losses are caused by only the dispersive properties of the constituent materials. The absorption and reflection spectra for this case are plotted in Fig. 7.6a and Fig. 7.6b respectively, in which it can be seen that the absorption around 1064 nm gradually increases with higher filling factors and eventually reaches almost 52%.

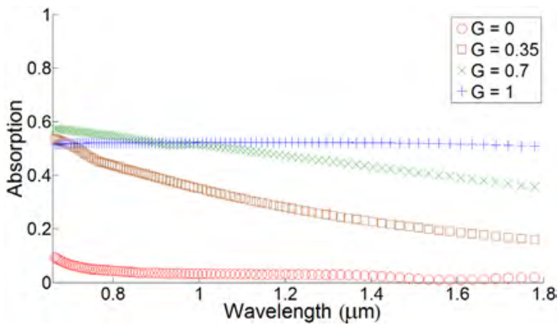

Fig. 7.6a – Absorption spectra for layered metal-dielectric structure

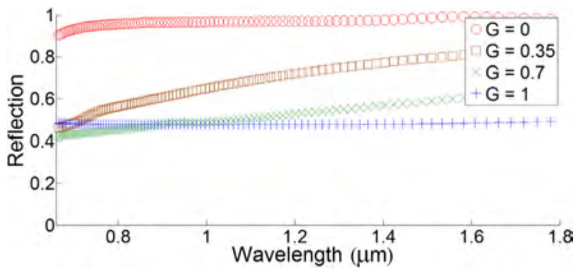

Fig. 7.6b – Reflection spectra for layered metal-dielectric structure

The calculated values of reflection, transmission and absorption (at 1064 nm) are presented in Table 7.2 for both the fishnet cells and layered metal-dielectric structures. For the metamaterial, the addition of titanium effectively increases the global absorption of the structure, but weakens its resonance. For the non-patterned multilayer structure, gold, as expected, acts as a good mirror, while titanium partially absorbs the incident radiation.

Table 7.2 – Simulated values of reflection, transmission and absorption at 1064 nm

	Fishnet structure			Layered metal-dielectric structure		
Filling factor	Reflection	Transmission	Absorption	Reflection	Transmission	Absorption
0	0.3345	0.1186	0.5469	0.9682	0	0.0318
0.35	0.0700	0.1166	0.8134	0.6738	0	0.3262
0.7	0.0689	0.1109	0.8202	0.4987	0	0.5013
1	0.1167	0.1114	0.7719	0.4775	0	0.5225

7.3.5 Thermal damage in metamaterials

In general, the damage of a material is associated with the absorbed fluence F of an incident light field **[19]**. For a CW laser with a spot-size d, exposure time T, incident power P and absorption A, the fluence is approximately equal to:

$$F = \frac{4TPA}{\pi d^2}. \tag{7.13}$$

Because of the limitations of the experimental setup, the measurements are restricted to exposing the samples to a fixed time of 2 minutes. Therefore, although real-time thermal damage assessment is not possible due to the constrained capabilities of the imaging system, it is feasible to make a brief qualitative estimation of the dealt damage after each subsequent exposure.

The underlying physics of material deformation resulting from laser-metal interactions can be explained using a combination of the elasto-plastic flow and two-temperature model (TTM) in a 2D approximation **[208]**. The elasto-plastic flow depicts the mechanical lattice deformation of the exposed surface, while the TTM describes the melting of the metal due to the incoming radiation being absorbed by electrons with the subsequent electron-phonon coupling.

Assuming a circular profile of the beam's spot, the coordinate system could be selected as cylindrical with a radial coordinate r, polar angle Θ, and axial coordinate z (along which the light is propagating). Then, according to TTM, the laser radiation absorption is written as **[208]**:

$$\left(C_l + \Delta H_m \delta(T - T_m)\right)\frac{\partial T_l}{\partial t} = g(T_e - T_l) \tag{7.14}$$

$$C_e \frac{\partial T_e}{\partial t} = \frac{\partial}{\partial z} K_e \frac{\partial T_e}{\partial z} + \frac{1}{r}\frac{\partial}{\partial r} r K_e \frac{\partial T_e}{\partial r} - g(T_e - T_l) + \Sigma(z, r, t), \tag{7.15}$$

where the subscripts l and e correspond to the lattice and electrons respectively; C_l and C_e are the lattice and electron heat capacities; the term with the δ-function takes into account interactions on the solid-liquid interface; g is the electron-lattice coupling coefficient; and K_e is the electron thermal conductivity **[213–215]**.

The dynamic elasticity for a cylindrical symmetry along the z-axis is expressed as **[21, 216]**:

$$\frac{\partial \sigma_{rr}}{\partial r} + \frac{\partial \sigma_{rz}}{\partial z} + \frac{\sigma_{rr} - \sigma_{\theta\theta}}{r} = \rho \frac{\partial^2 u}{\partial t^2} \qquad (7.16)$$

$$\frac{\partial \sigma_{rz}}{\partial r} + \frac{\partial \sigma_{zz}}{\partial z} + \frac{\sigma_{rz}}{r} = \rho \frac{\partial^2 w}{\partial t^2} \qquad (7.17)$$

$$\sigma_{zz} = \lambda div(D) + 2\mu \frac{\partial w}{\partial z} \qquad (7.18)$$

$$\sigma_{rr} = \lambda div(D) + 2\mu \frac{\partial u}{\partial r} \qquad (7.19)$$

$$\sigma_{\theta\theta} = \lambda div(D) + 2\mu \frac{u}{r} \qquad (7.20)$$

$$\sigma_{rz} = \mu \left(\frac{\partial u}{\partial z} + \frac{\partial w}{\partial r} \right), \qquad (7.21)$$

where σ_{rr}, σ_{rz}, σ_{rr} and $\sigma_{\Theta\Theta}$ are the components of the stress tensor; ρ is the medium's mass density; and D is the displacement vector with components u and w. The Young's modulus E and Poisson ratio v are connected to the Lamé parameters λ and μ as:

$$\lambda = \frac{E\nu}{(1+\nu)(1-2\nu)} \qquad (7.22)$$

$$\mu = \frac{E}{2(1+\nu)}. \qquad (7.23)$$

Finally, the plastic yielding can be found from Eq. 7.16-7.23 by taking into account the von Mises yield criterion in terms of the stress deviator **[208, 217]** as:

$$K = 2J - \frac{2}{3}(Y^0)^2 \quad (7.24)$$

$$2J = (S_{rr}^2 + S_{zz}^2 + S_{\theta\theta}^2) + 2\sigma_{rz}^2 \, . \quad (7.25)$$

Here Y^0 is the yield stress and S_{rr}, S_{zz} and $S_{\Theta\Theta}$ are the components of the stress deviator tensor. Further details of thermal modelling as well as a discussion of the types of materials best suited for microbump and nanojet formation can be found in **[218]**.

The deformation process is schematically visualized in Figs. 7.7a-7.7c. During exposure, the laser radiation impinges at a normal incidence to the studied sample (Fig. 7.7a) and, as a result of electron-phonon coupling, the metallic layer exhibits momentum normal to the surface. While at least some part of the layer remains solid, this momentum is compensated by the work of plastic deformations, which lead to the formation of a microbump or nanojet on top of the samples (Fig. 7.7b and Fig. 7.7c respectively). Eventually, with increases in the fluence, the metallic layer's momentum exceeds the surface tension forces (for the liquid phase), as well as the work of plastic deformations (for the solid phase), and produces nanojet burst.

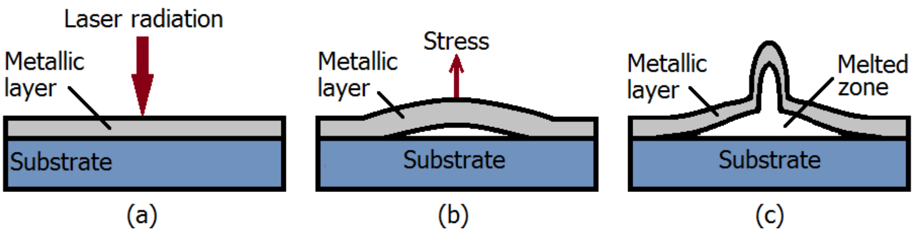

Fig. 7.7 – (a) Unexposed structure. (b) Microbump formation. (c) Nanojet formation

Qualitatively, the temperature distribution inside a metamaterial cell is shown in Fig. 7.8 for incident laser powers not reaching the threshold melting value (i.e., while no thermal damage occurs). It is seen that most of the heat accumulates in the top metallic layer, and, similar to a nano-antenna (considered in Chapter 5), is not efficiently dissipated by the surrounding air or quartz substrate.

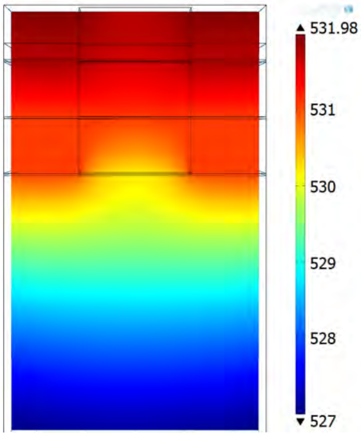

Fig. 7.8 – Qualitative temperature distribution in fishnet metamaterial for non-destructive power regime (temperature is given in °C)

Several factors influence the formation of microbumps, such as the melting temperature, Young's modulus and coefficient of linear thermal expansion **[218]**. As low values of these parameters correspond to small potential mechanical energy, lesser amounts of laser radiation are required to overcome the work of plastic deformations **[208]**. On the other hand, the material's plasticity should remain high to prevent premature bursts. Based on the material properties given in **[219]**, titanium can potentially form microbumps during irradiation and gold nanojets have been already experimentally demonstrated in **[219, 220]**.

7.4 Experimental results

7.4.1 Fishnet fabrication

All samples are fabricated on top of standard quartz substrates, with their metallic and dielectric parts deposited using EBE and Sputter systems respectively. The thicknesses of the materials are given in Table 7.1 and the selected filling factors are G = 0, G = 0.35, G = 0.7 and G = 1. The fishnet holes are milled using the FEI Helios NanoLab 600 dual-beam FIB system at a low current of 9.7 pA to prevent any undesirable damage to the structure (see Chapter 4 (Section 4.3.2) for more details).

Each sample has 3 fishnet arrays patterned on it, with every array occupying an area of 300 μm^2. SEM images of the metamaterial's surface at different magnifications are shown in Fig. 7.9a and Fig. 7.9b. The patterns are placed 100 μm away from each other allowing them to be exposed individually during the experiments. Every metamaterial array consists of 3920 elements, which prevents any local inhomogeneities or fabrication flaws affecting the overall performance of the structure.

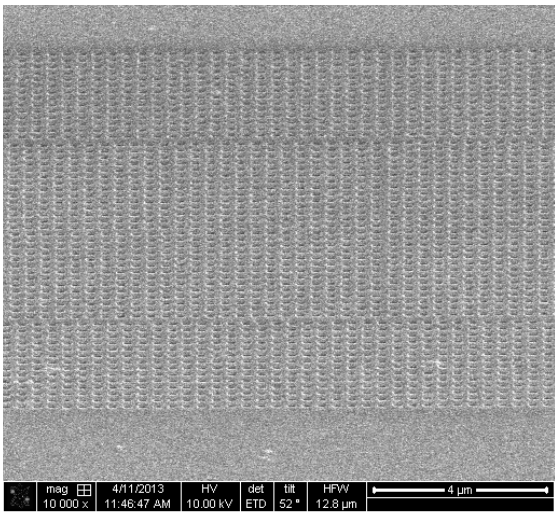

Fig. 7.9a – Fabricated fishnet
(magnification 10000×)

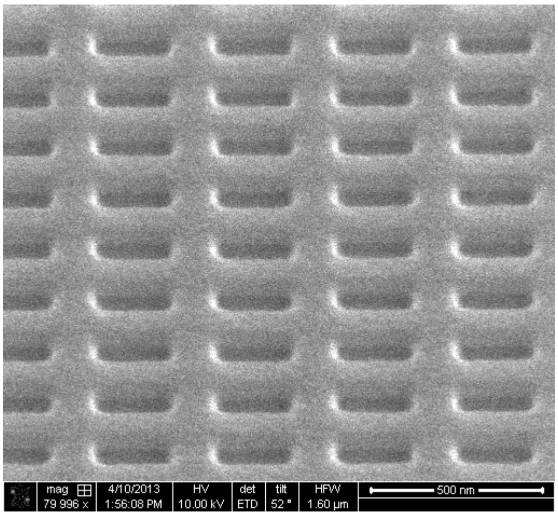

Fig. 7.9b – Fabricated fishnet
(magnification 80000×)

7.4.2 Overview of experimental setup

A schematic of the experimental setup is shown in Fig. 7.10. The 1064 nm CW Nd:YAG (Laser Quantum, IR Ventus) laser is focused down to a diffraction-limited spot using a microscope's objective lens (Nikon CFI Plan Achromat 100x), which is achieved by expanding the laser to slightly over-fill the back aperture of the lens. A spatial light modulator (SLM) (Hamamatsu, LCOS) is also pre-configured to minimize aberrations at the laser's focus. With these arrangements, a spot size of 0.8 µm is achieved at the laser's focus (it is assumed that the laser has a Gaussian profile and the spot's diameter is defined by containing 95% of the total beam power). The power at the laser's focus is controlled using a polarizing beam splitter together with a half-wave plate and, taking all optical losses into account, a maximum incident power of 140 mW is achieved.

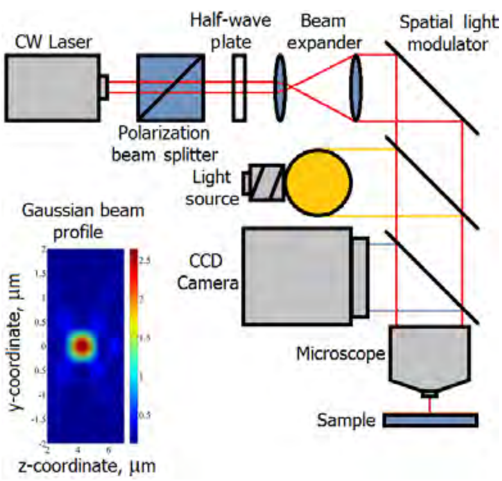

Fig. 7.10 – Experimental setup. Inset – laser spot profile

The substrates with nanostructure arrays are mounted on top of a glass slide and covered with Type-0 cover slips, with a thin film of water (20 μm) between them for refractive index matching. A CCD camera is used to image the surface of the substrate and locate the nanostructure arrays which, once found, are illuminated at a fixed laser power for 2 minutes. In subsequent experiments, the laser's power is gradually increased in steps of 15 mW. After each exposure, the laser spot is moved to a new position of the patterned area to ensure that damage won't accumulate in one point. Between experiments, the structures are first visually inspected via the CCD camera for macroscopic signs of microbump or nanojet formations.

7.4.3 Assessing thermal damage using SEM

The conducted experiments are focused on studying the dependence of damaging laser power on the Au/Ti ratio in the top layer (i.e., on sample absorption). It is observed that thermal damage of metamaterials occurs at the incident powers of: $P_0 = 88$ mW, $P_{0.35} = 53$ mW, $P_{0.7} = 45$ mW and $P_1 = 60$ mW, where the index corresponds to the filling factor *G*. Based on this data, the absorbed damaging power is determined by multiplying the incident damaging power (given in mW) by the absorption (calculated from numerical simulations). The final results for the considered filling factors are summarized in Table 7.3.

Table 7.3 – Summarized results

Filling factor	Calculated Reflection	Calculated Transmission	Calculated Absorption	Incident damaging power, mW	Absorbed damaging power, mW
0	0.3345	0.1186	0.5469	88	48.1272
0.35	0.0700	0.1166	0.8134	53	43.1102
0.7	0.0689	0.1109	0.8202	45	36.9090
1	0.1167	0.1114	0.7719	60	46.3140

All samples show good agreement with our expectations as SEM images of the exposed surface demonstrate significant thermal damage proportional to the illumination power, with a microbump's formation process clearly observed in Figs. 7.11a-d. When the laser power exceeds the threshold value, the underlying gold layer starts melting and deforming the titanium film above (Fig. 7.11a). As the power is increased from 60 mW to 90 mW, the affected area grows nearly 6 times (Fig. 7.11b). The laser exposure to the maximum power of 140 mW results in the formation of a microbump with a diameter of 1.5 μm (Fig. 7.11c), the burst of which is presented in Fig. 7.11d. During illumination, the underlying gold layer forms an unstable microbump and eventually blows the titanium film above, warping both materials and leaving traces of the melted metals around the exposed spot. The high-magnification SEM images of the exposed surface also show rectangular holes tending to form more rounded shapes close to the melting regions, which can be attributed to surface tension effects.

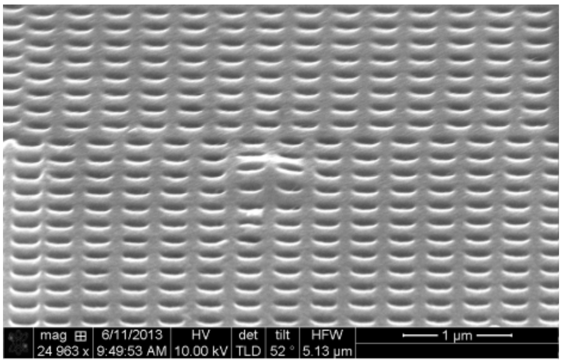

Fig. 7.11a – Microbump formation, power 60 mW, G = 0.35

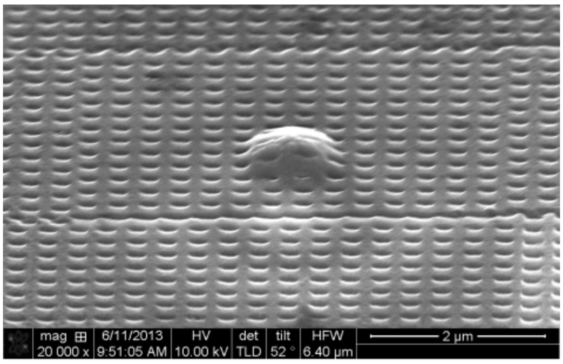

Fig. 7.11b – Microbump formation, power 90 mW, G = 0.35

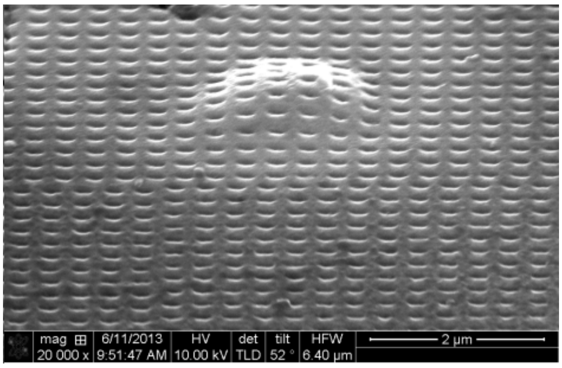

Fig. 7.11c – Microbump formation, power 140 mW, G = 0.35

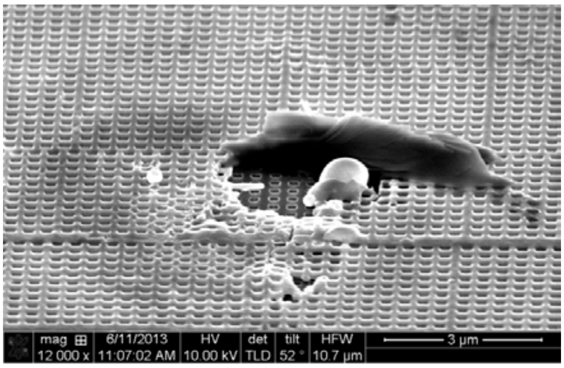

Fig. 7.11d– Microbump burst, power 140 mW, G = 0.7

As an additional reference, an unpatterned area away from the metamaterial array is exposed using the same illumination conditions, which also results in similar surface deformations, with a microbump with a nanojet on top clearly observed in Fig. 7.12. Due to lower absorption of the metallic layers, the incident power has to be increased above 90 mW, but as, in this region, the laser does not operate stably, and it is very difficult to find the exact damaging thresholds. However, the order, in which the samples melt, remains correct and specimens with higher fractions of gold require significantly larger incident powers. With a maximum possible incident power of 140 mW, all samples eventually display signs of thermal damage (Fig. 7.12). It is estimated that the absorbed damaging power for titanium is more than 70 mW and that for gold is greater than 4 mW.

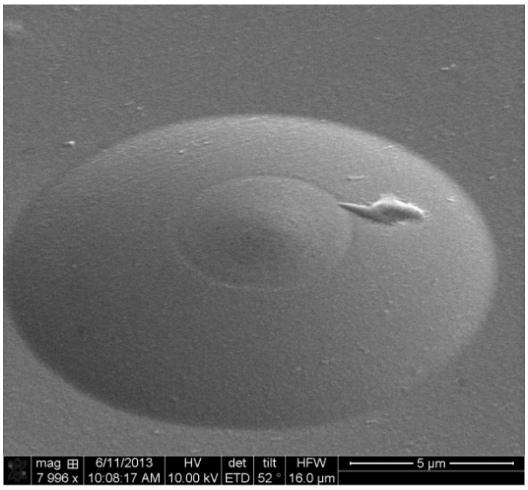

Fig. 7.12 – Microbump with nanojet formation

7.5 Summary

In this chapter, the impact of a titanium layer on the absorption of a conventional fishnet structure is analyzed. Initially, NIM metamaterials are theoretically modelled and their absorption spectra are calculated for samples with different titanium filling factors for both fishnet and multilayer MDM structures. From qualitative thermal simulations, it is found that heat mainly accumulates in the top fishnet layer and is not dissipated into the ambient area. During the experiments, each fishnet metamaterial is exposed to a 1064 nm CW Nd:YAG laser for a duration of 2 minutes and then thermal damage is assessed from SEM images. It is shown that the combination of titanium and gold increases the total absorption of the metamaterials to nearly 82% and leads to a reduction in the damage threshold power to 45 mW (51% of the original incident damaging power and 77% of the original absorbed damage threshold power). It is also found that the melting process results in the formation of microbumps in the top fishnet layer, which arise because the gold underlayer melts and leads to a mechanical deformation of the solid titanium film above.

Possible applications of such metamaterials with enhanced absorption could be as sensors or thermal fuses in optical circuits. While being transparent around the resonant frequency at low powers, they melt and block the light's path after the laser radiation exceeds a certain threshold. Although the fishnet metamaterial considered here is not a thermally resistive structure as are those discussed in previous chapters, it still can be seen as a high-power device assuming that it is deliberately fabricated to melt under intense laser radiation in order to act as a fuse (however this could be an expensive solution, which strongly depends on a particular application).

This section concludes the study of high-power plasmonic devices, which covered nano-antennas (Chapter 5), metamaterial slot waveguides (Chapter 6) and fishnet metamaterials (Chapter 7). A summary of all the obtained results as well as suggestions for future work are given further in Chapter 8.

Chapter 8 – Summary of the conducted research

8.1 Introduction

The final chapter summarizes all the research activities undertaken during my PhD. The discussion begins by briefly outlining the high-power plasmonic devices described in previous sections (i.e., dipole nano-antenna, metamaterial slot waveguide and fishnet metamaterial) and then provides some suggestions for future work.

8.2 Summary of research results

The interaction between electromagnetic radiation and an exposed nano-structure is a complex problem, which often results in the incident light properties (polarization, phase, wave vector, etc.) being modified through excitations of SPPs and LSPs. These resonant plasmonic quasi-particles arise at the conductor-insulator interfaces and, because of the metal's lossy nature, their electromagnetic energy becomes transformed into heat over time, which can lead to thermal deformations of the illuminated nano-patterns.

The present work studies the performances of plasmonic devices (dipole nano-antennas, metamaterial-based slot waveguides and fishnet metamaterials) that are driven by infrared radiation. Their optical properties are numerically analyzed using the FDTD software and the heat distributions are estimated by the FEM package. Also, some of structures are fabricated using EBE and FIB systems, and their thermal resistances are experimentally tested through exposure to powerful laser sources. The obtained results demonstrate the capability of the proposed designs to operate in high-power regimes, which implies that they have either high thermal damage thresholds (i.e., expanded operating ranges) or strong temperature sensitivity (that is useful for sensing applications). More explicitly, the following conclusions are drawn:

1) Dipole titanium nano-antennas are able to withstand considerably higher incident fluences and, thereby, support stronger electric fields than their gold counterparts. While plasmonic losses in a titanium-based structure lower its electric field enhancement factor by, on average, 19%, this is compensated by the higher melting temperature of titanium, which means that there is a possibility of achieving even stronger electric fields by simply increasing the intensity of the driving laser radiation. Quantitatively, the experiments show that titanium nano-antennas are able

to endure 18 dB greater incident power densities and, thus, handle 7 times higher electric fields than gold structures of the same dimensions, which makes the proposed design suitable for many applications, including SERS, nano-particle detection and nonlinear optics.

2) The silica-filled slot waveguide with lateral slab regions formed by multilayered metamaterials is not only capable of operating in a high-power regime, but also has optical properties superior to those of conventional pure dielectric or metallic slot waveguides. If the silver/silicon thickness ratio in these lateral regions is equal to 15 nm/10 nm, the electric field confinement improves dramatically, becoming 99% tighter (in terms of the normalized field values inside the slot) than that in an insulator-only device. Simultaneously, propagation losses are also reduced by 3.5 times compared with those of a pure metallic slot waveguide of similar size. The proposed geometry can find further application as an integrated component in short-distance infrared interconnects, modulators, switches, couplers and other plasmonic devices.

3) The additional titanium layer placed on top of a conventional Au-TiO_2-Au fishnet structure significantly increases the total absorption of the metamaterial because of the combination of losses introduced by its constituent materials and LSP excitations around its resonant frequency. The higher fractions of titanium enhance only the material absorption but, at the same time, weaken the impact of NIM resonance. For a metamaterial with a Ti/Au ratio in the upper layer of 35 nm/15 nm, the overall absorption rises to nearly 82%, which leads to a reduction in the incident damaging power of almost 49% (from 88 mW to 45 mW). The experimental measurements verify the simulation predictions and also show the distinctive thermal deformations of the exposed surfaces, which are attributed to the ablation processes in the gold underlayers. Such metamaterials with enhanced absorption may find application in temperature sensors or thermal fuses integrated in optical circuits.

8.3 Suggestions for future work

While a significant amount of research was performed to characterize the high-power plasmonic devices described in this thesis, some parts of the presented work could be further improved as follows:

1) Fabricating a metamaterial silica-filled slot waveguide and subsequently studying it using a near-field scanning optical microscope (NSOM) in order to experimentally measure the field confinement inside the slot (realistically, this will imply selecting wider slots than ones considered in the theoretical work). Another experiment could involve coupling a proposed waveguide to a high-power source and measuring its thermal resistance.
2) Performing thermal simulations in a more rigid form by utilizing the heat coefficients corresponding to the nano-scale material (rather than implementing bulk values) and using the characteristics of the more stable laser sources (i.e., those which have a reasonably low jitter of the generated light parameters). This will help to find a quantitative temperature distribution inside exposed nano-devices.
3) Applying TTM and elasto-plastic flow approaches to nano-antennas and slot waveguides to explicitly model their processes of thermal deformation; however this will require a major study in mechanical engineering.
4) Investigating other plasmonic devices, such as metamaterial absorbers or heat emitters, and studying the heat dissipation processes in a plasmonic circuit consisting of multiple high-power elements coupled together in order to gain a better insight into the underlying physical mechanisms.

Bibliography

[1] W. Koechner, “Solid State Laser Engineering”, *New York: Springer-Verlag* (1976)

[2] Y. F. Chen, *et al*., “A diode-pumped high power Q-switched and self-mode-locked Nd:YVO_4 laser with a LiF:F^-_2 saturable absorber”, *Applied Physics B,* vol. 73, pp. 115–118 (2001)

[3] M. T. Asaki, *et al*., “Generation of 11-fs pulses from a self-mode-locked Ti:sapphire laser”, *Optics Letters*, vol. 18, issue 12, pp. 977–979 (1993)

[4] S. Nolte, *et al*., “Ablation of metals by ultrashort laser pulses”, *Journal of the Optical Society of America B*, vol. 14, issue 10, pp. 2716–2722 (1997)

[5] A. Semerok, and C. Dutouquet, “Ultrashort double pulse laser ablation of metals”, *Thin Solid Films (Proceedings of Symposium H on Photonic Processing of Surfaces, Thin Films and Devices, of the E-MRS 2003 Spring Conference)*, vol. 453–454, pp. 501–505 (2004)

[6] F. Bozon-Verduraz, *et al*., “Production of nanoparticles by laser-induced ablation of metals in liquids”, *Quantum Electronics*, vol. 33, issue 8, pp. 714–720 (2003)

[7] A. Mele, *et al*., “Laser ablation of metals: Analysis of surface-heating and plume-expansion experiments”, *Applied Surface Science*, vol. 109–110, pp. 584–590 (1997)

[8] P. N. Prasad and D. J. Williams, “Introduction to nonlinear optical effects in molecules and polymers”, *New York: John Wiley & Sons, Inc.* (1991)

[9] P. J. Campagnola and Leslie M Loew, “Second-harmonic imaging microscopy for visualizing biomolecular arrays in cells, tissues and organisms”, *Nature Biotechnology*, vol. 21, issue 11, pp. 1356–1360 (2003)

[10] N. J. Borys, *et al*., “Intermittency in second-harmonic radiation from plasmonic hot spots on rough silver films”, *Physical Review B*, vol. 80, pp. 161407(R) (2009)

[11] T. H. Maiman, “Stimulated optical radiation in ruby”, *Nature*, vol. 187, issue 4736, pp. 493–494 (1960)

[12] N. Seto, *et al*., “High-speed simultaneous observation of plasma and keyhole behaviour during high power CO_2 laser welding: Effect of shielding gas on porosity formation”, *Journal of Laser Applications*, vol. 12, issue 6, pp. 245–250 (2000)

[13] W. Yuen, *et al*., “High-performance 1.6 µm single-epitaxy top-emitting VCSEL”, *Electronics Letters*, vol. 36, issue 13, pp. 1121–1123 (2000)

[14] D. J. Richardson, *et al*., “High power fiber lasers: current status and future perspectives”, *Journal of the Optical Society of America B*, vol. 27, issue 11, pp. B63–92 (2010)

[15] S. V. Chernikov, *et al*., “Supercontinuum self-Q-switched ytterbium fiber laser”, *Optics Letters*, vol. 22, issue 5, pp. 298–300 (1997)

[16] B. Braun, *et al*., “56-ps passively Q-switched diode-pumped microchip laser”, *Optics Letters*, vol. 22, issue 6, pp. 381–383 (1997)

[17] D. E. Spence, *et al*., “60-fsec pulse generation from a self-mode-locked Ti: sapphire laser”, *Optics Letters*, vol. 16, issue 1, pp. 42–44 (1991)

[18] Australian/New Zealand Standard AS/NZS 2211.1: 2004 – Safety of laser products (2004)

[19] H. Sobral and M. Villagrán-Muniz, “Energy balance in laser ablation of metal targets”, *Journal of Applied Physics*, vol. 98, pp. 083305 (2005)

[20] N. M. Bulgakova and I. M. Bourakov, “Phase explosion under ultrashort pulsed laser ablation: modeling with analysis of metastable state of melt”, *Applied Surface Science*, vol. 197–198, pp. 41–44 (2002)

[21] L. D. Landau and E. M. Lifshitz, “Theory of Elasticity. Vol. 7” (3rd Ed.), *Butterworth-Heinemann* (1986)

[22] C. Kittel and H. Kroemer, “Thermal Physics” (2nd Ed.), W. H. Freeman and Company (1980)

[23] D. V. Sivukhin, “General physics course. Volume 2: Thermodynamics and molecular physics” (in Russian), *Moscow: Nauka*, ISBN: 5020141879 (1990)

[24] J. Hao, *et al*., “Nearly total absorption of light and heat generation by plasmonic metamaterials”, *Physical Review B*, vol. 83, pp. 165107 (2011)

[25] C. Kittel, “Introduction to solid state physics” (8th Ed), *John Wiley & Sons, Inc.*, Hoboken (2005)

[26] M. L. Juan, *et al*., “Plasmon nano-optical tweezers”, *Nature photonics*, vol. 5, pp. 349–356 (2011)

[27] L. Cognet, *et al*, “Single metallic nanoparticle imaging for protein detection in cells”, *Proceedings of the National Academy of Sciences of the United States of America*, vol. 100, issue 20, pp. 11350–11355 (2003)

[28] X. Montet, *et al*, “Nanoparticle Imaging of Integrins on Tumor Cells”, *Neoplasia*, vol. 8, issue 3, pp. 214–222 (2006)

[29] L. R. Hirsch, *et al*., “Nanoshell-mediated near-infrared thermal therapy of tumors under magnetic resonance guidance”, *Proceedings of the National Academy of Sciences of the United States of America*, vol. 100, issue 23, pp. 13549–13554 (2003)

[30] L. C. Kennedy, *et al*, “A New Era for Cancer Treatment: Gold-Nanoparticle-Mediated Thermal Therapies”, *Small*, vol. 7, issue 2, pp. 169–183 (2011)

[31] H. C. Van de Hulst, “Light Scattering by Small Particles”, *New York: John Wiley & Sons, Inc.*, (1957)

[32] P. K. Jain, *et al*., “Calculated Absorption and Scattering Properties of Gold Nanoparticles of Different Size, Shape, and Composition: Applications in Biological Imaging and Biomedicine”, *Journal of Physical Chemistry B*, vol. 110, pp. 7238–7248 (2006)

[33] G. Baffou, *et al*., “Influence of morphology”, *Applied Physics Lett*ers, vol. 94, pp. 153109 (2009)

[34] D. L. Huffaker, *et al.*, “1.3 μm room-temperature GaAs-based quantum-dot laser”, *Applied Physics Lett*ers, vol. 73, issue 18, pp. 2564–2566 (1998)

[35] O. B. Shchekin and D. G. Deppe, “1.3 μm InAs quantum dot laser with T_0=161 K from 0 to 80 °C”, *Applied Physics Lett*ers, vol. 80, issue 18, pp. 3277–3279 (2002)

[36] F. Koyama, “Recent Advances of VCSEL Photonics”, *IEEE Journal of Lightwave Technology*, vol. 24, issue 12, pp. 4502–4512 (2006)

[37] Y. Arakawa and H. Sakaki, “Multidimensional quantum well laser and temperature dependence of its threshold current”, *Applied Physics Lett*ers, vol. 40, issue 11, pp. 939–941 (1982)

[38] S. Nagahama, *et al.*, “High-Power and Long-Lifetime InGaN Multi-Quantum-Well Laser Diodes Grown on Low-Dislocation-Density GaN Substrates”, *Japan Journal of Applied Physics*, vol. 39, pp. L647–L650 (2000)

[39] D. Punj, *et al.*, “A plasmonic ‘antenna-in-box’ platform for enhanced single-molecule analysis at micromolar concentrations”, *Nature Nanotechnology*, vol. 8, pp. 512–516 (2013)

[40] P. Chen and A. Alù, “Subwavelength Imaging Using Phase-Conjugating Nonlinear Nanoantenna Arrays”, *Nano Letters*, vol. 11, pp. 5514–5518 (2011)

[41] W. Zhang, *et al.*, “Trapping and Sensing 10 nm Metal Nanoparticles Using Plasmonic Dipole Antennas”, *Nano Letters*, vol. 10, pp. 1006–1011 (2010)

[42] A. E. Krasnok, *et al.*, “Optical nanoantennas”, *Physics-Uspekhi*, vol. 56, issue 6, pp. 539–564 (2013)

[43] H. T. Hattori, *et al.*, “Coupling of light from microdisk lasers into plasmonic nano-antennas”, *Optics Express*, vol. 17, issue 23, pp. 20878–20884 (2009)

[44] H. T. Hattori, *et al.*, “Driving plasmonic nanoantennas with triangular lasers and slot waveguides”, *Applied Optics*, vol. 50, issue 16, pp. 2391–2400 (2011)

[45] W. Nomura, *et al.*, “Nanodot coupler with a surface plasmon polariton condenser for optical far/near-field conversion”, *Applied Physics Letters*, vol. 86, pp. 181108 (2005)

[46] A. Alù and N. Engheta, “Tuning the scattering response of optical nanoantennas with nanocircuit loads”, *Nature Photonics*, vol. 2, pp. 307–310 (2008)

[47] S. A. Maier, *et al.*, “Observation of coupled plasmon-polariton modes in Au nanoparticle chain waveguides of different lengths: Estimation of waveguide loss”, *Applied Physic Letters*, vol. 81, issue 9, pp. 1714–1716 (2002)

[48] T. D. Visser, *et al.*, “Modal analysis of a planar waveguide with gain and losses”, *IEEE Journal of Quantum Electronics*, vol. 31, issue 10, pp. 1803–1810 (1995)

[49] W. Cai and V. Shalaev, “Optical Metamaterials: Fundamentals and Applications”, *New York: Springer* (2010)

[50] Y. Guo and Z. Jacob, “Thermal hyperbolic metamaterials”, *Optics Express*, vol. 21, issue 12, pp. 15014–15019 (2013)

[51] J. Hao, *et al.*, “High performance optical absorber based on a plasmonic metamaterial”, *Applied Physics Letters*, vol. 96, pp. 251104 (2010)

[52] H. Tao, *et al.*, “Highly flexible wide angle of incidence terahertz metamaterial absorber: Design, fabrication, and characterization”, *Physical Review B*, vol. 78, pp. 241103(R) (2008)

[53] X. Liu, *et al.*, “Infrared Spatial and Frequency Selective Metamaterial with Near-Unity Absorbance”, *Physical Review Letters*, vol. 104, pp. 207403 (2010)

[54] S. Molesky, *et al.*, “High temperature epsilon-near-zero and epsilon-near-pole metamaterial emitters for thermophotovoltaics”, *Optics Express*, vol. 21, issue S1, pp. A96–A110 (2013)

[55] C. Fu, *et al.*, “Thermal radiative properties of metamaterials and other nanostructured materials: A review”, *Frontiers of Energy and Power Engineering in China*, vol. 3, issue 1, pp. 11–26 (2009)

[56] S. A. Maier, “Plasmonics: fundamentals and applications”, *New York: Springer* (2007)

[57] L. D. Landau and E. M. Lifshitz, “The Classical Theory of Fields. Vol. 2” (4th Ed.), *Butterworth-Heinemann* (1975)

[58] A. Sommerfeld “Über die Fortpflanzung electrodynamischer Wellen längs eines Drahtes”, *Annalen der Physik und der physikalischen Chemie*, vol. 67, pp. 233–290 (1899)

[59] A. Hessel and A. A. Oliner, “A New Theory of Wood’s Anomalies on Optical Gratings”, *Applied Optics*, vol. 4, issue 10, pp. 1275–1297 (1965)

[60] R. H. Ritchie, *et al.*, “Surface-plasmon resonance effect in grating diffraction”, *Physical Review Letters*, vol. 21, issue 22, pp. 1530–1533 (1968)

[61] E. Kretschmann and H. Raether, “Radiative decay of non-radiative surface plasmons excited by light”, *Zeitschrift für naturforschung*, vol. 23A, pp. 2135–2136 (1968)

[62] P. B. Johnson and R. W. Christy, “Optical Constants of the Noble Metals”, *Physical Review B*, vol. 6, pp. 4370–4379 (1972)

[63] M. P. Nezhad, *et al.*, “Gain assisted propagation of surface plasmon polaritons on planar metallic waveguides”, *Optics Express*, vol. 12, issue 17, pp. 4072–4079 (2004)

[64] J. Homola, *et al.*, “Surface plasmon resonance sensors: review”, *Sensors and Actuators B*, vol. 54, pp. 3–15 (1999)

[65] J. G. Rivas, *et al.*, “Propagation of Surface Plasmon Polaritons on Semiconductor Gratings”, *Physical Review Letters*, vol. 93, pp. 256804 (2004)

[66] W. L. Barnes, *et al.*, “Surface plasmon subwavelength optics”, *Nature*, vol. 424, pp. 824–830 (2003)

[67] E. Ozbay, “Plasmonics: Merging Photonics and Electronics at Nanoscale Dimensions”, *Science*, vol. 311, pp. 189–193 (2006)

[68] A. Boltasseva, *et al.*, “Integrated Optical Components Utilizing Long-Range Surface Plasmon Polaritons”, *IEEE Journal of Lightwave Technology*, vol. 23, issue 1, pp. 413–422 (2005)

[69] C. F. Bohren and D. R. Huffman, "Absorption and scattering of light by small particles" (1st Ed.), *New York: John Wiley & Sons, Inc.* (1983)

[70] H. L. Gao, *et al*., "Efficiency enhancement of polymer solar cells by localized surface plasmon of Au nanoparticles", *Journal of Applied Physics*, vol. 114, pp. 163102 (2013)

[71] K. Nakayama, *et al*., "Plasmonic nanoparticle enhanced light absorption in GaAs solar cells", *Applied Physics Letters*, vol. 93, pp. 121904 (2008)

[72] S. A. Maier, *et al*., "Local detection of electromagnetic energy transport below the diffraction limit in metal nanoparticle plasmon waveguides", *Nature Materials*, vol. 2, pp. 229–232 (2003)

[73] M. Gu, *et al*., "Enhancing the Reception of Propagating Surface Plasmons Using a Nanoantenna", *IEEE Photonics Technology Letters*, vol. 22, no. 4, pp. 245–247 (2010)

[74] P. Biagioni, *et al*., "Nanoantennas for visible and infrared radiation", *Reports on Progress in Physics*, vol. 75, 024402 (2012)

[75] A. Kinkhabwala, *et al*., "Large single-molecule fluorescence enhancements produced by a bowtie nanoantenna", *Nature Photonics*, vol. 3, pp. 654–657 (2010)

[76] I. S. Maksymov, *et al*., "Optical Yagi-Uda nanoantennas", *Nanophotonics*, vol. 1, pp. 65–81 (2012)

[77] E. Mironov, *et al*., "Enhancing Weak Optical Signals by Using a Plasmonic Yagi-Uda Nano-antenna Array", *Photonics Technology Letters*, vol. 26, issue 22, pp. 2236-2239 (2014)

[78] Y. Zhang, *et al*., "Asymmetric fishnet metamaterials with strong optical activity", *Optics Express*, vol. 20, issue 10, pp. 10776–10787 (2012)

[79] T. Okamoto, *et al*., "Visible near-infrared light scattering of single silver split-ring structure made by nanosphere lithography", *Optics Express*, vol. 19, issue 8, pp. 7068–7076 (2011)

[80] M. Futamata, *et al*., "Microscopic morphology and SERS activity of Ag colloidal particles", *Vibrational Spectroscopy (Conference)*, vol. 30, issue 1, pp. 17–23 (2002)

[81] Z. Li, *et al*., "Charnia-like broadband plasmonic nano-antenna", *Journal of Modern Optics*, vol. 60, issue 10, pp. 790–796 (2013)

[82] D. J. Griffiths, "Introduction to Electrodynamics" (3rd Ed.), *Pearson Education*, *Dorling Kindersley* (2007)

[83] J. D. Jackson, "Classical Electrodynamics" (3rd Ed.), *New York: John Wiley & Sons, Inc.* (1999)

[84] G. Baffou, *et al*., "Mapping Heat Origin in Plasmonic Structures", *Physical Review Letters*, vol. 104, pp. 136805 (2010)

[85] A. O. Govorov and H. H. Richardson, "Generating Heat with Metal Nanoparticles", *Nano Today*, vol. 2, pp. 30–38 (2007)

[86] K. Yee, “Numerical solution of initial boundary value problems involving Maxwell’s equations in isotropic media”, *IEEE Transactions on Antennas and Propagation*, vol. 14, pp. 302–307 (1966)

[87] A. Taflove and S. C. Hagness, “Computational electrodynamics: the finite-difference time-domain method”, *Norwood: Artech House* (2000)

[88] R. M. Joseph, A. Taflove, “FDTD Maxwell’s Equations Models for Nonlinear Electrodynamics and Optics”, *IEEE Transactions on antennas and propagation*, vol. 45, issue 3, pp. 364–374 (1997)

[89] R. Courant, *et al*., “On the partial difference equations of mathematical physics” (translated from German), *IBM Journal of Research and Development*, vol. 11, issue 2, pp. 215–234 (1967)

[90] Information on FullWAVE 8.3 RSoft design group 2011 is available at: http://www.rsoftdesign.com (extracted on 24/11/2014)

[91] Information on MATLAB 7.8.0 (R2009a) is available at: http://www.mathworks.com.au/ (extracted on 24/11/2014)

[92] Information on COMSOL 4.0 Multiphysics 2012 is available at: http://www.comsol.com (extracted on 24/11/2014)

[93] A. F. Renteria, *et al*., “Effect of morphology on thermal conductivity of EB-PVD PYSZ TBCs”, *Surface and Coatings Technology*, vol. 201, issue 6, pp. 2611–2620 (2006)

[94] A. Majumdar, “Microscale Heat Conduction in Dielectric Thin Films”, *Journal of Heat Transfer*, vol. 115, pp. 7–16 (1993)

[95] D. Y. Shchegolkov, *et al*., “Perfect sub-wavelength metamaterial fishnet-like film absorbers for THz applications”, *34th International Conference on Infrared, Millimeter, and Terahertz Waves (IRMMW-THz 2009)*, ISBN: 978-1-4244-5416-7 (2009)

[96] G. J. Dolan, “Offset masks for lift-off photoprocessing”, *Applied Physics Letters*, vol. 31, pp. 337–229 (1977)

[97] Information is available at: http://anff-act.anu.edu.au/HTM/detail/flagship_services.htm (extracted on 24/11/2014)

[98] B. Kante, *et al*., “Infrared metafilms on a dielectric substrate”, *Physical Review B*, vol. 80, pp. 205120 (2009)

[99] B. Lahiri, *et al*., “Impact of titanium adhesion layers on the response of metallic split-ring resonators (SRRs)”, *Optics Express*, vol. 18, issue 11, pp. 11202–11208 (2010)

[100] Information on Sputter system is available at: http://www.ajaint.com/systems_atc.htm (extracted on 24/11/2014)

[101] F. Watt, *et al*., “Proton beam writing”, *Materials Today*, vol. 10, issue 6, pp. 20–29 (2007)

[102] J. A. van Kan, *et al*., “Three-dimensional nanolithography using proton beam writing”, *Applied Physics Letters*, vol. 83, issue 8, pp. 1629–1631 (2003)

[103] L. A. Giannuzzi, "Introduction to focused ion beams: instrumentation, theory techniques and practice", *Boston: Springer* (2004)

[104] Information on FIB system is available at: http://www.fibics.com/fib/tutorials/introduction-focused-ion-beam-systems/4/ (extracted on 24/11/2014)

[105] Information on FIB system is available at: http://www.fei.com/products/dualbeam/helios-nanolab (extracted on 24/11/2014)

[106] AutoScript xT Technical Note, *FEI Company* (2005)

[107] Auto FIB 2nd Ed., *FEI Company* (2005)

[108] C. M. Park, *et al.*, "Measurement of Ga implantation profiles in the sidewall and bottom of focused-ion-beam-etched structures", *Applied Physics Letters*, vol. 84, issue 17, pp. 3331–3333 (2004)

[109] J.C. Reiner, *et al.*, "Gallium artefacts on FIB-milled silicon samples", *Microelectronics Reliability*, vol. 44, pp. 1583–1588 (2004)

[110] R. I. Barabash, *et al.*, "Mapping strain gradients in the FIB-structured InGaN/GaN multilayered films with 3D X-Ray microbeam", *Materials Science and Engineering A*, vol. 528, pp. 52–57 (2010)

[111] E. G. Mironov, *et al.*, "Titanium nano-antenna for high-power pulsed operation", *IEEE Journal of Lightwave Technology*, vol. 31, issue 15, pp. 2459–2466 (2013)

[112] E. G. Mironov, *et al.*, "High power titanium Q-switched nano-antennas", *OSA Advanced Photonics 2013* (Rio Grande, Puerto Rico, United States), ISBN: 978-1-55752-981-7 (2013)

[113] P. Bharadwaj, *et al.*, "Optical Antennas", *Advances in Optics and Photonics*, vol. 1, pp. 438–483 (2009)

[114] N. Yu, E. Cubukcu, *et al.*, "Bowtie plasmonic quantum cascade laser antenna", *Optics Express*, vol. 15, issue 20, pp. 13272–13281 (2007)

[115] V. D. Kumar and K. Asakawa, "Investigation of a slot nanoantenna in optical frequency range", *Photonics and Nanostructures – Fundamentals and Applications*, vol. 7, pp. 161–168 (2009)

[116] T. Kosako, *et al.*, "Directional control of light by a nano-optical Yagi-Uda antenna", *Nature Photonics*, vol. 4, pp. 312–315 (2010)

[117] T. H. Taminiau, *et al.*, "Enhanced directional excitation and emission of single emitters by a nano-optical Yagi-Uda antenna", *Optics Express*, vol. 16, issue 14, pp. 10858–10866 (2008)

[118] C. Fumeaux, *et al.*, "Polarization response of asymmetric-spiral infrared antennas", *Applied Optics*, vol. 36, issue 25, pp. 6485–6490 (1997)

[119] J. Alda, *et al.*, "Optical antennas for nano-photonic applications", *Nanotechnology*, vol. 16, pp. S230–S234 (2005)

[120] F. González and G. Boreman, "Comparison of dipole, bowtie, spiral and log-period IR antennas", *Infrared Physics and Technology*, vol. 46, pp. 418–428 (2004)

[121] C. Middlebrook, *et al*., “Infrared phased-array antenna”, *Microwave and Optical Technology Letters*, vol. 50, issue 3, pp. 719–723 (2008)

[122] W. Yu-Ming, *et al*., “Geometric effects in designing bow-tie nanoantenna for optical resonance investigation”, *Asia-Pacific Symposium on Electromagnetic Compatibility (APEMC)*, pp. 1108–1111, ISBN 978-1-4244-5621-5 (2010)

[123] Z. Li, *et al*., “A plasmonic staircase nano-antenna device with strong electric field enhancement for surface enhanced Raman scattering (SERS) applications”, *Journal of Physics D: Applied Physics*, vol. 45, 305102 (2012)

[124] A. E. Krasnok, *et al*., “All-dielectric optical nanoantennas”, *Optics Express*, vol. 20, issue 18, pp. 20599–20604 (2012)

[125] G. Pellegrini, *et al*., “Light Extraction with Dielectric Nanoantenna Arrays”, *American Chemical Society Nano*, vol. 3, issue 9, pp. 2715–2721 (2009)

[126] S. Law, *et al*., “All-Semiconductor Plasmonic Nanoantennas for Infrared Sensing”, *Nano Letters*, vol. 13, issue 9, pp. 4569–4574 (2013)

[127] H. F. Hofmann, *et al*., “Design parameters for a nano-optical Yagi–Uda antenna”, *New Journal of Physics*, vol. 9, 217 (2007)

[128] I. S. Maksymov, *et al*., “Actively tunable bistable optical Yagi-Uda nanoantenna”, *Optics Express*, vol. 20, issue 8, pp. 8929–8938 (2012)

[129] H. A. Atwater and A. Polman, “Plasmonics for improved photovoltaic devices”, *Nature Materials*, vol. 9, pp. 205–213 (2010)

[130] D. K. Kotter, *et al*., “Theory and Manufacturing Processes of Solar Nanoantenna Electromagnetic Collectors”, *Journal of Solar Energy Engineering*, vol. 132, pp. 011014 (2010)

[131] E. S. Ünlü, *et al*., “Broadband plasmonic nanoantenna with an adjustable spectral response”, *Optics Express*, vol. 19, issue 2, pp. 1000–1006 (2011)

[132] N. Yu, *et al*., “Plasmonic quantum cascade laser antenna”, *Applied Physics Letters*, vol. 91, pp. 173113 (2007)

[133] N. Yu, *et al*., “Quantum cascade lasers with integrated plasmonic antenna-array collimators”, *Optics Express*, vol. 16, issue 24, pp. 19447–19461 (2008)

[134] A. Campion and P. Kambhampati, “Surface-enhanced Raman scattering”, *Chemical Society Reviews*, vol. 27, pp. 241–250 (1998)

[135] K. Kneipp, *et al*., “Surface-enhanced Raman scattering and biophysics”, *Journal of Physics: Condensed Matter*, vol. 18, pp. R597–R624 (2002)

[136] E. C. Le Ru, *et al*., “Surface Enhanced Raman Scattering Enhancement Factors: A Comprehensive Study”, *Physical Chemistry C*, vol. 111, issue 37, pp. 13794–13803 (2007)

[137] S. Aksu, *et al*., “High-throughput nanofabrication of infrared plasmonic nanoantenna arrays for vibrational nanospectroscopy”, *Nano Letters*, vol. 10, pp. 2511–2518 (2010)

[138] S. S. Chang, *et al*., "The shape transition of gold nanorods", *Langmuir*, vol. 15, pp. 701–709, (1999)

[139] S. Link, *et al*., "How long does it take to melt a gold nanorod? A femtosecond pump-probe absorption spectroscopy study", *Chemical Physics Letters*, vol. 315, pp. 12–18 (1999)

[140] M. E. Fermann, *et al*., "Ultrafast Lasers: Technology and Applications", *New York: Marcel Dekker* (2003)

[141] E. Mironov, *et al*., "Analysis of silica filled-slot waveguides based on hyperbolic metamaterials", *Journal of the Optical Society of America B*, vol. 31, issue 8, pp. 1822–1828 (2014); Erratum – vol. 31, issue 10, pp. 2285 (2014)

[142] E. Mironov, *et al*., "Sub-wavelength confinement in metamaterial filled-slot waveguide", *Conference on Lasers and Electro-Optics 2014 / CLEO 2014* (San Jose, California, USA), ISBN: 978-1-55752-999-2 (2014)

[143] D. Liu and C. Svensson, "Power consumption estimation in CMOS VLSI circuit", *IEEE Journal of Solid-State Circuits*, vol. 29, issue 6, pp. 663–670 (1994)

[144] S. Fan, *et al*., "Channel drop filters in photonic crystals", *Optics Express*, vol. 3, issue 1, pp. 4–11 (1998)

[145] T. Asano, *et al*., "A channel drop filter using a single-defect in a 2-D photonic crystal slab: defect engineering with respect to polarization mode and ratio of emissions from upper to lower sides", *IEEE Journal of Lightwave Technology*, vol. 21, issue 5, pp. 1370–1376 (2003)

[146] H. Nguyen, *et al*., "Sub-100 μm photonic crystal Si optical modulators: spectral, athermal, and high speed performance", *IEEE Journal on Selected Topics in Quantum Electronics*, vol. 19, issue 6 3400811 (2013)

[147] H. T. Hattori, *et al*., "Cantor set fiber Bragg grating", *Journal of the Optical Society of America A*, vol. 17, issue 9, pp. 1583–1589 (2000)

[148] T. F. Krauss, *et al*., "Two-dimensional photonic bandgap structures at near infrared wavelength", *Nature*, vol. 383, pp. 699–702 (1996)

[149] H. T. Hattori, *et al*., "In-plane coupling of light from InP-based photonic crystal band-edge lasers into single-mode waveguides", *IEEE Journal of Quantum Electronics*, vol. 43, issue 4, pp. 279–286 (2007)

[150] M. Fujita, *et al*., "Ultra-small and ultra-low threshold microdisk injection laser-design, fabrication, lasing characteristics and spontaneous emission factor", *IEEE Journal on Selected Topics in Quantum Electronics*, vol. 5, issue 3, pp. 673–681 (1999)

[151] S. V. Boriskina, *et al*., "Directional emission, increased free spectral range, and mode Q-factors in 2-D wavelength-scale optical microcavity structures", *IEEE Journal on Selected Topics in Quantum Electronics*, vol.12, issue 6, pp. 1175–1182 (2006)

[152] H. T. Hattori, "Analysis of optically pumped equilateral triangular microlasers with three mode-selective trenches", *Applied Optics*, vol. 47, issue 12, pp. 2178–2185 (2008)

[153] H. T. Hattori, *et al*., "Large square resonator laser with quasi single-mode operation", *IEEE Photonics Technology Letters*, vol. 21, issue 6, pp. 359–361 (2009)

[154] S. E. Kocabas, *et al*., "Modal analysis and coupling in metal-insulator-metal waveguides", *Physical Review B*, 79, pp. 035120 (2009)

[155] H. J. Lezec, *et al*., "Beaming light from a subwavelength aperture", *Science*, vol. 297, pp. 820–822 (2002)

[156] D. Dai and S. He, "A silicon-based hybrid plasmonic waveguide with a metal cap for a nano-scale light confinement", *Optics Express*, vol. 17, issue 19, pp. 16646–16653 (2009)

[157] J. Lin, *et al*., "Polarization-controlled tunable directional coupling of surface plasmon polaritons", *Science*, vol. 340, pp. 331–334 (2013)

[158] M. T. Hill, *et al*., "Lasing in metal-insulator-metal sub-wavelength plasmonic waveguides", *Optics Express*, vol. 17, issue 13, pp. 11107–11112 (2009)

[159] E. Cubukcu, *et al*., "Plasmonic laser antennas and related devices", *IEEE Journal on Selected Topics in Quantum Electronics*, vol. 14, issue 6, pp. 1448–1461 (2008)

[160] H. J. Y. Allen, *et al*., "Optical manipulation of nanoparticles and biomolecules in sub-wavelength slot waveguides", *Nature*, vol. 457, pp. 71–75 (2009)

[161] A. N. Grigorenko, *et al*., "Nanometric optical tweezers based on nanostructured substrates", *Nature Photonics*, vol. 2, pp. 365–370 (2008)

[162] J. Van Campehout, *et al*., "Low-footprint optical interconnect on an SOI chip through heterogeneous integration of InP-Based microdisk lasers and microdetectors", *IEEE Photonics Technology Letters*, vol. 21, issue 8, pp. 522–524 (2009)

[163] L. O'Faolain, *et al*., "Low-loss propagation in photonic crystal waveguides", *Electronics Letters*, vol. 42, issue 25, pp. 1454–1455 (2006)

[164] M. Gnan, *et al*., 'Fabrication of low-loss photonic wires in silicon-on-insulator using hydrogen silsesquioxane electron-beam resist", *Electronics Letters*, vol. 44, issue 2, pp. 115–116 (2008)

[165] G. Roelkens, *et al*., "High efficiency grating coupler between silicon-on-insulator waveguides and perfectly vertical optical fibers", *Optics Letters*, vol. 32, issue 11, pp. 1495–1497 (2007)

[166] Y. He, *et al*., "Nanoscale metamaterial optical waveguides with ultrahigh refractive indices", *Journal of the Optical Society of America B*, vol. 29, issue 9, pp. 2559–2566 (2012)

[167] L. Chen, *et al*., "Subwavelength confinement in an integrated metal slot waveguide on silicon", *Optics Letters*, vol. 31, issue 14, pp. 2133–2135 (2006)

[168] G. Veronis and S. Fan, "Modes of Subwavelength Plasmonic Slot Waveguides", *IEEE Journal of Lightwave Technology*, vol. 25, issue 9, pp. 2511–2521 (2007)

[169] J. A. Dionne, *et al*., "Highly Confined Photon Transport in Subwavelength Metallic Slot Waveguides", *Nano Letters*, vol. 6, issue 9, pp. 1928–1932 (2006)

[170] V. R. Almeida, *et al*., “Guiding and confining light in void nanostructure”, *Optics Letters*, vol. 29, issue 11, pp. 1209–1211 (2004)

[171] P. A. Anderson, *et al*., “High confinement in silicon slot waveguides with sharp bends”, *Optics Express*, vol. 14, issue 20, pp. 9197–9202 (2006)

[172] J. J. Burke, *et al*., “Surface-polariton-like waves guided by thin, lossy metal films”, *Physical Review B*, vol. 33, pp. 5186–5201 (1986)

[173] P. Berini, “Plasmon-polariton waves guided by thin lossy metal films of finite width: Bound modes of symmetric structures”, *Physical Review B*, vol. 61, issue 15, pp. 10484–10503 (2000)

[174] C. A. Foss, *et al*., “Template-Synthesized Nanoscopic Gold Particles: Optical Spectra and the Effects of Particle Size and Shape”, *Journal of Physical Chemistry*, vol. 98, issue 11, pp. 2963–2971 (1994)

[175] A. Sihvola, “Electromagnetic Mixing Formulas and Applications”, *London: Institution of Electrical Engineering* (1999)

[176] P. U. Jepsen, et al., “Metal-insulator phase transition in a VO_2 thin film observed with terahertz spectroscopy”, *Physical Review B*, vol. 74, pp. 205103 (2006)

[177] Y. He, *et al*., “Giant transverse optical forces in nanoscale slot waveguides of hyperbolic metamaterials”, *Optics Express*, vol. 20, issue 20, pp. 22372–22382 (2012)

[178] N. Feng, *et al*., “Lossless strip-to-slot waveguide transformer”, *Optics Letters*, vol. 32, issue 10, pp. 1250–1252 (2007)

[179] Q. Xu, *et al*., “Experimental demonstration of guiding and confining light in nanometer-size low-refractive-index material”, *Optics Letters*, vol. 29, issue 14, pp. 1626–1628 (2004).

[180] Z. Wang, *et al*., “Ultracompact low-loss coupler between strip and slot waveguides”, *Optics Letters*, vol. 34, issue 10, pp. 1498–1500 (2009)

[181] P. Horowitz and W. Hill, “The art of electronics”, *Cambridge: Cambridge university press* (1989)

[182] Y Avitzour, *et al*., “Wide-angle infrared absorber based on a negative-index plasmonic metamaterial”, *Physical Review B*, vol. 79, pp. 045131 (2009)

[183] E. G. Mironov, *et al*., “Fishnet metamaterials with incorporated titanium absorption layer”, *Journal of Physics D: Applied Physics*, vol. 46, no. 49, 495107 (2013)

[184] E. G. Mironov, *et al*., “Titanium absorption layer in fishnet metamaterials”, *Australian and New Zealand Conference on Optics and Photonics 2013 / ANZCOP 2013* (Perth, Western Australia, Australia) (2013)

[185] L. Liu, *et al*, “Temperature control of terahertz metamaterials with liquid crystals”, *IEEE Transactions on Terahertz Science and Technology*, vol. 3, no. 6, pp. 827–831 (2013)

[186] T. Driscoll, *et al*., “Dynamic tuning of an infrared hybrid-metamaterial resonance using vanadium dioxide”, *Applied Physics Letters*, vol. 93, pp. 024101 (2008)

[187] D. A. Powell, *et al*., “Metamaterial tuning by manipulation of near-field interaction”, *Physical Review B*, vol. 82, pp. 155128 (2010)

[188] N. R. Han, *et al*., “Broadband multi-layer terahertz metamaterials fabrication and characterization on flexible substrates”, *Optics Express*, vol. 19, issue 8, pp. 6990–6998 (2011)

[189] D. R. Chowdhury, *et al*., “A broadband planar terahertz metamaterial with nested structure”, *Optics Express*, vol. 19, issue 17, pp. 15817–15823 (2011)

[190] G. I. Eleftheriades and K. G. Balmain, “Negative refraction metamaterials: Fundamental Principles and Applications”, *Hoboken: John Wiley & Sons, Inc.* (2005)

[191] C. Enkrich, *et al*., “Focused-ion-beam nanofabrication of near-infrared magnetic metamaterials”, *Advanced Materials*, vol. 17, pp. 2547–2549 (2005)

[192] Y. A. Urzhumov and G. Shvets “Optical magnetism and negative refraction in plasmonic metamaterials”, *Solid State Communications*, vol. 146, pp. 208–220 (2008)

[193] D. Schurig, *et al*., “Metamaterial electromagnetic cloak at microwave frequencies”, *Science*, vol. 314, pp. 977–980 (2006)

[194] C. M. Bingham, *et al*., “Planar wallpaper group metamaterials for novel terahertz applications”, *Optics Express*, vol. 16, issue 23, pp. 18565–18575 (2008)

[195] G. Dolling, *et al*., “Cut-wire pairs and plate pairs as magnetic atoms for optical metamaterials”, *Optics Letters*, vol. 30, issue 23, pp. 3198–3200 (2005)

[196] V. Shalaev, “Optical negative-index metamaterials”, *Nature Photonics*, vol. 1, pp. 41–48 (2007)

[197] S. Zhang, *et al*., “Negative Refractive Index in Chiral Metamaterials”, *Physical Review Letters*, vol. 102, pp. 023901 (2009)

[198] Y. Ye and S. He, “90° polarization rotator using a bilayered chiral metamaterial with giant optical activity”, *Applied Physics Letters*, vol. 96, pp. 203501 (2010)

[199] H. T. Chen, *et al*., “Complementary planar terahertz metamaterials”, *Optics Express*, vol. 15, issue 3, pp. 1084–1095 (2007)

[200] L. Zhang, *et al*., “Creating double negative index materials using the Babinet principle with one metasurface”, *Physical Review B*, vol. 87, pp. 045101 (2013)

[201] I. V. Shadrivov, *et al*., “Second-harmonic generation in nonlinear lefthanded metamaterials”, *Journal of the Optical Society of America B*, vol. 23, issue 3, pp. 529–534 (2006)

[202] A. K. Popov, *et al*., “Four-wave mixing, quantum control, and compensating losses in doped negative-index photonic metamaterials”, *Optics Letters*, vol. 32, issue 20, pp. 3044–3046 (2007)

[203] A. K. Popov and V. M. Shalaev, “Compensating losses in negative-index metamaterials by optical parametric amplification”, *Optics Letters*, vol. 31, issue 14, pp. 2169–2171 (2006)

[204] J. B. Pendry, “Negative Refraction Makes a Perfect Lens”, *Physical Review Letters*, vol. 85, issue 18, pp. 3966–3969 (2000)

[205] T. Ergin, *et al.*, "Three-Dimensional Invisibility Cloak at Optical Wavelengths", *Science*, vol. 328, pp. 337–339 (2010)

[206] W. Cai, *et al.*, "Optical cloaking with metamaterials", *Nature Photonics*, vol.1, pp. 224–227 (2007)

[207] N. I. Zheludev and Y. S. Kivshar, "From metamaterials to metadevices", *Nature Materials*, vol. 11, pp. 917–924 (2012)

[208] Y. P. Meshcheryakov and N. M. Bulgakova "Thermoelastic modeling of microbump and nanojet formation on nanosize gold films under femtosecond laser irradiation", *Applied Physics A*, vol. 82, pp. 363–368 (2006)

[209] Information on CST Microwave Studio is available at: https://www.cst.com/Products/CSTMWS (extracted on 24/11/2014)

[210] D. M. Pozar, "Microwave Engineering" (3rd Ed.), *New York: John Wiley & Sons, Inc.* (2005)

[211] D. R. Smith and S. Schultz, "Determination of effective permittivity and permeability of metamaterials from reflection and transmission coefficients", *Physical Review B*, vol. 65, pp. 195104 (2002)

[212] C. Menzel, *et al.*, "Retrieving effective parameters for metamaterials at oblique incidence", *Physical Review B*, vol. 77, pp. 195328 (2008)

[213] M. I. Kaganov, *et al.*, "Relaxation between electrons and crystalline lattices", *Soviet Physics JETP*, vol. 4, pp. 173 (1957)

[214] S. I. Anisimov, *et al.*, "Electron emission from metal surfaces exposed to ultrashort laser pulses", *Soviet Physics JETP*, vol. 39, pp. 375 (1974)

[215] S. S. Wellershoff, *et al.*, "The role of electron–phonon coupling in femtosecond laser damage of metals", *Applied Physics A*, vol. 69, pp. S99–S107 (1999)

[216] S. P. Timoshenko, "Course of Theory of Elasticity" (in Russian), Kiev: Naukova Dumka (1972)

[217] M. L. Wilkins, "Calculation of Elastic-plastic Flow In: Methods in Computational Physics", *Academic, New York: Fundamental Methods in Hydrodynamics* (1964)

[218] F. Korte, *et al.*, "Formation of microbumps and nanojets on gold targets by femtosecond laser pulses", *Applied Physics A*, vol. 79, pp. 879–881 (2004)

[219] A. V. Bobylev, "Mechanical and Technological Properties of Metals" (in Russian), *Moscow: Metallurgia* (1987)

[220] J. Koch, *et al.*, "Nanotexturing of gold films by femtosecond laser-induced melt dynamics", *Applied Physics A*, vol. 81, pp. 325–328 (2005)

[221] Information on Windows Notepad is available at: http://windows.microsoft.com/en-au/windows/notepad-faq#1TC=windows-7 (extracted on 24/11/2014)

[222] Information on Royal Australian Air Force is available at: http://www.airforce.gov.au/ (extracted on 24/11/2014)

[223] T. M. Lillesand, *et al*., “Remote sensing and image interpretation”, *Chichester: John Wiley & Sons Ltd*. (2004)

[224] Information on the International Women’s Day is available at: http://www.un.org/womenwatch/feature/iwd/history.html (extracted on 24/11/2014)

[225] Information on the ANZAC Day is available at: http://www.awm.gov.au/commemoration/anzac-day/ (extracted on 24/11/2014)

Appendix A – Simple FIB scripting

This appendix explains the AutoScript patterning code **[106]** by providing an example of a simple rectangular geometry. As a general overview of the patterning process can be found in Chapter 4 (Section 4.3.2), it is not described here.

AutoScript is a scripting language used by FEI research equipment to automate the patterning process in a FIB **[105]**. The code is written as a plain text file with an extension, *.psc,* which can be created through Windows Notepad **[221]** or similar software and is executed by AutoFiB **[107]**. AutoScript explicitly defines a pattern's geometry as well as its fabrication conditions and imaging settings. Its main commands can be grouped in the following categories:

1) Patterning and milling (designing shape, adjusting milling depth);
2) Imaging the sample surface (grabbing frames and saving them);
3) Exercising beam control of the electron and ion columns (focusing, stigmation, aperture);
4) Determining detector settings (brightness and contrast);
5) Defining logical operators (condition statements, loops, timer);
6) Conducting miscellaneous activities (stage positioning, pressure control, dialog commands, etc.).

The analysis of an AutoScript code for milling a simple rectangular hole centered in the coordinate origin with dimensions of 2×2×0.2 μm is presented in Fig. 9.1. The left column represents the code itself and the right comments on the corresponding portions of the script (the variables are given in italics). In fact, the presented code is routinely used as a template for all fabrications conducted during this candidature with the only difference being the pattern details (i.e., milling depth and *x*-, *y*-coordinates).

clear	
setctrlbeam 0	Selects ion column
setbeamshift 0, 0	Sets beam shift to zero in both *x*- and *y*-axis
dialog 3, "Str file", "Box tool", "Cancel", "Milling", "Choose milling method"	Creates a dialog window titled "Milling" with description "Choose milling method" and 3 available options: Str file, Box tool and Cancel
if (dresult = 1) goto strfile	
if (dresult = 2) goto millboxes	
if (dresult = 3) goto end	
strfile:	
dialog 1, "OK", "Stream file", "Load str file"	Creates a dialog window titled "Steam file" with description "Load str file" and single available option: Ok
goto millboxes	
millboxes:	
#all values are given in µm	
depth = 0.2	
setpatinfo depth, Si	Sets the milling conditions to *depth* and application to *Si*
#-----------------pattern------------------	
x_1=-1	
y_1=-1	
x_2=1	Creates a rectangular pattern with coordinates x_1, y_1, x_2, y_2
y_2=1	
box x_1,y_1,x_2,y_2	
#---	
mill	Mills the defined pattern (in this case, rectangular)
waitformill	Pauses the script
sleep 100	Pauses the script on 100 milliseconds
clear	
dialog 1, "OK", "Success", "Pattern complete"	Creates a dialog window titled "Success" with description "Pattern complete" and single available option: Ok
goto end	
end:	
dialog 1, "OK", "End", "Finished"	Creates a dialog window titled "End" with description "Finished" and single available option: Ok

Fig. 9.1 – Analysis of AutoScript code

Appendix B – Advanced FIB scripting

While Appendix A discusses a very simple geometry, this one focuses on advanced designs to demonstrate the FIB's patterning capabilities. Therefore, the structures are deliberately chosen to have non-periodic complex shapes with multiple vertices (note that the patterns described further are *not* related in any way to high-power plasmonic devices other than being fabricated using the same equipment).

A perfect example of such a complex design is the symbol of the Royal Australian Air Force (RAAF), which is drawn as a red kangaroo hopping inside a blue ring (Fig. 9.2) **[222]**. This logo consists of three primary elements: a kangaroo; text; and ring. While the third element is easy to mill since AutoScript has an inbuilt command for creating rings, the first two require determinations of their spatial coordinates before inserting these data into the AutoScript template.

Fig. 9.2 – Royal Australian Air Force logo

The patterning process can be performed in the following steps:

1) Finding the figure's edges via image processing (Sobel operator **[223]**) and vectorization of a bitmap figure (alternatively, the figure's vertices can be found manually by estimating their positions);
2) Generating a MATLAB shape by breaking the image into several segments (Fig. 9.3a and Fig. 9.4a);
3) Extracting the spline coordinates;
4) Modifying the AutoScript file;
5) Patterning a kangaroo (Fig. 9.3b);
6) Patterning a ring (simple shape);
7) Patterning "RAAF" (Fig. 9.4b).

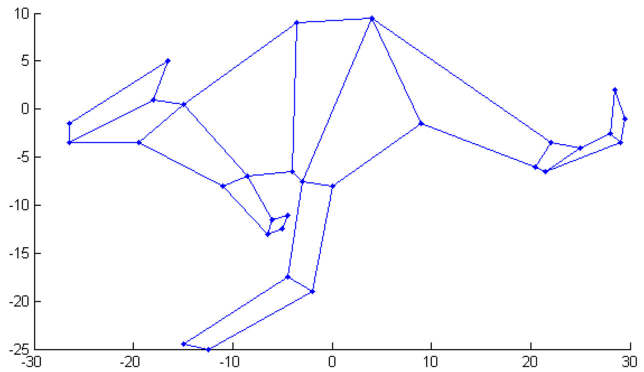

Fig. 9.3a – Vectorized kangaroo

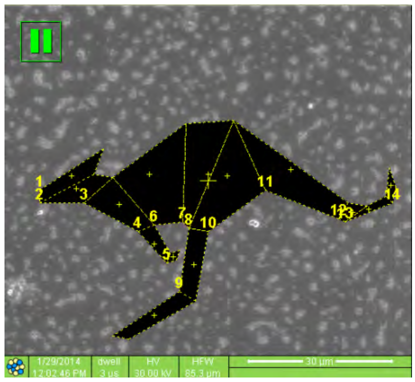
Fig. 9.3b – Patterned kangaroo

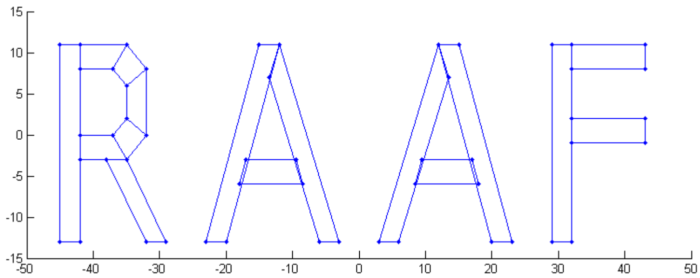

Fig. 9.4a – Vectorized RAAF

Fig. 9.4b – Patterned RAAF

The vectorized profile of the RAAF figure allows it to be easily scaled, as shown in Figs. 9.5a-9.6c. Here the scaling factor is chosen to be ×12.5, which results in a large kangaroo being visible even through a simple optical microscope.

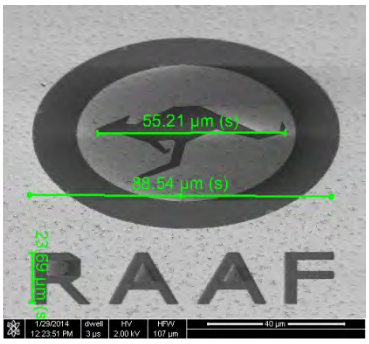

Fig. 9.5a – Large RAAF logo (with scale bar)

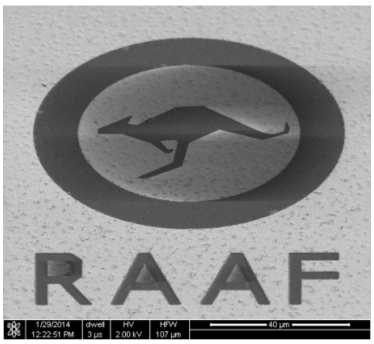

Fig. 9.5b – Large RAAF logo

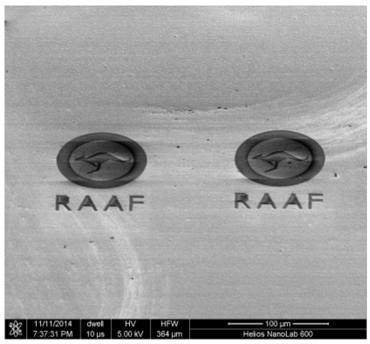

Fig. 9.5c – Two large RAAF logos

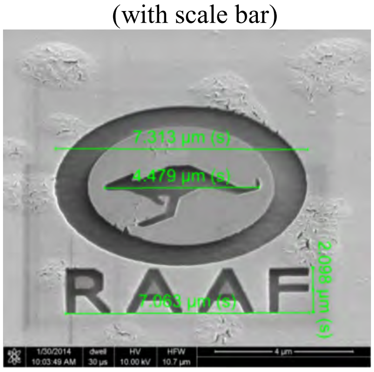

Fig. 9.6a – Small RAAF logo (with scale bar)

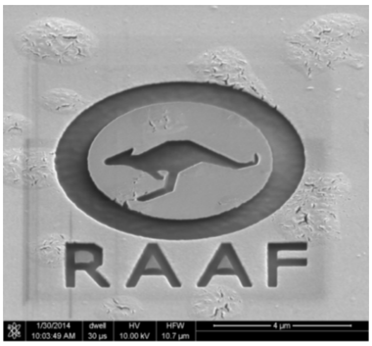

Fig. 9.6b – Small RAAF logo

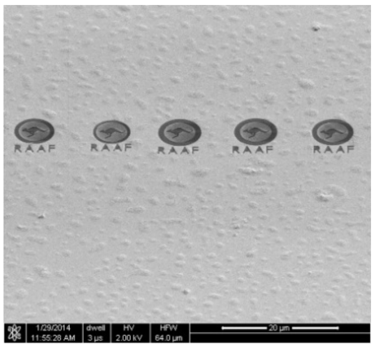
Fig. 9.6c – Five small RAAF logos

Other examples of advanced nano-patterns are presented in Fig. 9.7 and Fig. 9.8. Both are fabricated in a gold film deposited on a quartz substrate, with their large features milled at 9.7 nA and small ones at 28 pA. The typical milling time varies between 15 minutes and half an hour and the structures have an average depth of 200 nm. Fig. 9.7 represents a rosebud fabricated for the celebration of International Women's Day **[224]** (8^{th} March). Note that the charging of the isolated metallic regions in the rosebud and letters *P*, *R*, *O* and *D* results in a visual effect of glowing, because electrons become scattered more intensively from the sample's surface. The image in Fig. 9.8, which is devoted to ANZAC Day **[225]** (25^{th} April), consists of about 300 individual milled segments. Since this pattern is considerably larger than the rosebud (~4 times), the charging effects are not so clearly observed. The letters in both figures are generated by a separate script, which converts symbols into polygonal patterns and effectively allows the milling of any arbitrary text.

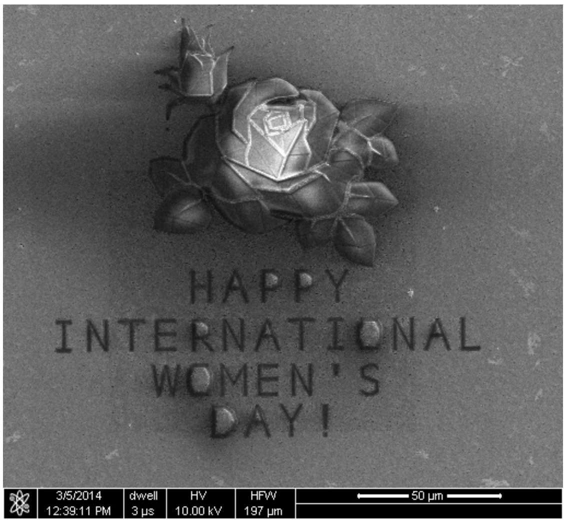

Fig. 9.7 – International Women's Day pattern

Fig. 9.8 – ANZAC Day pattern